Aus dem Walther-Straub-Institut für Pharmakologie und Toxikologie
Institut der Ludwig-Maximilians-Universität München
Vorstand: Prof. Dr. med. Thomas Gudermann

Identification of TRPM7-dependent pathways

Dissertation
zum Erwerb des Doktorgrades der Naturwissenschaften
an der Medizinischen Fakultät der
Ludwig-Maximilians-Universität München

vorgelegt von

Miyuki Egawa

aus

München, Deutschland

2025

Mit Genehmigung der Medizinischen Fakultät
der Ludwing-Maximilians-Universität München

Erstgutachter:	Prof. Dr. Dr. Christian Grimm
Zweitgutachter:	Prof. Dr. Alexander Faußner
Dekan:	Prof. Dr. med. Thomas Gudermann

Tag der mündlichen Prüfung: 12. Februar 2026

Affidavit

LMU LUDWIG-MAXIMILIANS-UNIVERSITÄT MÜNCHEN | Promotionsbüro Medizinische Fakultät | MMRS

Eidesstattliche Versicherung

Egawa, Miyuki
Name, Vorname

Ich erkläre hiermit an Eides statt, dass ich die vorliegende Dissertation mit dem Titel:

Identification of TRPM7-dependent pathways

selbständig verfasst, mich außer der angegebenen keiner weiteren Hilfsmittel bedient und alle Erkenntnisse, die aus dem Schrifttum ganz oder annähernd übernommen sind, als solche kenntlich gemacht und nach ihrer Herkunft unter Bezeichnung der Fundstelle einzeln nachgewiesen habe.

Ich erkläre des Weiteren, dass die hier vorgelegte Dissertation nicht in gleicher oder in ähnlicher Form bei einer anderen Stelle zur Erlangung eines akademischen Grades eingereicht wurde.

München, 16.02.2026
Ort, Datum

Miyuki Egawa
Unterschrift Doktorandin

Table of Contents

Abbreviations

ATP	Adenosine triphosphate
cDNA	Complementary deoxyribonucleic acid
DT40 cells	Avian leukosis virus (ALV)-induced lymphoma chicken cells
eEF2K	Elongation factor-2 kinase
GTP	Guanosine triphosphate
HAP1 cells	Human haploid leukemia cells
HEK293T cells	Human embryonic kidney 293 T cells
HeLa cells	Henrietta Lacks cervical cancer cells
HER2 /ERBB2	Human epidermal growth factor receptor 2
KO	Knockout
MDA-MB-231 cells	M.D. Anderson metastasis breast cancer cells
PIP_2	Phosphatidylinositol 4,5-bisphosphate
PLCγ2	Phospholipase C gamma 2
RhoA	Ras homolog family member A
SKBR3 cells	Sloan-Kettering breast cancer cells line 3
SMAD2/3	Mothers against decapentaplegic homolog 2/3
SOCE	Store-operated Ca^{2+} entry
STIM2	Stromal interaction molecule 2
TRP channels	Transient receptor potential channels
TRPM6	Transient receptor potential cation channel, subfamily M, member 6
TRPM7	Transient receptor potential cation channel, subfamily M, member 7
TS cells	Trophoblast stem cells
WT	Wild type

List of publications

1. **Egawa M.**, Schmücker E., Grimm C., Gudermann T., Chubanov V. Expression Profiling Identified TRPM7 and HER2 as Potential Targets for the Combined Treatment of Cancer Cells. *Cells*. 2024; 13(21):1801. https://doi.org/10.3390/cells13211801

2. Schmidt E., Narangoda C., Nörenberg W., **Egawa M**., et al. Structural mechanism of TRPM7 channel regulation by intracellular magnesium. Cellular and Molecular Life Sciences. 2022; https://doi.org/10.1007/s00018-022-04192-7

1. Contribution to publications

1.1 Contribution to Publication I [1]

In my first publication [1], I explored whether the TRPM7-mediated uptake of Zn^{2+} promotes tumour survival and assessed the potential for combining TRPM7 inhibitors with standard cancer treatments to achieve a synergistic therapeutic effect. Using genome-wide transcriptome profiling of haploid human leukemia (HAP1) cells, I investigated pathways commonly affected by knockout of *TRPM7* using the CRISPR/Cas9 approach as well as by pharmacological agent NS8593, a potent blocker of the TRPM7 channel. These experiments showed that TRPM7 regulates the expression levels of multiple transcripts, including the human epidermal growth factor receptor 2 HER2 (ERBB2). Also, I studied different non-hematopoietic cells, including trophoblast stem (TS) cells, HEK293 cells, HeLa cells and found that the deletion of *TRPM7* impacts HER2 expression in a Zn^{2+}-dependent manner. Additionally, I discovered that co-administering pharmacologic antagonists of HER2 and TRPM7 exerted a synergistic antiproliferative effect in HER2-positive SKBR3 breast cancer cells. However, this synergistic effect was not observed in HER2-deficient MDA-MB-231 cells. Collectively, the study concludes that the TRPM7 channel is critically implicated in Zn^{2+}-dependent regulation of HER2 expression. These findings suggest a new strategy for treating HER2-positive breast cancer cells.

In this study, I conducted the experiments illustrated in Figure 1 A, C, D, E, Figure 2, Figure 3 A, B, C, D, Figure 4, Figure 5 A, B, C, D, Figure 6, Suppl. Figure S1, Suppl. Figure S2, Suppl. Figure S4, Suppl. Table S1, Suppl. Table S2, and Suppl. Table S3

Figure 1: Functional examination of *TRPM7* KO HAP1 cells.

Given that clonal selection procedures often contribute to a considerable diversity of cell phenotypes, I investigated two clones of HAP1 cell lines with independent frameshift mutations in *TRPM7*. To functionally characterize these clones of HAP1 cells, I used the patch-clamp technique, which confirmed the absence of detectable TRPM7 currents in both HAP1 *TRPM7* knockout (KO) cell lines. I then compared the proliferation rates of wild type (WT) and *TRPM7* KO cells and found that *TRPM7* KO cells grew significantly slower than WT cells.

Figure 2: Transcriptome profiling of HAP1 cells.

To examine cellular pathways regulated by TRPM7, I conducted genome-wide transcriptome profiling of HAP1 cells using a microarray approach. This led to the identification of several commonly up- and down-regulated transcripts in WT HAP1 cells treated with NS8593 and two *TRPM7* KO cell lines. I verified the results obtained using the qPCR technique. Among other changes, I observed that *HER2* expression was 30-fold upregulated in two *TRPM7* KO HAP1 cell lines.

Figure 3: TRPM7 regulates the HER2 expression in HAP1 cells.

To assess whether TRPM7 could also influence HER2 expression on the protein level, I utilized the western blot approach with a HER2-specific antibody. I found that two HAP1 *TRPM7* KO cell lines exhibited significantly higher HER2 expression compared to the wild type. Since TRPM7 is a Zn^{2+} permeable channel, I further investigated if the effect of *TRPM7* KO on HER2 expression is Zn^{2+} dependent. I supplemented the HAP1 cells with a medium containing additional Zn^{2+} or zinc pyrithione (a small organic

molecule acting as a Zn^{2+} ionophore). Treatment of the HAP1 *TRPM7* KO cells with Zn^{2+} or zinc pyrithione significantly reduced HER2 levels, bringing them closer to the levels observed in WT cells**.**

Figure 4: The effect of *TRPM7* KO on HER2 expression in trophoblast stem (TS) cells and HEK293 cells

To determine if HER2 represents a regulatory target of TRPM7 in non-hematopoietic cells, I compared the expression levels of HER2 in mouse WT and *Trpm7* KO trophoblast stem (TS) cells, WT and *TRPM7* KO HEK293 cells, and WT HEK293 cells treated with *TRPM7* siRNA. In all *TRPM7* deficient cells, the HER2 expression was significantly downregulated, and this effect could be reversed by supplementation of cells with Zn^{2+} or zinc pyrithione. These results indicate that TRPM7 modulates the expression of HER2 in a Zn^{2+}-dependent manner.

Figure 5: Targeting of TRPM7 in breast cancer cells.

Given HER2's critical role in breast cancer progression, I investigated whether TRPM7 inhibition impacts HER2 expression and the proliferation of breast cancer cells. The human breast cancer cell lines SKBR3, MCF-7 and MDA-MB-231 cells each exhibit varying levels of HER2 overexpression and are widely used to test new therapeutic strategies. We utilized western blotting to confirm that SKBR3 cells express significantly higher levels of HER2 compared to MCF-7 and MDA-MB-231 cells. Following, I examined whether HER2 is a regulatory target of TRPM7 in SKBR3 cells, and I found that two different anti-*TRPM7* siRNAs significantly downregulated HER2 levels in SKBR3 cells. Additionally, I investigated the impact of NS8593 on breast cancer cell proliferation and discovered that NS8593 dose-dependently inhibited the

proliferation of SKBR3 and MDA-MB-231 cells. These findings suggest that inhibition of TRPM7 in breast cancer cells reduces HER2 levels and elicits an antiproliferative effect.

Figure 6: Combinatory pharmacological treatment of SKBR3 cells.

To determine if combined pharmacologic inhibition of TRPM7 and HER2 can be used to improve the targeted therapy of HER2-positive cancer cells, I examined the viability of HER2-positive SKBR3 cells treated with different concentrations of CP724714, a HER2-specific inhibitor, in combination with distinct concentrations of NS8593, the TRPM7 inhibitor. The results showed a significantly synergistic antiproliferative effect of CP724714 and NS8593 in SKBR3 cells.

Supplementary Figure S1: Verification of *TRPM7* KO mutation in HAP1 cells.

To examine the newly generated *TRPM7* KO-01 HAP1 cell line, I analyzed the presence of aberrant TRPM7 transcripts using RT-PCR and sequencing. The analysis revealed that the PCR product from *TRPM7* KO-01 cells had an incorrect linkage of exon 3 to an intronic sequence leading to a frameshift mutation in *TRPM7* mRNA.

Supplementary Figure S2: Examination of human HeLa cells with *TRPM7* KO mutation.

I conducted patch clamp and western blot experiments to confirm that the new *TRPM7* KO HeLa cells lack TRPM7 activity. Consistent with the findings in the experiments with TS and HEK293 cells (Figure 4), *TRPM7* KO HeLa cells also showed downregulation of HER2 expression.

Supplementary Figure S4: The treatment of MDA-MB-231 cells with CP724714 and NS8593.

Since MDA-MB-231 cells display very low HER2 expression levels, I performed experiments similar to those shown in Figure 6. MDA-MB-231 cells showed no response to treatment with CP724714, and CP724714 failed to increase NS8593's antiproliferative effect in these cells. These findings further strengthen the hypothesis that the effect of NS8593 and CP724714 on SKBR3 cells is synergistic due to the high expression of HER2.

Suppl. Table S1: Affymetrix microarray analysis of transcriptome in HAP1 cells. The data from this table was used for Figure 2.

Suppl. Table S2: Up- and down-regulated transcripts in HAP1 cells subjected to genetic and pharmacological ablation of TRPM7. Inactivation of TRPM7 in HAP1 cells resulted in up-and down-regulation of several genes, as outlined in Figure 2.

Suppl. Table S3: Sequence of primers used for qRT-PCR procedures in the present study.

1.2 Contribution to Publication II [2]

The channel-kinase TRPM7 controls the membrane transport of divalent cations [1, 3-7]. It is well established that cytosolic Mg^{2+} levels regulate the TRPM7 channel [8-10], but the molecular mechanisms of this process remain enigmatic. In the present study, we used electrophysiological techniques and molecular dynamics (MD) to obtain evidence that intracellular Mg^{2+} interacts directly with TRPM7, leading to inhibition of channel activity. Specifically, we proposed that four N1097 residues located in the channel gate of TRPM7 form a regulatory Mg^{2+}-binding site. We found that the N1097Q mutation reduced the potency of Mg^{2+} but did not affect the action of other TRPM7 ligands. We also showed that mutagenesis of the closely located N1098 (N1098Q) results in a gain-of-function variant of the TRPM7 channel, offsetting the effects of all examined TRPM7 ligands, including Mg^{2+}, Mg·ATP, PIP_2 and pharmacological compounds NS8593 and naltriben, reinforcing the idea that the lower channel gate of TRPM7 has a critical functional role.

In the present study, I conducted the experiments presented in Supplementary Figures 2 and 4.

Supplementary Figure 2: I investigated the subcellular localization of the wild-type (WT) TRPM7 and two TRPM7 variants with N1097Q and N1098Q mutations. After transiently expressing the WT and mutant TRPM7 cDNA variants in HEK293T cells, I stained the fixed cells with mouse monoclonal anti-TRPM7 antibody and goat anti-mouse IgG conjugated to Alexa Fluor 488. Confocal microscopy using an LSM 880 AxioObserver with Airyscan showed no noticeable differences in the subcellular localization or distribution of TRPM7 variants in HEK293T cells. This suggests that the

N1097Q and N1098Q mutations alter TRPM7 function but do not affect its stability or cellular trafficking.

Supplementary Figure 4: I examined whether the reduced Mg·ATP sensitivity observed in the N1097Q and N1098Q mutations of TRPM7 also holds true for other magnesium nucleotides, such as Mg·GTP [11, 12]. Towards this purpose, I measured TRPM7 currents in HEK293T cells expressing WT, N1097Q and N1098Q TRPM7 variants in the presence of 6 mM Mg·GTP and 250 μM free Mg^{2+}. While this coadministration inhibited the WT TRPM7 channel, the currents in N1097Q and N1098Q TRPM7 remained unchanged after the exposure to Mg·GTP, analogously to our experiments with Mg·ATP. Based on these experimental data, I concluded that the N1097Q and N1098Q mutations did not affect the channel's response to Mg·ATP and Mg·GTP.

2. Introduction

The transient receptor potential cation channel, subfamily M, member 7 (TRPM7), is a plasma membrane protein that contains a channel segment fused to a serine/threonine protein kinase domain (Figure 1). The channel segment of TRPM7 shares sequence homology with a large group of tetrameric ion channels referred to as transient receptor potential (TRP) channels [13].

In mammals, the TRP gene superfamily consists of 28 members forming six distinct groups (subfamilies): TRPA channels (ankyrin repeats containing TRPs), TRPC channels (canonical TRPs), TRPM channels (melastatin-related TRPs), TRPML channels (mucolipin TRPs), TRPV channels (vanilloid receptor-related TRPs) and TRPP proteins (polycystin TRPs) [14]. Among the eight channels of the TRPM subfamily, only TRPM7 and its nearest homolog, TRPM6, contain the C-terminal protein kinase.

The kinase domain of TRPM7 resembles other protein kinases referred to as α-kinases, which can phosphorylate serines and threonines located in α-helixes of substrate proteins [15]. In addition to TRPM6 and TRPM7, there are four other mammalian α-kinases, including eukaryotic elongation factor-2 kinase and α-kinases 1-3 [15].

TRPM7 and TRPM6 function as plasma membrane cation channels highly permeable to divalent cations [6, 12, 16]. While TRPM6 is primarily expressed in the kidney, intestine and placenta [7, 17, 18], TRPM7 is ubiquitously expressed throughout various tissues [12, 16, 19, 20]. TRPM7 plays a critical role in regulating of Zn^{2+} and Mg^{2+} homeostasis, Ca^{2+}-dependent signaling, and cellular functions such as proliferation, motility, and exocytosis [7, 12, 21-25].

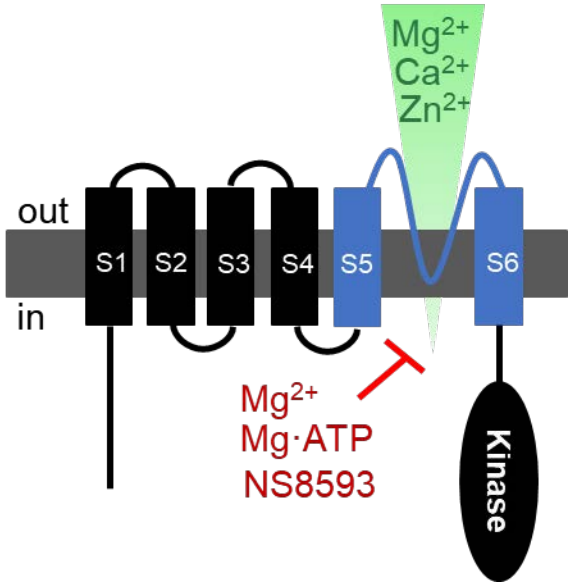

Figure 1. TRPM7 is a bifunctional plasma membrane protein.
The channel segment of TRPM7 contains six transmembrane helixes (S1–S6) linked to an α-type protein kinase domain. The channel pore-forming segment is located between the S5 and S6 helixes (in blue). The TRPM7 channel is permeable to Mg^{2+}, Ca^{2+}, and Zn^{2+} and is negatively regulated by Mg^{2+} and Mg·ATP. The small synthetic molecule NS8593 inhibits TRPM7 channel activity.

2.1 Functional characteristics of the TRPM7 channel

TRPM7 is a constitutively active channel that is highly permeable to divalent cations with the following preference: $Zn^{2+} \approx Ni^{2+} >> Ba^{2+} > Co^{2+} > Mg^{2+} \geq Mn^{2+} \geq Sr^{2+} \geq Cd^{2+} \geq Ca^{2+}$ [6, 12]. Intracellular Mg^{2+} and Mg·ATP have been shown to act as negative regulators of the TRPM7 channel [8-10]. Thus, a common strategy to induce TRPM7 currents in patch-clamp experiments is based on the application of EDTA/EGTA-containing intracellular pipette solutions, enabling the removal of intracellular Mg^{2+} and Mg·ATP, thereby activating TRPM7 currents [11, 12, 26]. It has been hypothesized that Mg^{2+} and Mg·ATP maintain a negative feedback mechanism linking the metabolic state of the cell and TRPM7-mediated uptake of divalent cations [11, 12, 26].

In addition to Mg^{2+} and Mg·ATP, the TRPM7 channel is regulated by phosphatidylinositol 4,5-bisphosphate (PIP_2). The activation of phospholipase C (PLC)

by G-protein-coupled receptors leads to PIP_2 depletion and, consequently, inactivation of the TRPM7 channel [27]. Other factors that modulate TRPM7 activity include intracellular and extracellular pH [28], mechanical stress [29-33], halogens [34], and osmolarity [35]

Alongside the aforementioned physiological factors regulating the TRPM7 channel, synthetic drug-like ligands of the TRPM7 channel have been discovered and have been used extensively to map the function of TRPM7 in cultured cells and model animals [36]. For instance, NS8593 is a potent inhibitor [36], while naltriben acts as an activator [37], allowing for instant modulation of TRPM7 channel activity in living cells. Other frequently used drug-like inhibitors of the TRPM7 channel are waixenicin A [38] and FTY720 [39].

2.2 Functional characteristics of the TRPM7 kinase

The TRPM7 kinase domain displays catalytic activity and is capable of phosphorylating serine and threonine residues in target proteins [40]. Several proteins have been suggested as physiological substrates of TRPM7 kinase, including TRPM6 [41], annexin I [42], several isoforms of myosin II [43], eEF2-K [44], phospholipase C gamma 2 (PLCγ2) [45], tropomodulin [46] and stromal interaction molecule 2 (STIM2) [4], mothers against decapentaplegic homolog (SMAD) 2/3 [47] and Ras homolog family member A (RhoA) [48]. In addition, the TRPM7 kinase domain can autophosphorylate its own serine and threonine residues primarily within a segment located upstream of the kinase domain itself [49, 50].

Annexin I, which is involved in membrane fusion, is phosphorylated by TRPM7, and this modification is thought to contribute to cell growth and apoptosis [42, 51]. The phosphorylation of myosin IIA, IIB, and IIC by TRPM7 kinase has been associated with

cell motility and adhesion [43, 52, 53]. Furthermore, the TRPM7-induced phosphorylation of eEF2K likely leads to an altered protein translation rate [44]. The phosphorylation of PLCγ2 by the TRPM7 kinase induces changes in PLCγ2 signaling [45]. TRPM7 kinase also phosphorylates tropomodulin, affecting the regulation of tropomodulin capping activity and, as a result, the dynamics of actin filaments [46]. The phosphorylation of STIM2 by the TRPM7 kinase domain leads to a modulatory effect of store-operated Ca^{2+} entry (SOCE) [4]. Additionally, the phosphorylation of SMAD2/3 through the TRPM7 kinase moiety plays a role in autoimmune and inflammatory disorders [47]. Lastly, RhoA can be phosphorylated and activated by the TRPM7 kinase moiety [48].

Despite the identification of these substrates, small molecules that selectively target the TRPM7 kinase remain to be identified. Song et al. introduced the organic compound TG100-115 as the first small inhibitor of TRPM7 kinase [54], though subsequent experiments revealed that TG100-115 also inhibits TRPM6 kinase [55].

2.3 Cellular processes regulated by TRPM7

The channel and kinase functions of TRPM7 were extensively investigated in cultured cells. Pioneering work examined DT40 chicken lymphocytes with the disabled *Trpm7* gene and showed that the loss of TRPM7 leads to a proliferation defect. This phenotype was reversible by Mg^{2+} supplementation, leading the authors to propose that the TRPM7 channel maintains the cellular equilibrium of Mg^{2+} and that this mechanism is crucial for the proliferation of DT40 cells [7, 12]. This phenotype has since been recapitulated in many mammalian cell lines, including mouse embryonic stem (ES) cells and trophoblast stem (TS) cells [56, 57], human embryonic kidney (HEK293T) cells [3] and human haploid leukemia (HAP1) cells [56]. Similar to research

on DT40 cells, supplementation of cell culture medium with Mg^{2+} (usually 10 mM Mg^{2+}) ameliorates the proliferation defect of TRPM7 gene-deficient cell lines [7, 56, 57].

Several studies have linked the TRPM7 channel to Ca^{2+} signaling [6, 12, 16, 57]. TRPM7 Ca^{2+} currents are essential in replenishing intracellular Ca^{2+} stores [4]. Additionally, TRPM7 was found to interact with the endoplasmic reticulum Ca^{2+} sensor STIM2, which activates the plasma membrane Ca^{2+} channels ORAI1 and ORAI2 [4]. It also has been discovered that TRPM7 plays a role in cytoplasmic Ca^{2+} oscillations in mouse eggs upon fertilization [24, 25] and modulates Ca^{2+} flickering in human embryonic lung fibroblasts [58].

Our group recently demonstrated that TRPM7 controls cellular Zn^{2+} balance in HAP1 cells [5]. Other researchers [3] reported that TRPM7 can be localized in uncharacterized intracellular vesicles enriched in glutathione and Zn^{2+}, referred to as M7V. These vesicles were distinct from endosomes or lysosomes and were suggested to act as intracellular Zn^{2+} stores regulated by TRPM7 [3]. Additionally, TRPM7 has been shown to maintain Zn^{2+} levels in mouse embryonic stem (ES) cells [59]. Reports show stress hormones enhancing the neurotoxicity of Zn^{2+} by increasing its influx through TRPM7 in human SH-SYS5Y cells [60].

Recent studies have implicated many other physiological and pathophysiological processes dependent on regulation by the TRPM7 channel, such as cell motility [43, 58, 61], mechanosensitivity [31, 32, 58], cell cycle [7, 12, 38, 62], hypertension [63], exocytosis [23], anoxic neuronal death [64], neurodegenerative disorders [65, 66], cardiac fibrosis [67], and cancer [68-71].

TRPM7 kinase also regulates several cellular processes, such as PLC activity, which influences B-cell receptor signaling in immune responses [45]. TRPM7 kinase controls TGF-β-mediated SMAD2 phosphorylation [47]. Inhibition of TRPM7 kinase

activity by a mutation within its active site (K1646R) results in a decrease in the production of $CD4^+$ T helper 17 (T_H17) lymphocytes, the known crucial regulators of autoimmune and inflammatory responses [47]. TRPM7's kinase domain has been shown to be split from the channel domain, to translocate in the nucleus and phosphorylate chromatin-remodeling proteins like histone H3, thus modulating the epigenetic landscape [59], likely depending on Zn^{2+} [3].

2.4 The physiological role of TRPM7 in animal genetic models

Experiments with animal genetic models showed the crucial role of TRPM7 in early prenatal development, tissue morphogenesis, and the organismal equilibrium of divalent cations [72]. Global inactivation of the *Trpm7* gene (*Trpm7* null mutation) leads to lethality at embryonic day 7.5 (e7.5) [72], emphasizing the critical role of TRPM7 in prenatal development. Mutant mice with conditional deletion of *Trpm7* in the embryonic heart at e9.0 displayed abnormal cardio genesis [73, 74], while conditional ablation of cardiac *Trpm7* between e9.0 and e12.5 did not induce histological changes but triggered ventricular arrhythmia, suggesting that TRPM7 controls cardiac automaticity in adult mice [73, 74]. Mice with *Trpm7* inactivation in the T-cell lineage display disrupted thymopoiesis [72] indicating a vital function of TRPM7 in immune system development.

TRPM7 plays a vital role in prenatal kidney morphogenesis [75]. It was found that deletion of *Trpm7* in the embryonic metanephric mesenchyme leads to a deficiency of TRPM7 protein in the renal tubules of the adult mice. Consequently, the mutant individuals develop morphological changes in the kidney with less glomeruli, dilatation of the renal tubules, and growth of cysts in the proximal tubules, indicating that *Trpm7* is essential for nephrogenesis [75]. Macrothrombocytopenia is a rare human disorder

combining enlarged platelets and thrombocytopenia. Megakaryocyte-specific inactivation of Trpm7 in mice also produces a macrothrombocytopenia-like phenotype, further highlighting the role of TRPM7 in platelet production and function [76].

More recently, our laboratory has shown the crucial role of the TRPM7 channel in intestinal absorption of divalent cations such as Zn^{2+}, $Mg^{2+,}$ and Ca^{2+}. Thus, enterocyte-restricted deletion of *Trpm7* in mice caused early postnatal growth arrest and mortality. Mutant pups displayed reduced levels of Zn^{2+}, $Ca^{2+,}$ and Mg^{2+} in serum and bones. Remarkably, dietary Zn^{2+} and Mg^{2+} supplementation of breastfeeding mothers significantly extended the survival rate of mutant pups [5].

The inactivation of TRPM7 α-kinase activity by a point mutation within its active site (K1646R, $Trpm7^{R/R}$) showed no effect on embryonic development, tissue morphogenesis, postnatal survival [77], nor did it influence Ca^{2+} and Mg^{2+} serum levels, indicating that the phenotypes of mice with *Trpm7* null mutations were mainly triggered by the lack of TRPM7 channel activity. Interestingly, Ryazanova et al. [78] hypothesized that the TRPM7 kinase functions as a sensor of Mg^{2+} levels in the organism since they found that adult $Trpm7^{R/R}$ mice are more resistant to dietary Mg^{2+} withholding [78].

Taken together, these findings underscore the crucial role of TRPM7 channel in maintaining the homeostasis of divalent cations, particularly Mg^{2+} and Zn^{2+}. Inactivation of TRPM7 leads to imbalances in divalent cation homeostasis which can contribute to various human diseases.

2.5 Research goals

In this project, we aimed to investigate the mechanisms of TRPM7 channel regulation by intracellular Mg^{2+} and to identify the cellular pathways influenced by TRPM7 channel activity.

In particular, we sought to address the following key questions:

1. What are mechanisms of Mg^{2+} inhibition of the TRPM7 channel? (Publication II)
2. What are the cellular pathways regulated by the TRPM7 channel? (Publication I)
3. Are these pathways dependent on TRPM7-mediated entry of Zn^{2+}? (Publication I)
4. What is the therapeutic relevance of TRPM7 inhibition in cancer cells? (Publication I)

3. Abstract

Previous research has indicated that the plasma membrane channel kinase Transient Receptor Potential Cation Channel Subfamily M Member 7 (TRPM7) is involved in the uptake of divalent cations, including Zn^{2+}, Mg^{2+}, and Ca^{2+} [3-7], which are required for many cellular processes. Studies with cultured cells and animal disease models demonstrated that inactivation of TRPM7 led to impaired proliferation of cancer cells. However, mechanistically, the role of TRPM7 in tumour progression remains poorly understood. In our study, we conducted electrophysiological and cell biological experiments to investigate how intracellular Mg^{2+} interacts directly with TRPM7, leading to the inhibition of TRPM7 currents. In addition, we used genome-wide transcriptome profiling of haploid human leukemia (HAP1) cells to identify cellular pathways altered upon introduction of loss-of-function mutations in the *TRPM7* gene using the CRISPR/Cas9 approach or the administration of a pharmacological inhibitor of the TRPM7 channels, NS8593. Notably, among the affected gene networks, we observed that the expression levels of human epidermal growth factor receptor *HER2* (*ERRB2*), a well-known oncogene in breast cancer, were altered upon TRPM7 inhibition. Consequently, we examined the interplay of TRPM7 and HER2 in several cell lines and found that TRPM7 mediates Zn^{2+}-dependent downregulation of HER2 protein levels. In addition, we observed that simultaneous administration of CP724714 (an inhibitor of HER2) and NS8593 (a TRPM7 inhibitor) synergistically suppressed the proliferation of HER2-positive SKBR3 cells but not HER2-negative MDA-MB-231 cells. Our study, therefore, provides new insights into the regulatory mechanisms of the TRPM7 channel and uncovers new cellular counterparts of TRPM7. We demonstrate that the inhibition of TRPM7, in combination with HER2-targeted therapy, can more effectively suppress the proliferation of HER2-positive breast cancer cells.

4. Zusammenfassung

Bisherige Forschungen haben gezeigt, dass die Plasmamembrankanalkinase TRPM7 an der Aufnahme essenzieller bivalenter Kationen wie Zn^{2+}, Mg^{2+} und Ca^{2+} beteiligt ist [3-7], die für zelluläre Prozesse von entscheidender Bedeutung sind. Unabhängige Studien mit kultivierten Zellen und Tiermodellen haben gezeigt, dass die Inaktivierung von TRPM7 zu einer eingeschränkten Proliferation von Krebszellen führt. Der Mechanismus von TRPM7 bei der Tumorentwicklung ist jedoch nach wie vor wenig verstanden. In unserer Studie haben wir elektrophysiologische und zellbiologische Experimente durchgeführt, um zu erforschen, wie intrazelluläres Mg^{2+} direkt mit dem unteren Gate von TRPM7 interagiert, was zu einer Hemmung der Kanalaktivität führt. Darüber hinaus haben wir ein genomweites Transkriptom-Profiling haploider menschlicher Leukämiezellen (HAP1) durchgeführt, um zelluläre Signalwege zu identifizieren, die sich nach der Insertion von Loss-of-Function-Mutationen im *TRPM7-Gen* mithilfe des CRISPR/Cas9-Ansatzes oder der Verabreichung eines pharmakologischen Inhibitors der TRPM7-Kanäle, NS8593, verändern. Unter den betroffenen Gennetzwerken stellten wir fest, dass die Expressionswerte des menschlichen epidermalen Wachstumsfaktorrezeptors 2, HER2 (ERRB2), eines kritischen Onkogens bei Brustkrebs, durch die Inhibition von TRPM7 verändert wurden. Daraufhin untersuchten wir das Zusammenspiel von TRPM7 und HER2 in mehreren Zelllinien und stellten fest, dass TRPM7 eine Zn^{2+}-abhängige Herabregulierung von HER2 bewirkt.

Darüber hinaus konnten wir beobachten, dass die gleichzeitige Verabreichung von CP724714 (einem HER2-Inhibitor) und NS8593 (einem TRPM7-Inhibitor) die Proliferation von HER2-positiven SKBR3-Zellen, nicht aber von HER2-negativen MDA-MB-231-Zellen synergistisch unterdrückte.

Unsere Studie bietet daher neue Einblicke in die Regulationsmechanismen des TRPM7-Kanals und deckt neue zelluläre Gegenspieler von TRPM7 in Krebszellen auf. Wir zeigen, dass die Hemmung von TRPM7 in Kombination mit einer auf HER2 ausgerichteten Therapie die Proliferation von HER2-positiven Brustkrebszellen wirksam unterdrücken kann.

5. Publication I

Title: Expression Profiling Identified TRPM7 and HER2 as Potential Targets for the Combined Treatment of Cancer Cells

https://doi.org/10.3390/cells13211801

cells

MDPI

Article

Expression Profiling Identified TRPM7 and HER2 as Potential Targets for the Combined Treatment of Cancer Cells

Miyuki Egawa [1], Eva Schmücker [1], Christian Grimm [1,2], Thomas Gudermann [1,3,*] and Vladimir Chubanov [1,*]

[1] Walther-Straub Institute of Pharmacology and Toxicology, Ludwig Maximilian University of Munich, 80336 Munich, Germany; miyuki.egawa@campus.lmu.de (M.E.); eva_schmuecker@gmx.de (E.S.); christian.grimm@med.uni-muenchen.de (C.G.)
[2] Immunology, Infection and Pandemic Research IIP, Fraunhofer Institute for Translational Medicine and Pharmacology ITMP, 80799 Munich, Germany
[3] Comprehensive Pneumology Center, German Center for Lung Research (DZL), 81377 Munich, Germany
* Correspondence: thomas.gudermann@lrz.uni-muenchen.de (T.G.); vladimir.chubanov@lrz.uni-muenchen.de (V.C.)

Abstract: TRPM7 is a divalent cation-permeable channel that is highly active in cancer cells. The pharmacological inhibitors of TRPM7 have been shown to suppress the proliferation of tumor cells, highlighting TRPM7 as a new anticancer drug target. However, the potential benefit of combining TRPM7 inhibitors with conventional anticancer therapies remains unexplored. Here, we used genome-wide transcriptome profiling of human leukemia HAP1 cells to examine cellular responses caused by the application of NS8593, the potent inhibitor of the TRPM7 channel, in comparison with two independent knockout mutations in the *TRPM7* gene introduced by the CRISPR/Cas9 approach. This analysis revealed that *TRPM7* regulates the expression levels of several transcripts, including *HER2* (*ERBB2*). Consequently, we examined the *TRPM7/HER2* axis in several non-hematopoietic cells to show that TRPM7 affects the expression of HER2 protein in a Zn^{2+}-dependent fashion. Moreover, we found that co-administration of pharmacological inhibitors of HER2 and TRPM7 elicited a synergistic antiproliferative effect on HER2-overexpressing SKBR3 cells but not on HER2-deficient MDA-MB-231 breast cancer cells. Hence, our study proposes a new combinatorial strategy for treating HER2-positive breast cancer cells.

Keywords: TRP channels; HER2; ERBB2; NS8593; CP724714; zinc; breast cancer

Citation: Egawa, M.; Schmücker, E.; Grimm, C.; Gudermann, T.; Chubanov, V. Expression Profiling Identified TRPM7 and HER2 as Potential Targets for the Combined Treatment of Cancer Cells. *Cells* **2024**, *13*, 1801. https://doi.org/10.3390/cells13211801

Academic Editor: Ludger Hengst

Received: 3 July 2024
Revised: 21 October 2024
Accepted: 28 October 2024
Published: 31 October 2024

1. Introduction

The transient receptor potential cation channel, subfamily M, member 7 (TRPM7), is a bifunctional protein containing a membrane-spanning cation channel segment fused to a cytosolic protein kinase domain [1–4]. Electrophysiological experiments demonstrated that TRPM7 forms a constitutively active channel, which is highly permeable to divalent cations, including Zn^{2+}, Mg^{2+}, and Ca^{2+} [5–9]. Independent evidence supports the notion that the TRPM7 channel represents the main route for the cellular uptake of divalent cations, especially Mg^{2+} and Zn^{2+} [10–14]. In line with this assumption, the genetic disruption of TRPM7 causes cell cycle arrest [10–12]. In addition to the homeostatic control of Mg^{2+}, the TRPM7 channel regulates multiple Zn^{2+}- and Ca^{2+}-regulated pathways pertinent to cancer progression [15–20].

The kinase domain of TRPM7 belongs to the atypical group serine/threonine-protein kinases entitled α-kinases (or alpha-protein kinases) [4,21–23]. TRPM7 and its close homologous protein TRPM6 are the only known ion channels covalently fused to kinase domains [2,4]. In addition, four other human proteins contain α-kinase domains, including eukaryotic elongation factor-2 kinase (eEF-2K) and alpha-protein kinases 1–3 (ALPK1–3) [21–23]. The identified phosphorylation substrates of TRPM7 kinase comprise a set of functionally heterogeneous

proteins like TRPM6, annexin A1, myosin II, eEF-2K, tropomodulin, PLCγ2, STIM2, SMAD2, RhoA, and CREB [1–3,22,23].

Several drug-like molecules were identified as potent modulators of the TRPM7 channel [24–28]. Among them, NS8593, waixenicin A, and FTY720 represent the most comprehensively characterized inhibitors of the TRPM7 channel [25,29–32]. Recently, cryogenic electron microscopy (cryo-EM) structures of the TRPM7 channel in active open and inactive closed states were solved [4,33,34]. In addition, cryo-EM identified the binding site of NS8593 and delineated the molecular mechanism underlying its inhibitory impact on the TRPM7 channel [4,34]. Mechanistically, the pharmacological effects of waixenicin A and FTY720 on TRPM7 remain less understood.

NS8593 was extensively used to dissect cellular functions of the TRPM7 channel in different physiological and pathophysiological settings, including animal models of human diseases [25,35,36]. One of the most noticeable findings is that NS8593 showed inhibitory effects on the proliferation of cancer cells [10,20,35,37–41]. Additionally, many investigators used NS8593 or other TRPM7 inhibitors, often in combination with RNAi silencing of *TRPM7*, to demonstrate the crucial role of TRPM7 in signaling pathways and cellular processes linked to tumor progression [25,35,38,40,42–45], including breast cancer [38,46–51]. These findings correlate well with genetic, histological and bioinformatic analysis of human tissue samples, suggesting TRPM7 is aberrantly expressed in many cancer types and can serve as a prognosis marker of the disease progression and survival of the patients [52–56]. Consequently, TRPM7 has been proposed as a new anti-cancer drug target [56–58].

In the present study, we conducted transcriptome profiling of human leukemia HAP1 cells to characterize cellular responses after genetic inactivation and pharmacological inhibition of TRPM7. In follow-up experiments with HAP1 cells and different cancer cells, we found that TRPM7 regulates the expression of HER2 and that this regulatory mechanism can be exploited for combinatorial pharmacological treatment of HER2-expressing breast cancer cells.

2. Materials and Methods

2.1. Pharmacological Agents

NS8593 and CP724714 were acquired from Tocris, Bristol, UK. $ZnCl_2$ and zinc pyrithione (#PHR1401) were purchased from Merck, Darmstadt, Germany.

2.2. HAP1 Cells

Parental (herein referred to as wild-type (WT) cells) and *TRPM7* knockout (*TRPM7* KO) human haploid leukemia (HAP1) cells were acquired from Horizon Discovery (Cambridge, UK). The genetic and functional characterization of clone 10940–04 (referred to as *TRPM7* KO-04) was described previously [12,39]. A CRISPR/Cas9 approach was used to introduce a 17 bp (GTGACCATTTTAATCAG) deletion in exon 4 of the human *TRPM7* gene, resulting in a frame-shift mutation [12,39]. The clone 10940–01 of HAP1 cells (referred to as *TRPM7* KO-01) was characterized in the present study. A 16 bp targeting sequence (AAAATGGTCACCCAAT) was selected to modify the exon 4 of *TRPM7* using the CRISPR/Cas9 technique. The *TRPM7* KO-01 clone was examined by RT-PCR approach using *hTRPM7*-Forward 5′-GGAGTCCGCCCCGTGAGG-3′ and *hTRPM7*-Reverse 5′-TGACTTCCGCCCCATACTTTCCAACAG-3′ primers and the following PCR settings: 95 °C 30″, 63 °C 15″, 72 °C 90″. The obtained PCR products were isolated from the gel, purified and sequenced. The sequence of PCR product from WT cells matched to *TRPM7* mRNA. The PCR product from *TRPM7* KO-01 cells contained a sequence of exon 3, which was aberrantly spliced to an intronic sequence followed by a sequence from the distal part of exon 4 of *TRPM7* (Supplementary Figure S1). In silico translation of the mutant cDNA revealed a frame-shift mutation in *TRPM7*.

2.3. Cell Cultures

HAP1 cells were cultured in IMDM supplemented with 10% fetal bovine serum (FBS), 100 U/mL penicillin and 100 µg/mL streptomycin mixture (all from Merck, Darmstadt, Germany). Unless indicated otherwise, *TRPM7* KO-01 and KO-04 HAP1 cells were supplemented with 10 mM $MgCl_2$ included in the regular cell culture medium.

WT and *TRPM7* knockout (*TRPM7* KO) mouse trophoblast stem (TS) cells were derived from mouse blastocysts as described earlier [39]. TS cells were cultured in RPMI 1640 medium (Merck, Darmstadt, Germany) supplemented with 20% FBS (ES type, Life Technologies, Darmstadt, Germany), 1 mM sodium pyruvate (cell culture type, Merck, Darmstadt, Germany), 100 mM β-mercaptoethanol (Merck, Darmstadt, Germany), 50 µg/mL streptomycin (Merck, Darmstadt, Germany), 50 U/mL penicillin (Merck, Darmstadt, Germany), 1.0 mg/mL heparin (cell culture type, Merck, Darmstadt, Germany), 25 ng/mL human recombinant FGF4, 5 ng/mL human recombinant TGF-β1, and 10 ng/mL recombinant activin A (all from R&D systems, Minneapolis, MN, USA). Cells were maintained in a humidified cell culture incubator (Heraeus, Thermo Fisher Scientific, Waltham, MA, USA) at 37 °C and 5% CO_2.

TRPM7 KO HEK293 cells were described previously [15]. WT and *TRPM7* KO HEK293 cells were maintained in DMEM supplemented with 10% FBS, 100 µg/mL streptomycin, and 100 U/mL penicillin (all from Merck, Darmstadt, Germany). WT and *TRPM7* KO HeLa cells were acquired from Abcam (Cambridge, UK; ab265480). The frame-shift mutation in exon 14 of *TRPM7* was introduced using CRISPR/Cas9. WT and *TRPM7* KO HeLa cells were maintained in DMEM supplemented with 10% FBS, 100 µg/mL streptomycin, and 100 U/mL penicillin (all from Merck, Darmstadt, Germany). MCF-7, MDA-MB-231, and SKBR3 cells (all from DSMZ-German Collection of Microorganisms and Cell Cultures, Brunswick, Germany) were maintained in RPMI 1640 medium containing 10% FBS, 100 U/mL penicillin, 100 µg/mL streptomycin (all from Merck, Darmstadt, Germany).

2.4. Genome-Wide Transcriptome Profiling and qRT-PCR Analysis

To study the impact of *TRPM7* KO mutations and NS8593 on transcriptome of HAP1 cells, WT, *TRPM7* KO-01, and KO-04 cells were maintained in 25 cm^2 flasks (Sarstedt, Nümbrecht, Germany) with IMDM containing 10% fetal bovine serum (FBS), 100 U/mL penicillin, and 100 µg/mL streptomycin (all from Thermo Fisher Scientific, Waltham, MA, USA) supplemented with 10 mM $MgCl_2$ (IMDM-Mg). At ~50% confluence, the IMDM-Mg was exchanged for the regular IMDM. The cells were cultured for an additional 24 h. To extract total RNA, the medium was removed, and the cells were immediately exposed to a lysis solution followed by RNA purification using the GenElute Mammalian Total RNA Miniprep kit (Merck, Darmstadt, Germany).

To investigate the effect of NS8593, WT HAP1 cells were maintained in IMDM-Mg (to match conditions used for *TRPM7* KO cells). Next, the cells were incubated in regular IMDM containing NS8593 for 24 h, and total RNA was extracted as described above. Whole genome profiling was performed using a GeneChip Human Gene 1.0 ST Array (Affymetrix, Santa Clara, CA, USA) at Source Bioscience (Nottingham, UK) as described previously [12,39]. Processing of the array data, quality assessment, background correction, and normalization were performed with the Affymetrix Expression Console (version 1.4.0). Differential expression analysis was performed with DNASTAR ArrayStar 11.0 software (Supplementary Table S1). DNASTAR ArrayStar 11.0 software was also used to generate Venn diagrams for transcripts showing $\geq$ 1.5-fold changes in samples from *TRPM7* KO and NS8593-treated WT cells as compared to WT HAP1 cells and to select transcripts commonly affected in KO-01, KO-04, and NS8593-treated WT HAP1 cells versus WT cells (Supplementary Table S2). Microarray data were deposited in NCBI Gene Expression Omnibus (GEO) (GSE203013).

For qRT-PCR analysis, RNA was extracted with GenElute Mammalian Total RNA Miniprep Kit (Merck, Darmstadt, Germany). The PCR primer pairs (Metabion, Planegg, Germany) used are shown in Supplementary Table S3. The first strand cDNA synthesis was

generated using the Thermo Scientific RevertAid H Minus First Strand cDNA Synthesis Kit (Thermo Fisher Scientific, Waltham, MA, USA). qPCR reactions were performed using the Thermo Scientific Absolute qPCR SYBR Green Mix (Thermo Fisher Scientific, Waltham, MA, USA) and a LightCycler 480 (Roche, Basel, Switzerland) with the following PCR settings: 95 °C 15′, 95 °C 15″, 60 °C 15″, 72 °C 30″. The cycle thresholds (CT) of the test and reference (*HPRT*) genes were calculated using LightCycler 480 software (version 1.5.0, Roche, Basel, Switzerland). The relative mRNA expression levels were calculated using the $2^{-\Delta\Delta CT}$ approach.

2.5. siRNA Targeting of TRPM7

HEK293 and SKBR3 cells were seeded in 6-well plates (Sarstedt, Nümbrecht, Germany) (~10^5 cells/well). The next day, the cells were transiently transfected with 20 nM FlexiTube siRNAs silencing *TRPM7*: Hs_*TRPM7*_7 FlexiTube siRNA (siRNA #7), Hs_*TRPM7*_8 FlexiTube siRNA (siRNA #8), and AllStars Negative Control siRNA (all from QIAGEN, Hilden, Germany) using Lipofectamine 2000 reagent (Thermo Fisher Scientific, Waltham, MA, USA). The cells were analyzed 72 h after transfection.

2.6. Electrophysiological Techniques

Patch-clamp experiments were performed and analyzed as reported previously [4,24,28,59]. Briefly, whole-cell currents were recorded using an EPC10 patch-clamp amplifier (Harvard Bioscience, Holliston, MA, USA) and PatchMaster software (version V2x69, Harvard Bioscience, Holliston, MA, USA). Voltages were corrected for a liquid junction potential of 10 mV. Currents were elicited by voltage ramps from −100 mV to +100 mV over 50 ms applied every 2 s. The inward and outward current amplitudes were measured at −80 mV and +80 mV and were normalized to the cell size as pA/pF. The capacitance was measured using the automated capacitance cancellation function of EPC10. The standard extracellular solution contained 140 mM NaCl, 2.8 mM KCl, 3 mM $CaCl_2$, 10 mM HEPES-NaOH, and 11 mM glucose (all from Merck, Darmstadt, Germany). Solutions were adjusted to pH 7.2 using an FE20 pH meter (Mettler Toledo, Columbus, OH, USA) and to 290 mOsm using a Vapro 5520 osmometer (Wescor Inc, South Logan, UT, USA). Patch pipettes were made of borosilicate glass (Science Products, Hofheim, Germany) and had a resistance of 2.0−3.7 MΩ when filled with the standard intracellular pipette solution containing 120 mM Cs-glutamate, 8 mM NaCl, 10 mM Cs-EGTA, 5 mM Cs-EDTA, and 10 mM HEPES-CsOH (all from Merck, Darmstadt, Germany). The intracellular solution was also adjusted to pH 7.2 and 290 mOsm.

2.7. Aequorin-Based Ca^{2+} Influx Assay

Measurements of $[Ca^{2+}]_i$ in TRPM7 expressing cells were performed and analyzed as reported previously [4,28]. HEK293 cells were maintained at 37 °C and 5% CO_2 in DMEM supplemented with 10% FBS, 100 µg/mL streptomycin, and 100 U/mL penicillin (all from Merck, Darmstadt, Germany). Cells cultured in 6-well plates (~60% confluence) were transfected with 2 µg/dish *Trpm7* plasmid DNA and 0.1 µg/dish *pG5A* plasmid DNA encoding eGFP fused to *Aequorea victoria* aequorin, using Lipofectamine 2000 (Thermo Fisher Scientific, Waltham, MA, USA). Twenty-four hours after transfection, the cells were washed with Mg^{2+}-free HEPES-buffered saline (Mg^{2+}-free HBS) containing 150 mM NaCl, 5.4 mM KCl, 0.5 mM $CaCl_2$, 5 mM HEPES (pH 7.4), and 10 mM glucose, and mechanically resuspended in the Mg^{2+}-free HBS. For reconstitution of aequorin, cell suspensions were incubated with 5 µg/mL coelenterazine (Carl Roth, Karlsruhe, Germany) in the Mg^{2+}-free HBS for 30 min at room temperature. Cells were washed twice by centrifugation at 2000 rpm for 5 min (Heraeus Pico 17 microcentrifuge, Thermo Fisher Scientific, Waltham, MA, USA), resuspended in the Mg^{2+}-free HBS and aliquoted into 96-well plates (1×10^5 cells per well). Luminescence was detected at room temperature using a CLARIOstar microplate reader (BMG LABTECH GmbH, Ortenberg, Germany). To monitor the effects of CP724714 and NS8593, the extracellular concentration of Ca^{2+} was increased to 5 mM by injecting the

$CaCl_2$-containing Mg^{2+}-free HBS in the absence or presence of the inhibitors. The experiments were terminated by lysing cells with 0.05% (*v*/*v*) Triton X-100 in the Mg^{2+}-free HBS to record the total bioluminescence. The bioluminescence rates (counts/s) were analyzed at 1-s intervals and calibrated as $[Ca^{2+}]_i$ values using the following equation:

$$p[Ca^{2+}]_i = 0.332588\ (-\log(k)) + 5.5593 \quad (1)$$

where *k* represents the rate of aequorin consumption, i.e., counts/s divided by the total number of counts.

2.8. Assessment of Cell Viability

To study the impact of Mg^{2+} supplementation on the growth rate of WT and *TRPM7* KO HAP1 cells (Figure 1A), the cells of each genotype were seeded in 6-well plates (10^5 cells/well) in a standard culture medium supplemented with 10 mM $MgCl_2$. After 24 h, the cell culture medium was replaced by the fresh medium with or without additional Mg^{2+}, and the cell counts were determined at 24 h intervals using a Neubauer chamber (Marienfeld Superior, Lauda-Königshofen, Germany). The cell density at day 1 was accounted as 100%.

To examine the antiproliferative effects of NS8593 on HAP1 cells, the cells were seeded in a 96-well plate (5×10^3 cells/well) in the standard culture medium supplemented with 10 mM $MgCl_2$. After 24 h, the culture medium was replaced with the fresh medium with or without 10 mM $MgCl_2$ and indicated concentrations of NS8593. The cells were further cultured for an additional 72 h. Cell Counting Kit-8 (CCK-8, Selleck Biotechnology, Frankfurt am Main, Germany) was used to determine cell density according to the manufacturer's protocol.

To assess the antiproliferative effects of NS8593 and CP724714 on breast cancer cells, SKBR3, and MDA-MB-231 cells were seeded in 96-well plates (2×10^4 cells/well) in the standard cell culture medium. After 24 h, the indicated concentrations of NS8593 and CP724714 were added to the cell culture medium and the cells were incubated for an additional 72 h. The cell density was determined using a Neubauer chamber. The synergy in the effects of NS8593 and CP724714 was assessed using the LOEWE model (Combenefit 2.021 software [60]).

2.9. Western Blot (WB) Analysis

To assess the effects of Zn^{2+} and zinc pyrithione on HER2 expression, HAP1 cells were seeded in a 6-well plate (10^5 cells/well) and cultured for 72 h in the presence or absence of the supplements. After the treatment, the culture medium was removed by aspiration, and the cells were disrupted using a lysis buffer (Pierce IP Lysis Buffer, Thermo Fisher Scientific, Waltham, MA, USA; #87787) containing protease and phosphatase inhibitor cocktails (Selleck Biotechnology, Frankfurt am Main, Germany). Aliquots of the cell lysates were mixed (1:1) with 2 x *Laemmli* buffer, heated at 70 °C for 10 min and cooled on ice. The samples were separated by SDS-PAGE (4–20% gradient acrylamide/bis-acrylamide, Bio-Rad, Feldkirchen, Germany) and electroblotted on nitrocellulose membranes (Merck, Darmstadt, Germany; #GE10600002). After blocking with 5% (*w*/*v*) non-fat dry milk in Tris-buffered saline with 0.1% Tween 20 (TBST), the upper part of the membrane was probed by a rabbit monoclonal anti-HER2 antibody (Cell Signaling Technology, Danvers, MA, USA; #2165, 1:2000) in TBST with 5% (*w*/*v*) bovine serum albumin (BSA; Merck, Darmstadt, Germany) overnight at 4 °C, followed by triple washing steps in TBST, incubation with a horseradish peroxidase-coupled anti-rabbit lgG (Cell Signaling Technology, Danvers, MA, USA; #7074V, 1:1000) in TBST with 5% (*w/v*) BSA for 1 h at r.t. and washing in TBST. The lower part of the membrane was assessed by the anti-mouse monoclonal anti-β-Actin-Peroxidase (Merck, Darmstadt, Germany; #A3854, 1:100,000) in TBST with 5% (*w*/*v*) BSA for 1 h at r.t. and triple washing steps in TBST. Blots were examined by the luminescence imager ChemiDoc (Bio-Rad, Feldkirchen, Germany). The HER2 signal was normalized to the signal obtained with the mouse monoclonal anti-β-Actin-Peroxidase (Merck, Darmstadt, Germany; #A3854, 1:100,000) using the Image Studio Lite Ver 5.2 software. WB analysis of HER2 expression in other cells was conducted similarly.

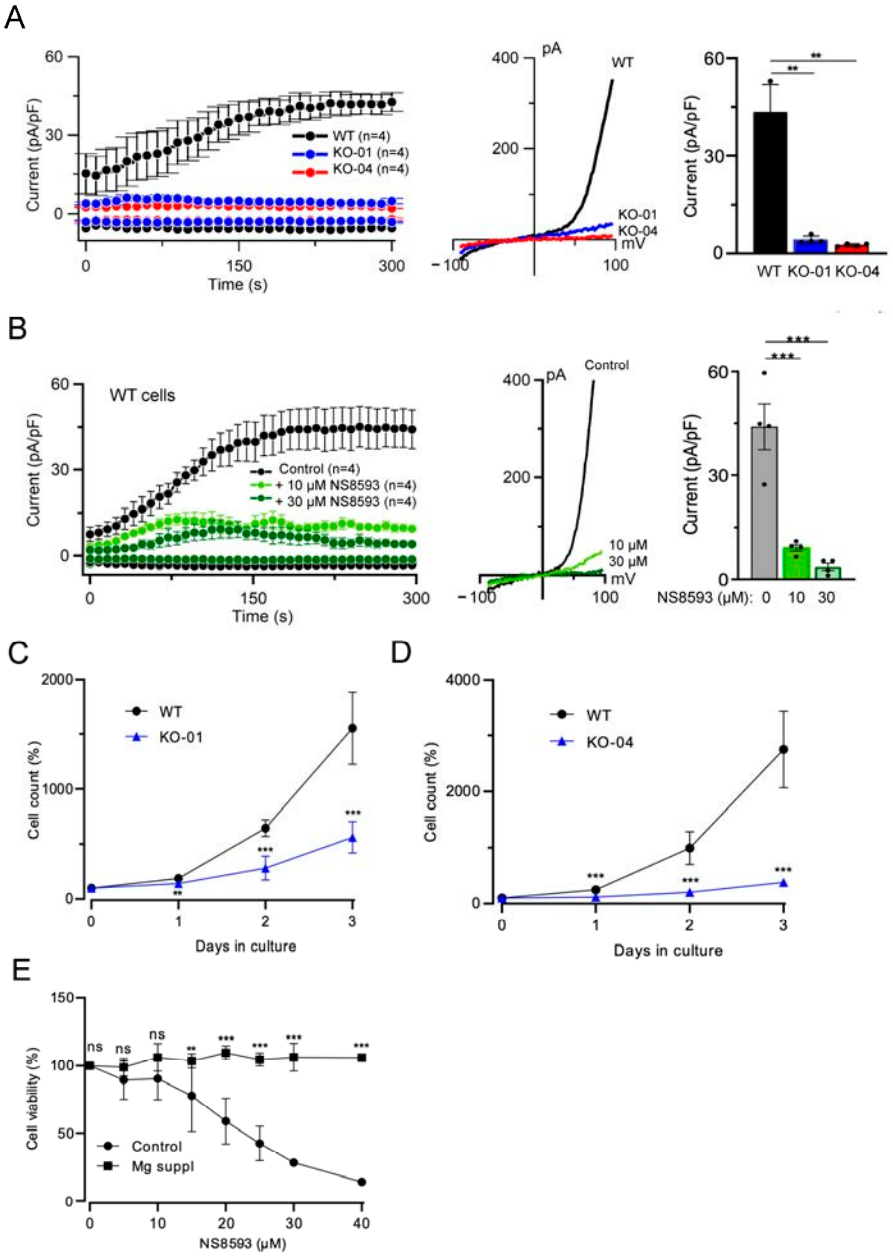

Figure 1. Assessment of human leukemia HAP1 cells. (**A**) Left panel: Whole-cell currents measured at −80 and +80 mV over time in WT (WT) and two *TRPM7* KO (KO-01 and KO-04) HAP1 cell lines. Middle panel: Representative current−voltage (I−V) relationships obtained at 300 s in measurements illustrated on the Left panel. Right panel: Bar graphs of current amplitudes at +80 mV (300 s) illustrated on the Left panel. Data are mean ± SD; *n*, the number of cells examined. ** $p \leq 0.01$ (one-way ANOVA). (**B**) Left panel: Whole-cell currents measured at −80 and +80 mV over time in WT HAP1 cells in the absence (Control) and the presence of 10 or 30 μM NS8593. Middle panel: Representative I−V relationships obtained at 300 s in measurements illustrated on the Left panel. Right panel: Bar graphs of current amplitudes at +80 mV (300 s) illustrated on the Left panel. Data are mean ± SD; *n*, the number of cells examined. *** $p \leq 0.001$ (one-way ANOVA). (**C**,**D**) Proliferation rate of WT and *TRPM7* KO-01 (**C**) and KO-04 (**D**) HAP1 cells. The cells were cultured for 3 days in the regular cell culture medium. The initial cell density (Day 0) was accounted as 100%. Data are mean ± SD of $n = 3$ independent experiments. *** $p \leq 0.001$; ** $p \leq 0.01$ (*t*-test). (**E**) Viability of WT HAP1 cells maintained in regular cell culture medium (Control) or medium with an additional 10 mM $MgCl_2$ (Mg suppl) containing different concentrations of NS8593 for 72 h. Cell densities in the absence of NS8593 were accounted as 100%. Data are mean ± SD of $n = 3$ independent experiments. *** $p \leq 0.001$; ** $p \leq 0.01$; ns—not significantly different (*t*-test).

2.10. Statistical Analysis

Data are presented as the means ± standard deviation (SD). Data showed a normal distribution. Data were compared using a two-tailed *t*-test. For multiple comparisons, an ANOVA (GraphPad Prism 10.1.2 software) was used. Significance was accepted at $p \leq 0.05$.

3. Results

3.1. Genetic and Pharmacological Inactivation of TRPM7 Suppresses the Proliferation of Human Leukemia HAP1 Cells

In previous studies, we employed a human leukemia HAP1 cell line (referred to as clone KO-04) carrying a frame-shift mutation in the *TRPM7* gene [12,39]. Because clonal selection can produce a considerable diversity of cell phenotypes, we took advantage of an alternative HAP1 cell line with a frame-shift mutation in *TRPM7* (clone KO-01) (Supplementary Figure S1). TRPM7 functions as a constitutively active cation channel, which is negatively regulated by intracellular Mg^{2+} through a regulatory site located in the lower channel gate of TRPM7 [2,59]. In patch-clamp measurements, the induction of whole-cell TRPM7 currents is achieved by removing cytosolic Mg^{2+} using EDTA-containing patch pipette solutions [2]. We applied this approach to characterize HAP1 cells. Patch-clamp measurements with parental WT HAP1 cells (clone WT-C631) revealed characteristic endogenous TRPM7 currents, which were entirely abrogated in both *TRPM7* knockout (KO) cell lines (Figure 1A).

Because frame-shift mutations in *TRPM7* permanently eliminate channel and kinase activities of TRPM7, we asked whether NS8593, a potent inhibitor of the TRPM7 channel [29,35], can serve as an alternative strategy to block the TRPM7 channel in HAP1 cells acutely. We observed that exposure of WT HAP1 cells to 10 or 30 μM NS8593 markedly suppressed the TRPM7 currents (Figure 1B).

In accordance with previous studies [10–12], we found that *TRPM7* KO HAP1 cells grow normally in a cell culture medium containing an additional 10 mM Mg^{2+}. However, we observed that maintaining *TRPM7* KO HAP1 cells in a regular cell culture medium suppressed the proliferation of KO-01 and KO-04 cell lines and that this effect was well noticeable after 48 h of the medium's replacement (Figure 1C,D). Next, we cultured WT HAP1 cells in the regular cell culture medium containing different concentrations of NS8593 for 72 h and observed concentration-dependent inhibition of cell growth (Figure 1E). However, the proliferation of NS8593-treated HAP1 cells was fully normalized in the Mg^{2+}-supplemented medium (Figure 1E).

Hence, the pharmacological inhibition of the TRPM7 channel replicated the effects of *TRPM7* KO mutations on endogenous TRPM7 currents and the proliferation of HAP1 cells.

3.2. Gene Expression Profiling of HAP1 Cells Reveals New Regulatory Targets of TRPM7

Previously, we conducted genome-wide transcriptome profiling of mouse tissues to investigate organismal responses upon deleting the *Trpm6* and *Trpm7* genes in mice [12,39]. In the present study, we applied this approach to uncover cellular pathways affected by the deletion of the *TRPM7* gene in HAP1 cells. We cultured the parental WT HAP1 cells and two *TRPM7* KO clones in the regular cell culture medium (without additional 10 mM Mg^{2+}) for 24 h, the incubation time preceding the growth defect of *TRPM7* KO cells (Figure 1C,D). Consequently, RNA was acutely extracted from adherent cells, and transcriptome profiling was performed analogously to our previous studies [12,39]. Applying a cut-off value of 1.5-fold changes, we identified 274 up- and 201 down-regulated genes in *TRPM7* KO-01 cells compared to WT HAP1 cells (Figure 2A, Supplementary Table S1). A similar analysis of *TRPM7* KO-04 cells revealed 473 up- and 221 down-regulated genes (Figure 2A, Supplementary Table S1). Among other transcripts, we noted that the receptor tyrosine-protein kinase *HER2* gene (*ERBB2*) expression was remarkably up-regulated in both *TRPM7* KO clones (Supplementary Table S1). Interestingly, transcripts of α-kinases eEF-2K and ALPK1–3 were detected in HAP1 cells (Supplementary Table S1), but the expression levels of only *ALPK1* were increased in either of the *TRPM7* KO cell lines (Supplementary Table S2).

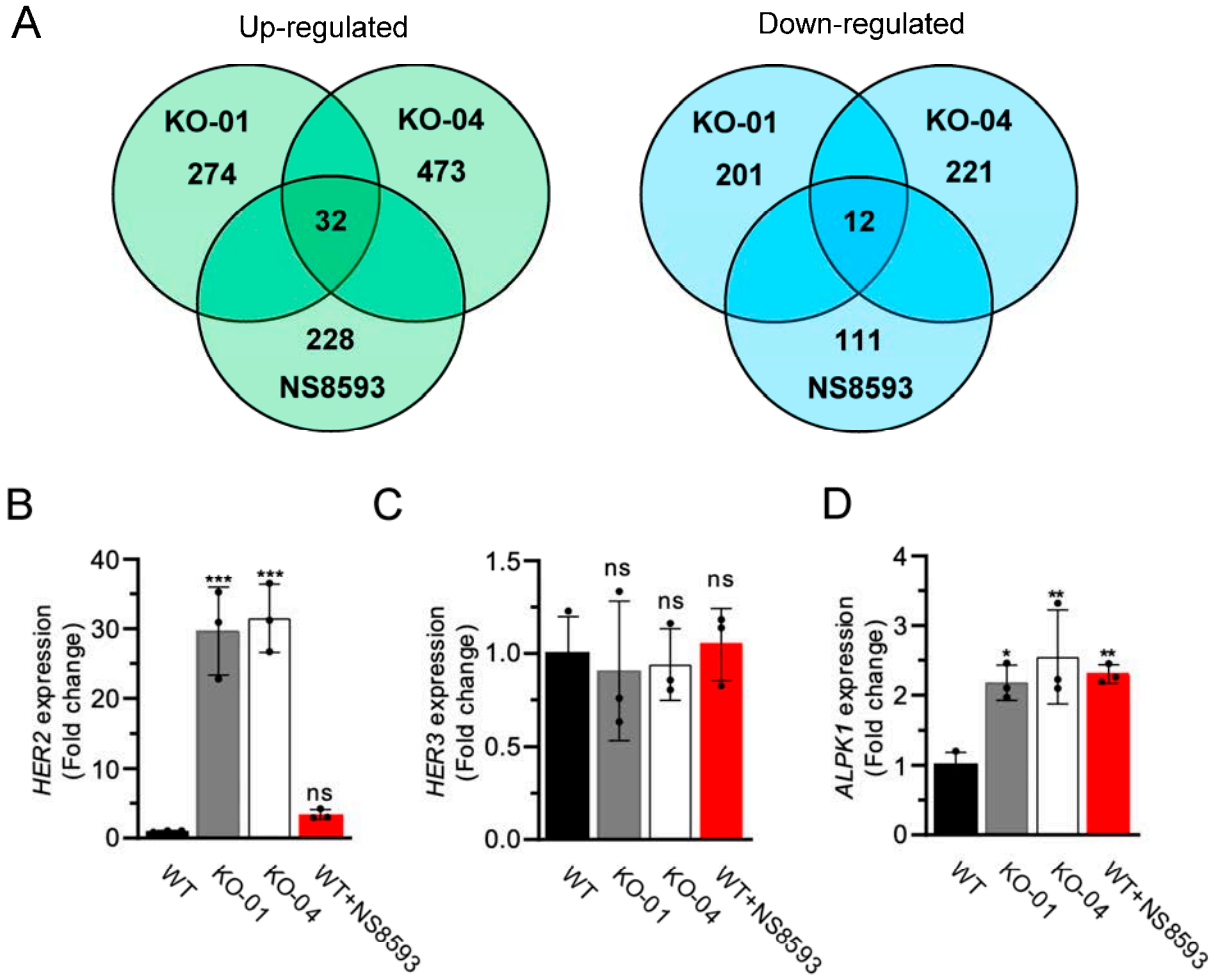

Figure 2. Genome-wide transcriptome profiling of HAP1 cells. (**A**) Venn diagrams for transcripts showing ≥1.5-fold up-regulation (Left panel) and down-regulation (Right panel) in *TRPM7* KO-01 (KO-01), *TRPM7* KO-04 (KO-04), and NS8593-treated WT (NS8593) HAP1 cells as compared to untreated WT HAP1 cells. (**B**–**D**) Relative expression levels of *HER2 (ERBB2)* (**B**) and *HER3 (ERBB3)* (**C**) and *ALPK1* (**D**), assessed by qRT-PCR approach in WT (WT), *TRPM7* KO-01 (KO-01), *TRPM7* KO-04 (KO-04), and NS8593-treated WT (WT+NS8593) HAP1 cells with *HPRT* as a reference transcript. Data are mean ± SD of $n = 3$ independent experiments. *** $p \leq 0.001$; ** $p \leq 0.01$; * $p \leq 0.05$; ns—not significantly different (one-way ANOVA).

Next, we investigated how inhibition of the TRPM7 channel by NS8593 could impact the transcriptome of WT HAP1 cells and whether these changes can be correlated to the effects of *TRPM7* KO mutations. To this end, we cultured WT HAP1 cells for 24 h in the regular cell culture medium containing 30 μM NS8593, followed by transcriptome profiling analogously to the experiment with *TRPM7* KO cells. This analysis identified 228 up- and 111 down-regulated genes in NS8593-treated cells compared to WT HAP1 cells (Figure 2A, Supplementary Table S1). Next, we compared these results with two datasets obtained with *TRPM7* KO cells. We found that pharmacological or genetic ablation of TRPM7 activity in HAP1 cells caused up-regulation of 32 genes and down-regulation of 12 genes (Figure 2A, Supplementary Table S2). Hence, the combinatory profiling of HAP1 cells enabled us to narrow the list of putative regulatory targets of *TRPM7* for future analysis.

We noted that NS8593-treated WT HAP1 cells increased the expression of *HER2* and *ALPK1*, hence recapitulating the impact of *TRPM7* KO mutations (Supplementary Table S2). These findings were re-examined by the qRT-PCR approach, which demonstrated that the expression levels of *HER2*, but not *HER3*, were significantly higher in the two *TRPM7* KO

cell lines (Figure 2B,C). The exposure of WT HAP1 cells to NS8593 also increased *HER2* expression, but these changes were not statistically significant in these settings (Figure 2B). *ALPK1* expression was similarly up-regulated in NS8593-treated WT and *TRPM7* KO cells (Figure 2D).

3.3. *TRPM7* Regulates Expression Levels of HER2 in a Zn^{2+}-Dependent Fashion

The crucial role of HER2 in the diagnosis and treatment of breast cancer [61] prompted us to study how TRPM7 regulates the expression of *HER2*. Using the western blotting approach, we found that HER2 protein levels were 5.0- and 2.5-fold higher in TRPM7 KO-01 and KO-04 cells than in parental WT HAP1 cells (Figure 3A). Since the *TRPM7* KO-04 HAP1 cells were extensively studied previously [12,35,39,62], we selected this cell line for further experiments.

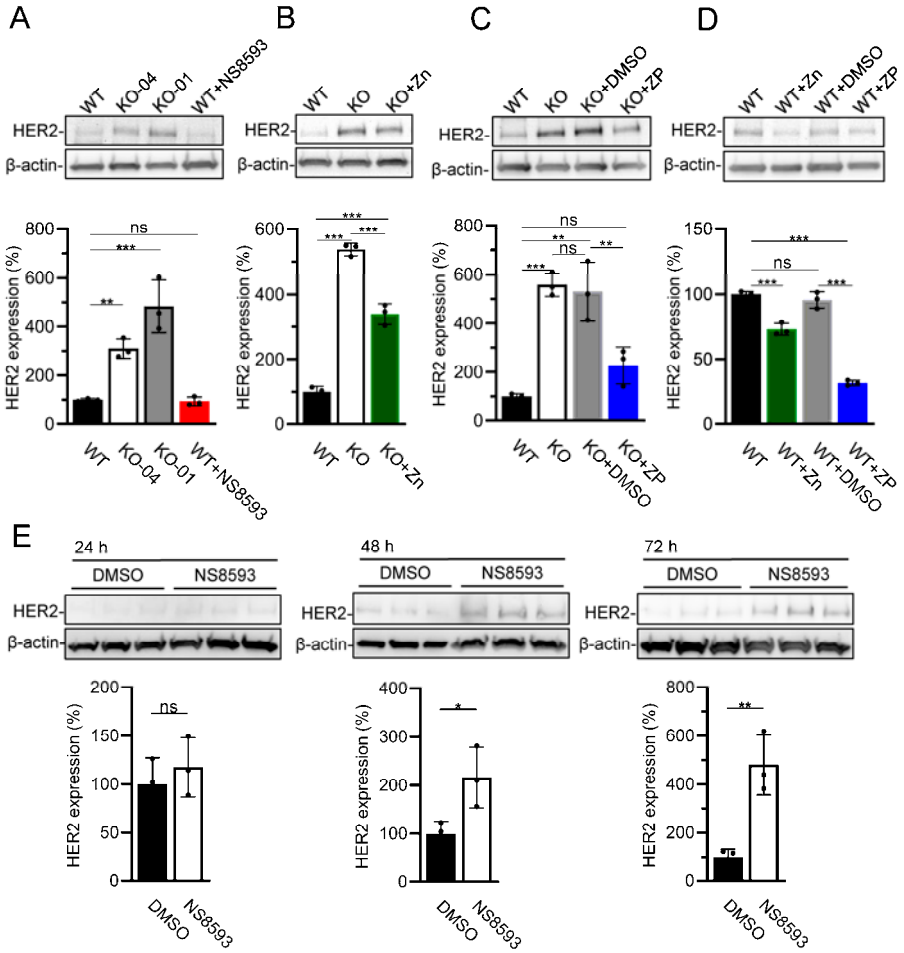

Figure 3. The impact of TRPM7 on HER2 expression levels in HAP1 cells. (**A**) HER2 expression in WT (WT), *TRPM7* KO-04 (KO-04), *TRPM7* KO-01 (KO-01), and NS8593-treated WT (WT+NS8593) HAP1 cells. (**B**–**D**) Effects of 10 μM $ZnCl_2$ (Zn) and 0.5 μM zinc pyrithione (ZP) on HER2 expression in WT (WT) and *TRPM7* KO-04 (KO) HAP1 cells. (**E**) HER2 expression in WT HAP cells treated by 20 μM NS8593 for 24, 48, and 72 h. In (**C**–**E**), equal DMSO volumes (DMSO) were used instead of ZP or NS8593. Upper panels: Representative western blots are shown. Equal volumes of cell lysates were assessed using anti-HER2 and anti-β-actin antibodies. Lower panels: Bar graphs showing normalized HER2 expression levels in experiments from the Upper panel. The ratio of HER2 and anti-β-actin signals in untreated WT HAP1 cells was accounted as 100%. The results shown in the bar graphs are mean ± SD of $n = 3$ independent experiments. In (**A**–**D**), *** $p \leq 0.001$; ** $p \leq 0.01$; ns—not significantly different (one-way ANOVA). In (**E**), ** $p \leq 0.01$; * $p \leq 0.05$; ns—not significantly different (*t*-test).

The TRPM7 channel is highly permeable for divalent cations, including Zn^{2+}, and its genetic deletion leads to the cellular deprivation of Zn^{2+} in *TRPM7* KO-04 HAP1 cells [12]. However, Zn^{2+} levels were normalized in *TRPM7* KO-04 HAP1 cells after Zn^{2+} supplementation, arguing that alternative Zn^{2+} transporters can compensate for the lack of TRPM7 [12]. In accordance with this assumption, we showed previously that the uptake of radioactive $^{65}Zn^{2+}$ was significantly reduced but not completely abolished in *TRPM7* KO-04 HAP1 cells [12]. Along these lines, we investigated herein whether adding Zn^{2+} to the cell culture medium can reverse the effect of *TRPM7* KO-04 cells on the expression of HER2. We observed that adding 10 µM Zn^{2+} to the regular medium could ameliorate the impact of *TRPM7* KO on HER2 expression (Figure 3B). The expression of HER2 was further normalized in *TRPM7* KO-04 cells after the application of 0.5 µM zinc pyrithione (ZP), a broadly used Zn^{2+} ionophore (Figure 3C). In agreement with these findings, analogous treatment of WT HAP1 cells by additional Zn^{2+} or ZP caused a significant reduction of HER2 expression (Figure 3D). These results support the notion that deletion of *TRPM7* indirectly altered HER2 expression, likely due to Zn^{2+} deprivation of HAP1 cells.

We noted that HER2 expression was not altered in WT HAP1 cells cultured for 24 h in the presence of NS8593 (Figure 3A). We asked whether a more prolonged inhibition of the TRPM7 channel is necessary to replicate the impact of *TRPM7* KO mutations on HER2 expression. To this end, we exposed WT HAP1 cells to NS8593 for 48–72 h and found that the prolonged application of the TRPM7 inhibitor caused a gradual increase in HER2 levels (Figure 3E).

The haploid HAP1 cells were engineered from cells isolated from a patient with chronic myeloid leukemia [63]. To investigate whether HER2 is the regulatory target of TRPM7 in cells of non-hematopoietic origin, we examined HER2 expression in embryonic trophoblast stem (TS) cells isolated from WT and *Trpm7* KO mice [28,39]. Unexpectedly, we found that *Trpm7* KO TS cells displayed significantly reduced HER2 expression levels compared to WT TS cells. This effect was partially reversed by adding Zn^{2+} or ZP to the cell culture medium (Figure 4A). Furthermore, the exposure of WT TS cells to the medium supplemented by Zn^{2+} or ZP increased the expression of HER2 (Figure 4B).

HEK293 cells were often used to study the cellular role of endogenous TRPM7 [15,24,28,64]. We found that, analogously to TS cells, HEK293 cells with *TRPM7* KO mutation [15] displayed reduced levels of HER2 compared to WT cells and that Zn^{2+} supplementation ameliorated this phenotype (Figure 4C). Consistently, the exposure of WT HEK293 cells to the Zn^{2+}-enriched medium resulted in up-regulation of HER2 expression (Figure 4E). However, we noted that the application of ZP did not normalize HER2 levels in WT and *TRPM7* KO HEK293 cells (Figure 4D,E). Next, we asked whether siRNA silencing of TRPM7 could alter HER2 expression analogously to the *TRPM7* KO mutation. Applying two alternative TRPM7-specific siRNA constructs, we observed that both treatments lowered HER2 levels in HEK293 cells and that this effect was comparable to the impact of *TRPM7* KO mutation (Figure 4F).

In addition, we studied the impact of *TRPM7* KO on human HeLa cells, which were derived from cervical cancer [65]. Using the patch-clamp approach, we found that WT HeLa cells display characteristic TRPM7 currents, which were fully diminished in *TRPM7* KO cells (Supplementary Figure S2A). Analogously to our experiments with TS and HEK293 cells, *TRPM7* KO caused down-regulation of HER2 expression in HeLa cells (Supplementary Figure S2B). However, we observed that Zn^{2+} supplementation of *TRPM7* KO HeLa cells did not normalize HER2 levels, likely reflecting the inability of alternative Zn^{2+} transporter proteins to compensate for the role of TRPM7 in these cells (Supplementary Figure S2B). In line with this notion, adding Zn^{2+} to the culture medium of WT HeLa cells caused only modest up-regulation of HER2 expression, but these changes were not statistically significant (Supplementary Figure S2C).

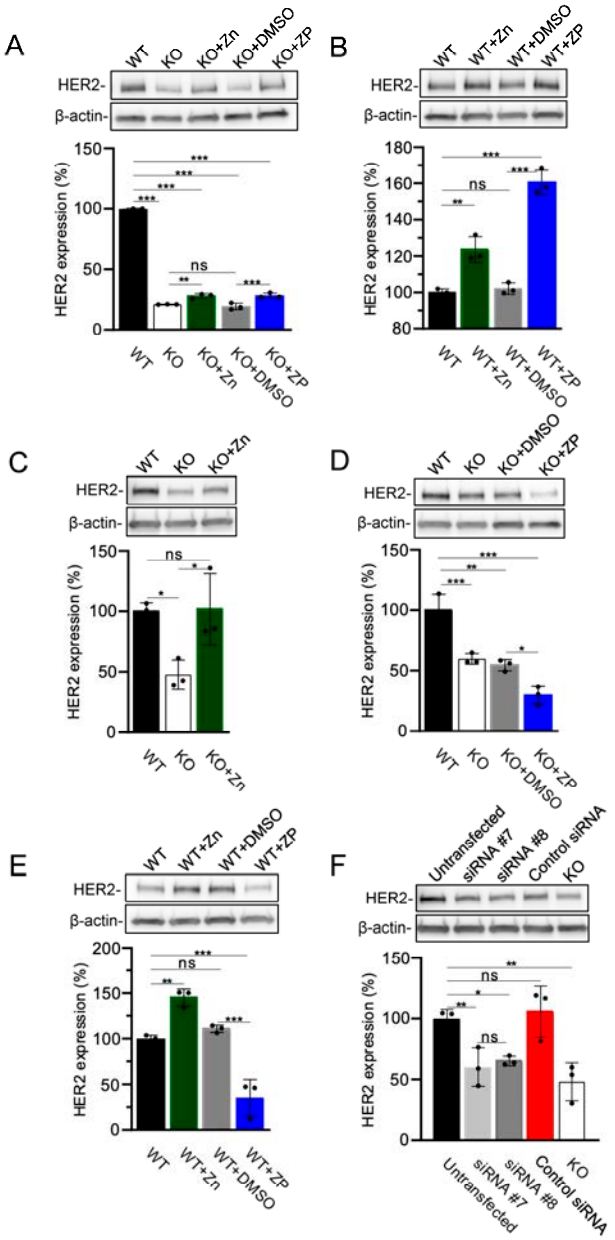

Figure 4. The regulatory effect of TRPM7 on HER2 expression in embryonic trophoblast stem (TS) cells and HEK293 cells. (**A**,**B**) Assessment of HER2 expression in WT (WT) and *TRPM7* KO (KO) TS cells. Upper panels: Representative western blots obtained with the cells cultured in the absence or presence of 10 μM $ZnCl_2$ (Zn) and 0.5 μM zinc pyrithione (ZP) are shown. Equal volumes of cell lysates were assessed using anti-HER2 and anti-β-actin antibodies. Equal volumes of DMSO (DMSO) were used instead of ZP as an additional control. Lower panels: Bar graphs showing normalized HER2 expression levels in experiments in the Upper panels. The ratio of HER2 to anti-β-actin signals in WT TS cells was accounted as 100%. (**C**–**E**) Assessment of HER2 expression in WT (WT) and *TRPM7* KO (KO) HEK293 cells in the absence or presence of 10 μM $ZnCl_2$ (Zn) and 0.5 μM zinc pyrithione (ZP). The experiments were performed and analyzed analogously to (**A**,**B**). (**F**) Analysis of HER2 expression in untransfected WT (Untransfected) HEK293 cells, WT HEK293 cells transfected by *TRPM7*-specific siRNA #7 (siRNA #7), *TRPM7*-specific siRNA #8 (siRNA #*8*) and AllStars Negative Control siRNA (Control siRNA), and *TRPM7* KO (KO) HEK293 cells. Experiments were performed and analyzed analogously to (**A**,**B**) except that the ratio of HER2 to anti-β-actin signal in untransfected WT HEK293 cells was accounted as 100%. The results in the bar graphs are mean ± SD of $n = 3$ independent experiments. *** $p \leq 0.001$; ** $p \leq 0.01$; * $p \leq 0.05$; ns—not significantly different (one-way ANOVA).

Human breast cancer SKBR3 cells expressing very high levels of HER2 are frequently used for testing new therapeutic strategies. Using western blotting, we could confirm that SKBR3 cells express remarkably high HER2 levels compared to other breast cancer MCF-7 and MDA-MB-231 cells (Figure 5A). Next, we investigated whether HER2 is the regulatory target of TRPM7 in SKBR3 cells. Analogously to other cells (Figure 4, Supplementary Figure S2), we observed that two alternative anti-*TRPM7* siRNAs caused significant down-regulation of HER2 levels in SKBR3 cells (Figure 5B). In addition, we performed patch-clamp measurements of endogenous TRPM7 currents in SKBR3 and MDA-MB-231 (Figure 5C). We found that both cell lines displayed similar current amplitudes, suggesting that increased expression of HER2 did not affect the TRPM7 channel activity (Figure 5C).

Taken together, our experiments with various cell lines revealed that TRPM7 regulates the expression levels of HER2 protein in a Zn^{2+}-dependent fashion.

3.4. Combinatory Pharmacological Inhibition of TRPM7 and HER2 Elicits the Synergistic Effect on the Proliferation of HER2-Positive Breast Cancer Cells

It is well-documented that genetic or pharmacological inactivation of TRPM7 causes an inhibitory effect on the growth of tumor cells (reviewed in [25]). In accordance with this notion, we observed that NS8593 suppressed the proliferation of SKBR3 and MDA-MB-231 cells in a concentration-dependent fashion (Figure 5D). Moreover, the treatment of SKBR3 cells by NS8593 significantly reduced HER2 levels (Figure 5E).

Consequently, we asked whether a combined pharmacological inhibition of TRPM7 and HER2 could improve the treatment of HER2-positive cancer cells. We exposed SKBR3 cells to the potent HER2 inhibitor CP724714 [66] and found that this compound dose-dependently suppressed the growth of SKBR3 cells (Figure 6A). Co-administration of 10 or 20 μM NS8593 with CP724714 further suppressed the proliferation of SKBR3 cells (Figure 6B,C). Applying a LOEWE analysis [60,67], we established that a combinatory treatment with 10 μM NS8593 and 0.5 μM CP724714 synergistically affected cell growth (Figure 6D). Furthermore, adding 20 μM NS8593 elicited the synergetic effect in the presence of the whole range of CP724714 concentrations (Figure 6D). To rule out that the synergetic effect of CP724714 was elicited due to off-target inhibition of TRPM7, we examined transiently expressed TRPM7 in WT HEK293 cells and examined TRPM7 activity in the presence of either 10 μM CP724714 or 10 μM NS8593. We observed that NS8593 inhibited the channel, whereas CP724714 showed no effects on TRPM7 (Supplementary Figure S3).

Finally, we conducted analogous experiments with MDA-MB-231 cells expressing HER2 at a low level (Supplementary Figure S4A–C). MDA-MB-231 cells were insensitive to the relevant concentrations of CP724714. Moreover, CP724714 could not enhance the antiproliferative effects of 5 and 20 μM NS8593 and rather weakened the impact of 10 μM NS8593 (Supplementary Figure S4D). These results support the idea that the synergistic action of NS8593 and CP724714 on SKBR3 cells was attributed to the high expression of HER2.

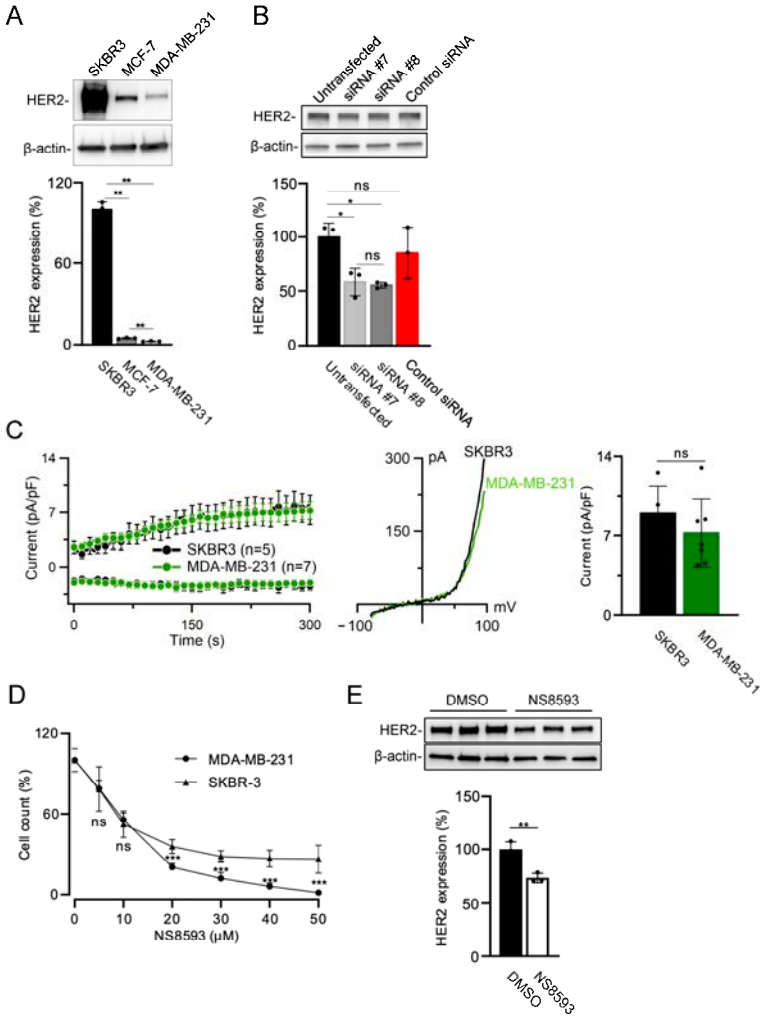

Figure 5. Assessment of breast cancer SKBR3, MCF-7, and MDA-MB-231 cells. (**A**) Analysis of HER2 expression in SKBR3, MCF-7, and MDA-MB-231 cells. Upper panel: Representative western blot obtained with SKBR3, MCF-7, and MDA-MB-231 cells. Equal volumes of cell lysates were assessed using anti-HER2 and anti-β-actin antibodies. Lower panel: Bar graph showing normalized HER2 expression levels in experiments from the Upper panel. The ratio of HER2 to anti-β-actin signal in SKBR3 cells was accounted as 100%. (**B**) Assessment of HER2 expression in untransfected (Untransfected) SKBR3 cells and SKBR3 cells transfected by *TRPM7*-specific siRNA #7 (siRNA #7), siRNA #8 (siRNA #8), and AllStars Negative Control siRNA (Control siRNA). Experiments were performed and analyzed analogously to (**A**) except that the ratio of HER2 to anti-β-actin signal in untransfected SKBR3 cells was accounted as 100%. The results in the bar graphs in (**A**,**B**) are mean ± SD of $n = 3$ independent experiments. ** $p \leq 0.01$; * $p \leq 0.05$; ns—not significantly different (one-way ANOVA). (**C**) Comparison of endogenous TRPM7 currents measured in SKBR3 and MDA-MB-231 cells. Left panel: Whole-cell currents measured at −80 and +80 mV over time in SKBR3 and MDA-MB-231 cells. Middle panel: Representative current−voltage (I−V) relationships obtained at 300 s in measurements shown in the Left panel. Right panel: Bar graph of current amplitudes at +80 mV (300 s) illustrated on the Left panel. Data are mean ± SD; *n*, the number of cells examined. Ns—not significantly different (*t*-test). (**D**) Viability of SKBR3 and MDA-MB-231 cells exposed to different concentrations of NS8593 for 72 h. Cell densities in the absence of NS8593 were accounted as 100%. Data are mean ± SD of $n = 3$ independent experiments. *** $p \leq 0.001$; ns—not significantly different (*t*-test). (**E**) HER2 expression in SKBR3 cells treated by 30 μM NS8593 (NS8593) or equal volumes of DMSO (DMSO) for 72 h. Upper panel: Representative western blots are shown. Equal volumes of cell lysates were assessed using anti-HER2 and anti-β-actin antibodies. Lower panel: Bar graphs showing normalized HER2 expression level in experiments from the Upper panel. The results in the bar graphs are mean ± SD of $n = 3$ independent experiments. ** $p \leq 0.01$ (*t*-test).

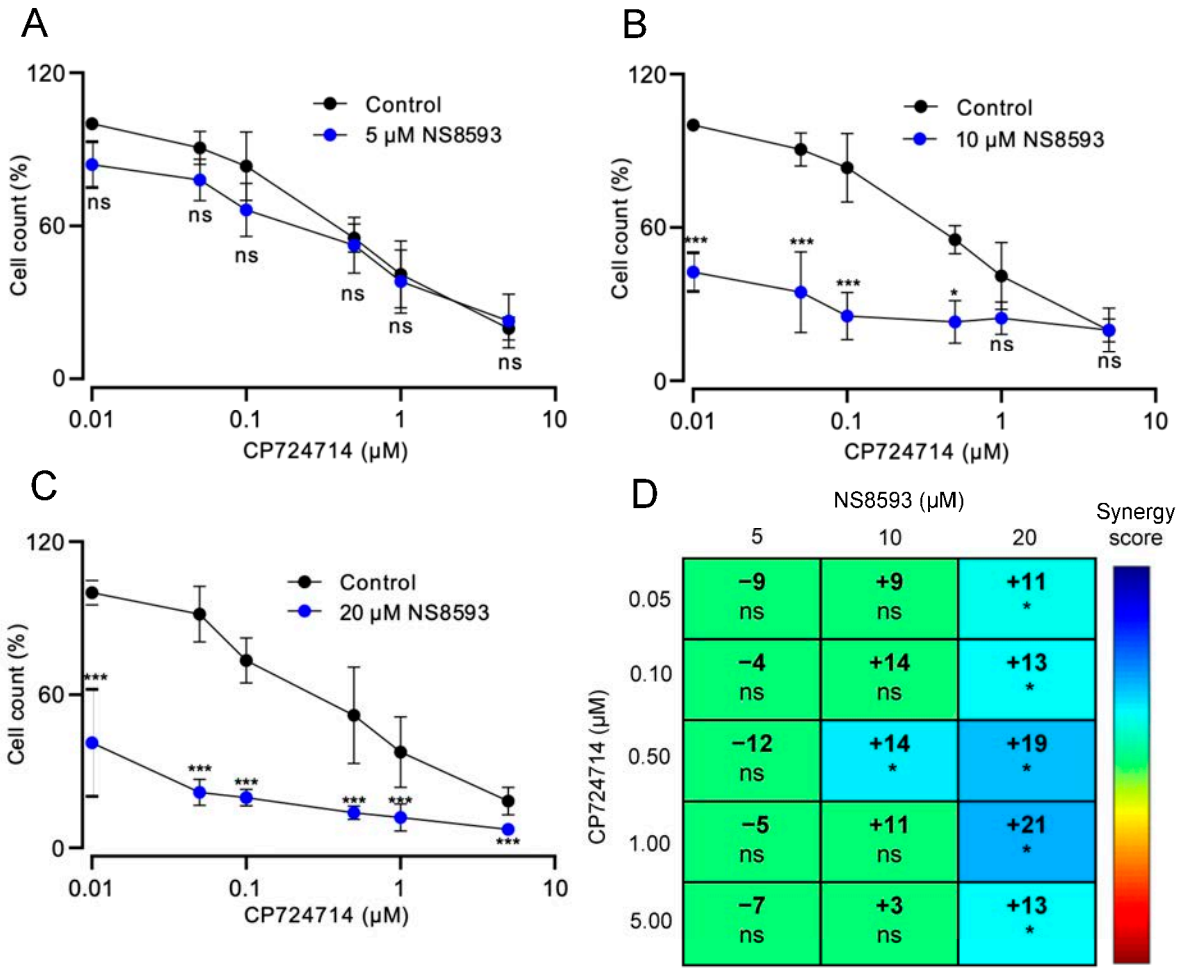

Figure 6. Combinatory treatment of SKBR3 cells by NS8593 and CP724714. (**A**–**C**) Viability of SKBR3 cells treated by different concentrations of CP724714 for 72 h in the absence (Control) and presence of 5 µM (**A**), 10 µM (**B**), or 20 µM (**C**) NS8593. Data are mean ± SD of $n = 3$ independent experiments. *** $p \leq 0.001$; * $p \leq 0.05$; ns—not significantly different (one-way ANOVA). (**D**) LOEWE synergy analysis of the cytotoxic effects elicited by NS8593 and CP724714 on SKBR3 cells in (**A**–**C**). * $p \leq 0.05$; ns—not significantly different (one-way ANOVA).

4. Discussion

In the present study, we conducted transcriptome profiling of human leukemia HAP1 cells to get insights on cellular responses triggered by inhibition of the TRPM7 channel using the pharmacological agent NS8593. Among other entities, expression levels of HER2 (ERBB2) were found to be affected by either NS8593 or genetic disruption of *TRPM7* in HAP1 cells and other cell lines. Given the exceptional importance of HER2 for treating breast cancer, we performed proof-of-principle experiments to show that combined pharmacological inhibition of HER2 and TRPM7 elicits synergistic antiproliferative effects on HER2-positive breast cancer cells.

HAP1 cells represent a near-haploid cell line engineered from cells isolated from a patient with chronic myeloid leukemia triggered by the *BCR-ABL* fusion mutation [63]. As HAP1 cells only have one copy of each gene, the CRISPR/Cas9 technology allows a rapid introduction of loss-of-function mutations in these cells [63]. Consequently, HAP1 cells were widely used in various biomedical studies, including functional profiling of oncogenic mutations and genome-wide screens for new anti-cancer targets [68–71]. More recently, our group and other laboratories explored HAP1 cells to elucidate the cellular role of TRPM7 [12,35,39,62,72]. Thus, we examined the HAP1 cell line carrying a loss-of-function mutation in the *TRPM7* gene to demonstrate that the TRPM7 channel regulates cellular

levels of Zn^{2+} [12,39]. In the present study, we investigated the impacts of the *TRPM7* KO mutation and TRPM7 inhibitor NS8593 on the transcriptome of HAP1 cells. Such comparative analysis revealed that TRPM7 regulates HER2 expression in a Zn^{2+}-dependent manner [12,15].

The clinical relevance of HER2 for targeting breast cancer therapy is well-documented [61]. Up to 30% of breast cancers overexpress HER2, whereby high HER2 expression is associated with a more aggressive disease progression and higher recurrence rate [61]. Many patients with HER2-overexpressing cancer respond to HER2 inhibitors such as trastuzumab, pertuzumab, lapatinib, and neratinib [73]. However, patients frequently develop drug resistance through different mechanisms, for instance, acquiring mutations in HER2 or compensatory changes in cell signaling [73,74]. To this end, the identification of new pathways connected to HER2 can offer alternative strategies for combinatorial drug treatment of breast cancer [73].

The present study investigated the TRPM7/HER2 relationship in various cells, including embryonic TS cells, HEK293, HeLa, MDA-MB-231, and SKBR3 cells. These experiments demonstrated that TRPM7 regulates the expression of HER2. However, unlike in HAP1 cells, the deactivation of TRPM7 in TS cells, HEK293, HeLa, MDA-MB-231, and SKBR3 cells resulted in the down-regulation of HER2. We noted that another group investigated the impact of *Trpm7* KO on the transcriptome of mouse embryonic stem (ES) cells and reported that *HER2* was down-regulated in *Trpm7* KO ES cells [16]. Previously, we performed genome-wide transcriptome profiling of villi isolated from the whole intestine of mice with enterocyte-specific *Trpm7* KO [12]. Intriguingly, *HER2* was down-regulated in *Trpm7*-deficient villi [12]. The distinct response of HAP1 cells may be attributed to the hematopoietic origin of these cells associated with distinct Zn^{2+} signaling and expression profiles of Zn^{2+} finger proteins [75]. In addition, a compensatory impact of Zn^{2+} transporters on the *TRPM7* KO phenotype could play a role. Apart from TRPM7, twenty-four members of the solute carriers of family 30 (Slc30a1–10 or ZnT1–10) and family 39 (Slc39a1–14 or Zip1–14) were proposed to orchestrate cellular Zn^{2+} balance in a cell-specific mode [76]. It is worth noting that analysis of human breast cancer tissues showed significant Zn^{2+} accumulation, especially in HER2-positive and triple-negative cancers and that this effect correlated with the grade of malignancy [77,78]. In another study, experiments with MCF-7 breast cancer cells demonstrated that TRPM7 regulates cellular levels of MDMX by modulating the intracellular Zn^{2+} levels [79]. MDMX is a zinc-containing negative regulator of p53, which is overexpressed in various cancers and implicated in cancer initiation and progression [79]. Along these lines, further studies are necessary to establish the mechanisms of the Zn^{2+}-dependent transcriptional regulation of HER2.

NS8593 was initially characterized as an inhibitor of Ca^{2+}-activated K^+ ($K_{Ca}2.1$–2.3) channels [80]. Further research revealed that NS8593 is also a potent inhibitor of the TRPM7 channel [81]. In non-excitable cells, $K_{Ca}2.1$–2.3 channels hyperpolarize the plasma membrane, thereby enhancing the influx of divalent cations [80]. On the other hand, the TRPM7 channel controls the cellular uptake of Zn^{2+}, Ca^{2+}, and Mg^{2+} [2,12]. Therefore, the dual specificity of NS8593 could be advantageous for treating rapidly growing cancer cells, which heavily rely on a steady supply of divalent cations and other nutrients [10,20,35,37–41]. In the present work, we investigated whether NS8593 can be advantageous for the combined targeting of HER2-positive cancer cells. Our proof-of-concept experiments showed that the co-application of pharmacological inhibitors of HER2 and TRPM7 had a synergistic antiproliferative effect on HER2-positive breast cancer SKBR3 cells but not HER2-deficient MDA-MB-231 cells. Collectively, our results reinforced the idea that TRPM7 represents a promising therapeutic target for treating breast cancer [38,46–51].

5. Conclusions

Transcriptome profiling of human leukemia HAP1 cells revealed that TRPM7 plays a regulatory role in the expression of several transcripts, including *HER2* (*ERBB2*). Further

examination of HAP1 cells and several non-hematopoietic cells demonstrated that TRPM7 affects the expression of *HER2* in a Zn^{2+}-dependent fashion. Co-inhibition of HER2 and TRPM7 elicits a synergistic antiproliferative effect on HER2-overexpressing SKBR3 cells. Collectively, our findings suggest a new combinatorial approach for a targeted therapy for HER2-positive breast cancer.

Supplementary Materials: The following supporting information can be downloaded at: https://www.mdpi.com/article/10.3390/cells13211801/s1, Figure S1. Characterization of *TRPM7* KO-01 HAP1 cells. (**A**) Sequence alignment of RT-PCR product obtained with primers flanking exon 4 of the human *TRPM7* gene. RT-PCR was performed using RNA extracted from *TRPM7* KO-01 HAP1 cells. Note that the aberrant transcript contains an intronic sequence (indicated by the red arrow), which was spliced between sequences encoded by exon 3 and the distal part of exon 4 of *TRPM7*. (**B**) Magnified sequence alignment of the intronic sequence found in the aberrant *TRPM7* transcript. (**C**) The sequence of RT-PCR product of the mutant *TRPM7* transcript containing the exon 3 (black sequence), intronic sequence (red sequence) and distal segment of exon 4 (blue sequence). In silico translation of the mutant transcript revealed that the mutation results in a frame-shift mutation. Figure S2. Assessment of human HeLa cells. (**A**) Left panel: Whole-cell currents measured at −80 and +80 mV over time in wild-type (WT) and *TRPM7* KO (KO) HeLa cells. Middle panel: Representative current−voltage (I−V) relationships obtained at 300 s in measurements illustrated on the Left panel. Right panel: Bar graph of current amplitudes at +80 mV (300 s) illustrated on the Left panel. Data are mean ± SD; *n*, the number of cells examined. * $p \leq 0.05$; (one-way ANOVA). (**B**,**C**) Upper panels: Representative western blots obtained with WT (WT) and *TRPM7* KO (KO) HeLa cells maintained in the absence or presence of 10 μM $ZnCl_2$ (Zn). Equal volumes of cell lysates were assessed using anti-HER2 and anti-β-actin antibodies. Lower panels: Bar graphs showing normalized HER2 expression levels in experiments from the Upper panels. The ratio of HER2 to anti-β-actin signals in WT cells (**B**) or untreated WT cells (**C**) was accounted as 100%. Data are mean ± SD of $n = 3$ independent experiments. ** $p \leq 0.01$; ns—not significantly different (one-way ANOVA). Figure S3. The effects of CP724714 and NS8593 on the TRPM7 channel. Intracellular Ca^{2+} levels ($[Ca^{2+}]_i$) were measured using a bioluminescence-based assay in WT HEK293 cells transfected with *Trpm7* plasmid DNA exposed to 10 μM CP724714, 10 μM NS8593 or equal DMSO volumes (DMSO). (**A**) $[Ca^{2+}]_i$ was measured in the presence of 0.5 or 10 mM external Ca^{2+} ($[Ca^{2+}]_o$) as indicated by the horizontal bars. Representative traces are shown from $n = 3$ independent experiments. (**B**) Ca^{2+} rises ($\Delta[Ca^{2+}]_i$, mean ± SD, $n = 3$) were calculated from measurements shown in **(A)** by subtraction of the resting $[Ca^{2+}]_i$ from the maximal $[Ca^{2+}]_i$ after application of 10 mM $[Ca^{2+}]_o$. *** $p \leq 0.001$; ns—not significantly different (one-way ANOVA). Figure S4. Combinatory treatment of MDA-MB-231 cells by NS8593 and CP724714. (**A–C**) Viability of MDA-MB-231 cells treated by different concentrations of CP724714 for 72 h in the absence (Control) and presence of 5 μM (**A**), 10 μM (**B**), or 20 μM (**C**) NS8593. Data are mean ± SD of $n = 3$ independent experiments. *** $p \leq 0.001$; ** $p \leq 0.01$; * $p \leq 0.05$; ns—not significantly different (one-way ANOVA). **D**, LOEWE synergy analysis of the cytotoxic effects elicited by NS8593 and CP724714 on MDA-MB-231 cells in (**A–C**). * $p \leq 0.05$; ns—not significantly different (one-way ANOVA). Table S1. Microarray profiling of differentially expressed genes after inactivation of TRPM7 in HAP1 cells. Excel file contains one worksheet: Genome-wide analysis of Affymetrix probes using RNA extracted from parental wild-type (WT) cells, *TRPM7* KO cells (clones KO-01 and KO-04) and parental WT cells treated with NS8593 (WT+NS8593). Table S2. Commonly up- and down-regulated transcripts after genetic and pharmacological inactivation of TRPM7 in HAP1 cells. Excel file contains two worksheets: (**1**) Commonly ≥ 1.5-fold up-regulated Affymetrix probes in RNA extracted from *TRPM7* KO cells (clones KO-01 and KO-04) and parental wild-type (WT) cells treated with NS8593 (WT+NS8593) as compared to untreated parental WT cells; (**2**) Commonly ≥ 1.5-fold down-regulated Affymetrix probes in RNA extracted from *TRPM7* KO cells (clones KO-01 and KO-04) and parental WT cells treated with NS8593 (WT+NS8593) as compared to parental untreated WT cells. Table S3. Primers used for qRT-PCR assessment of HAP1 cells.

Author Contributions: M.E., E.S. and C.G. carried out experiments and analyzed data. M.E., T.G. and V.C. wrote the manuscript, which was then edited by all the authors. All authors have read and agreed to the published version of the manuscript.

Funding: Vladimir Chubanov and Thomas Gudermann were supported by the Deutsche Forschungsgemeinschaft (DFG), TRR 152 (P15) and Research Training Group 2338 (P10).

Institutional Review Board Statement: This study did not require ethical approval.

Informed Consent Statement: Not applicable.

Data Availability Statement: NCBI GEO–GSE203013, Whole-genome profiling of human HAP1 cells after the genetic and pharmacological inactivation of TRPM7.

Acknowledgments: We thank Joanna Zaisserer and Anna Erbacher for their excellent technical assistance. We thank David Clapham for *TRPM7* KO HEK293 cells.

Conflicts of Interest: The authors declare no conflicts of interest.

References

1. Gotru, S.K.; Chen, W.; Kraft, P.; Becker, I.C.; Wolf, K.; Stritt, S.; Zierler, S.; Hermanns, H.M.; Rao, D.; Perraud, A.-L.; et al. TRPM7 Kinase Controls Calcium Responses in Arterial Thrombosis and Stroke in Mice. *Arter. Thromb. Vasc. Biol.* **2018**, *38*, 344–352. [CrossRef] [PubMed]
2. Fleig, A.; Chubanov, V. *Handbook of Experimental Pharmacology*; Springer: Berlin/Heidelberg, Germany, 2014; pp. 521–546.
3. Bates-Withers, C.; Sah, R.; Clapham, D.E. TRPM7, the Mg^{2+} inhibited channel and kinase. *Adv. Exp. Med. Biol.* **2011**, *704*, 173–183.
4. Nadezhdin, K.D.; Correia, L.; Narangoda, C.; Patel, D.S.; Neuberger, A.; Gudermann, T.; Kurnikova, M.G.; Chubanov, V.; Sobolevsky, A.I. Structural mechanisms of TRPM7 activation and inhibition. *Nat. Commun.* **2023**, *14*, 2639. [CrossRef]
5. Nadler, M.J.S.; Hermosura, M.C.; Inabe, K.; Perraud, A.-L.; Zhu, Q.; Stokes, A.J.; Kurosaki, T.; Kinet, J.-P.; Penner, R.; Scharenberg, A.M.; et al. LTRPC7 is a Mg.ATP-regulated divalent cation channel required for cell viability. *Nature* **2001**, *411*, 590–595. [CrossRef]
6. Monteilh-Zoller, M.K.; Hermosura, M.C.; Nadler, M.J.; Scharenberg, A.M.; Penner, R.; Fleig, A. TRPM7 provides an ion channel mechanism for cellular entry of trace metal ions. *J. Gen. Physiol.* **2003**, *121*, 49–60. [CrossRef]
7. Runnels, L.W.; Yue, L.; Clapham, D.E. TRP-PLIK, a bifunctional protein with kinase and ion channel activities. *Science* **2001**, *291*, 1043–1047. [CrossRef] [PubMed]
8. Bai, Z.; Feng, J.; Franken, G.A.C.; Al'saadi, N.; Cai, N.; Yu, A.S.; Lou, L.; Komiya, Y.; Hoenderop, J.G.J.; de Baaij, J.H.F.; et al. CNNM proteins selectively bind to the TRPM7 channel to stimulate divalent cation entry into cells. *PLoS Biol.* **2021**, *19*, e3001496. [CrossRef]
9. Li, M.; Du, J.; Jiang, J.; Ratzan, W.; Su, L.-T.; Runnels, L.W.; Yue, L. Molecular determinants of Mg^{2+} and Ca^{2+} permeability and pH sensitivity in TRPM6 and TRPM7. *J. Biol. Chem.* **2007**, *282*, 25817–25830. [CrossRef]
10. Schmitz, C.; Perraud, A.-L.; Johnson, C.O.; Inabe, K.; Smith, M.K.; Penner, R.; Kurosaki, T.; Fleig, A.; Scharenberg, A.M. Regulation of vertebrate cellular Mg^{2+} homeostasis by TRPM7. *Cell* **2003**, *114*, 191–200. [CrossRef]
11. Ryazanova, L.V.; Rondon, L.J.; Zierler, S.; Hu, Z.; Galli, J.; Yamaguchi, T.P.; Mazur, A.; Fleig, A.; Ryazanov, A.G. TRPM7 is essential for Mg^{2+} homeostasis in mammals. *Nat. Commun.* **2010**, *1*, 109. [CrossRef]
12. Mittermeier, L.; Demirkhanyan, L.; Stadlbauer, B.; Breit, A.; Recordati, C.; Hilgendorff, A.; Matsushita, M.; Braun, A.; Simmons, D.G.; Zakharian, E.; et al. TRPM7 is the central gatekeeper of intestinal mineral absorption essential for postnatal survival. *Proc. Natl. Acad. Sci. USA* **2019**, *116*, 4706–4715. [CrossRef] [PubMed]
13. Ardestani, G.; Mehregan, A.; Fleig, A.; Horgen, F.D.; Carvacho, I.; Fissore, R.A. Divalent cation influx and calcium homeostasis in germinal vesicle mouse oocytes. *Cell Calcium* **2020**, *87*, 102181. [CrossRef]
14. Tashiro, M.; Inoue, H.; Konishi, M. Modulation of Mg^{2+} influx and cytoplasmic free Mg^{2+} concentration in rat ventricular myocytes. *J. Physiol. Sci.* **2019**, *69*, 97–102. [CrossRef]
15. Abiria, S.A.; Krapivinsky, G.; Sah, R.; Santa-Cruz, A.G.; Chaudhuri, D.; Zhang, J.; Adstamongkonkul, P.; DeCaen, P.G.; Clapham, D.E. TRPM7 senses oxidative stress to release Zn^{2+} from unique intracellular vesicles. *Proc. Natl. Acad. Sci. USA* **2017**, *114*, E6079–E6088. [CrossRef] [PubMed]
16. Krapivinsky, G.; Krapivinsky, L.; Manasian, Y.; Clapham, D.E. The TRPM7 chanzyme is cleaved to release a chromatin-modifying kinase. *Cell* **2014**, *157*, 1061–1072. [CrossRef] [PubMed]
17. Runnels, L.W.; Yue, L.; Clapham, D.E. The TRPM7 channel is inactivated by PIP(2) hydrolysis. *Nat. Cell. Biol.* **2002**, *4*, 329–336. [CrossRef]
18. Krapivinsky, G.; Mochida, S.; Krapivinsky, L.; Cibulsky, S.M.; Clapham, D.E. The TRPM7 ion channel functions in cholinergic synaptic vesicles and affects transmitter release. *Neuron* **2006**, *52*, 485–496. [CrossRef]
19. Faouzi, M.; Kilch, T.; Horgen, F.D.; Fleig, A.; Penner, R. The TRPM7 channel kinase regulates store-operated calcium entry. *J. Physiol.* **2017**, *595*, 3165–3180. [CrossRef]
20. Luongo, F.; Pietropaolo, G.; Gautier, M.; Dhennin-Duthille, I.; Ouadid-Ahidouch, H.; Wolf, F.I.; Trapani, V. TRPM6 is Essential for Magnesium Uptake and Epithelial Cell Function in the Colon. *Nutrients* **2018**, *10*, 784. [CrossRef]
21. Ryazanov, A.G. Elongation factor-2 kinase and its newly discovered relatives. *FEBS Lett.* **2002**, *514*, 26–29. [CrossRef]
22. Drennan, D.; Ryazanov, A.G. Alpha-kinases: Analysis of the family and comparison with conventional protein kinases. *Prog. Biophys. Mol. Biol.* **2004**, *85*, 1–32. [CrossRef] [PubMed]
23. Ryazanova, L.V.; Dorovkov, M.V.; Ansari, A.; Ryazanov, A.G. Characterization of the protein kinase activity of TRPM7/ChaK1, a protein kinase fused to the transient receptor potential ion channel. *J. Biol. Chem.* **2004**, *279*, 3708–3716. [CrossRef]

24. Ferioli, S.; Zierler, S.; Zaißerer, J.; Schredelseker, J.; Gudermann, T.; Chubanov, V. TRPM6 and TRPM7 differentially contribute to the relief of heteromeric TRPM6/7 channels from inhibition by cytosolic Mg^{2+} and Mg.ATP. *Sci. Rep.* **2017**, *7*, 8806. [CrossRef] [PubMed]
25. Chubanov, V.; Gudermann, T. Mapping TRPM7 Function by NS8593. *Int. J. Mol. Sci.* **2020**, *21*, 7017. [CrossRef] [PubMed]
26. Ryazanova, L.V.; Hu, Z.; Suzuki, S.; Chubanov, V.; Fleig, A.; Ryazanov, A.G. Elucidating the role of the TRPM7 alpha-kinase: TRPM7 kinase inactivation leads to magnesium deprivation resistance phenotype in mice. *Sci. Rep.* **2014**, *4*, 7599. [CrossRef]
27. Hofmann, T.; Schäfer, S.; Linseisen, M.; Sytik, L.; Gudermann, T.; Chubanov, V. Activation of TRPM7 channels by small molecules under physiological conditions. *Pflugers Arch.* **2014**, *466*, 2177–2189. [CrossRef]
28. Rössig, A.; Hill, K.; Nörenberg, W.; Weidenbach, S.; Zierler, S.; Schaefer, M.; Gudermann, T.; Chubanov, V. Pharmacological agents selectively acting on the channel moieties of TRPM6 and TRPM7. *Cell Calcium* **2022**, *106*, 102640. [CrossRef]
29. Krasteva, G.; Hartmann, P.; Papadakis, T.; Bodenbenner, M.; Wessels, L.; Weihe, E.; Schütz, B.; Langheinrich, A.C.; Chubanov, V.; Gudermann, T.; et al. Cholinergic chemosensory cells in the auditory tube. *Histochem. Cell Biol.* **2012**, *137*, 483–497. [CrossRef]
30. Zierler, S.; Yao, G.; Zhang, Z.; Kuo, W.C.; Pörzgen, P.; Penner, R.; Horgen, F.D.; Fleig, A. Waixenicin A inhibits cell proliferation through magnesium-dependent block of transient receptor potential melastatin 7 (TRPM7) channels. *J. Biol. Chem.* **2011**, *286*, 39328–39335. [CrossRef]
31. Sun, H.-S.; Horgen, F.D.; Romo, D.; Hull, K.G.; Kiledal, S.A.; Fleig, A.; Feng, Z.-P. Waixenicin A, a marine-derived TRPM7 inhibitor: A promising CNS drug lead. *Acta Pharmacol. Sin.* **2020**, *41*, 1519–1524. [CrossRef]
32. Qin, X.; Yue, Z.; Sun, B.; Yang, W.; Xie, J.; Ni, E.; Feng, Y.; Mahmood, R.; Zhang, Y.; Yue, L. Sphingosine and FTY720 are potent inhibitors of the transient receptor potential melastatin 7 (TRPM7) channels. *Br. J. Pharmacol.* **2013**, *168*, 1294–1312. [CrossRef] [PubMed]
33. Duan, J.; Li, Z.; Li, J.; Hulse, R.E.; Santa-Cruz, A.; Valinsky, W.C.; Abiria, S.A.; Krapivinsky, G.; Zhang, J.; Clapham, D.E. Structure of the mammalian TRPM7, a magnesium channel required during embryonic development. *Proc. Natl. Acad. Sci. USA* **2018**, *115*, E8201–E8210. [CrossRef] [PubMed]
34. Nadezhdin, K.D.; Correia, L.; Shalygin, A.; Aktolun, M.; Neuberger, A.; Gudermann, T.; Kurnikova, M.G.; Chubanov, V.; Sobolevsky, A.I. Structural basis of selective TRPM7 inhibition by the anticancer agent CCT128930. *Cell Rep.* **2024**, *43*, 114108. [CrossRef]
35. Voringer, S.; Schreyer, L.; Nadolni, W.; Meier, M.A.; Woerther, K.; Mittermeier, C.; Ferioli, S.; Singer, S.; Holzer, K.; Zierler, S.; et al. Inhibition of TRPM7 blocks MRTF/SRF-dependent transcriptional and tumorigenic activity. *Oncogene* **2020**, *39*, 2328–2344. [CrossRef]
36. Suzuki, S.; Penner, R.; Fleig, A. TRPM7 contributes to progressive nephropathy. *Sci. Rep.* **2020**, *10*, 2333. [CrossRef]
37. Schilling, T.; Miralles, F.; Eder, C. TRPM7 regulates proliferation and polarisation of macrophages. *J. Cell Sci.* **2014**, *127*, 4561–4566. [CrossRef]
38. Song, C.; Choi, S.; Oh, K.; Sim, T. Suppression of TRPM7 enhances TRAIL-induced apoptosis in triple-negative breast cancer cells. *J. Cell Physiol.* **2020**, *235*, 10037–10050. [CrossRef] [PubMed]
39. Chubanov, V.; Ferioli, S.; Wisnowsky, A.; Simmons, D.G.; Leitzinger, C.; Einer, C.; Jonas, W.; Shymkiv, Y.; Bartsch, H.; Braun, A.; et al. Epithelial magnesium transport by TRPM6 is essential for prenatal development and adult survival. *eLife* **2016**, *5*, e20914. [CrossRef]
40. Tian, Y.; Yang, T.; Yu, S.; Liu, C.; He, M.; Hu, C. Prostaglandin E2 increases migration and proliferation of human glioblastoma cells by activating transient receptor potential melastatin 7 channels. *J. Cell Mol. Med.* **2018**, *22*, 6327–6337. [CrossRef]
41. Davis, F.M.; Azimi, I.; Faville, R.A.; Peters, A.A.; Jalink, K.; Putney, J.W.; Goodhill, G.J.; Thompson, E.W.; Roberts-Thomson, S.J.; Monteith, G.R. Induction of epithelial-mesenchymal transition (EMT) in breast cancer cells is calcium signal dependent. *Oncogene* **2014**, *33*, 2307–2316. [CrossRef]
42. Rybarczyk, P.; Vanlaeys, A.; Brassart, B.; Dhennin-Duthille, I.; Chatelain, D.; Sevestre, H.; Ouadid-Ahidouch, H.; Gautier, M. The Transient Receptor Potential Melastatin 7 Channel Regulates Pancreatic Cancer Cell Invasion through the Hsp90alpha/uPA/MMP2 pathway. *Neoplasia* **2017**, *19*, 288–300. [CrossRef] [PubMed]
43. Rybarczyk, P.; Gautier, M.; Hague, F.; Dhennin-Duthille, I.; Chatelain, D.; Kerr-Conte, J.; Pattou, F.; Regimbeau, J.; Sevestre, H.; Ouadid-Ahidouch, H. Transient receptor potential melastatin-related 7 channel is overexpressed in human pancreatic ductal adenocarcinomas and regulates human pancreatic cancer cell migration. *Int. J. Cancer* **2012**, *131*, E851–E861. [CrossRef]
44. Franz, M.J.; Wenisch, P.; Wohlleben, P.; Rupprecht, L.; Chubanov, V.; Gudermann, T.; Kyheröinen, S.; Vartiainen, M.K.; Heinrich, M.R.; Muehlich, S. Identification of novel inhibitors of the transcriptional coactivator MRTF-A for HCC therapy. *Mol. Ther. Oncol.* **2024**, *32*, 200855. [CrossRef]
45. Huang, J.; Furuya, H.; Faouzi, M.; Zhang, Z.; Monteilh-Zoller, M.; Kawabata, K.G.; Horgen, F.D.; Kawamori, T.; Penner, R.; Fleig, A. Inhibition of TRPM7 suppresses cell proliferation of colon adenocarcinoma in vitro and induces hypomagnesemia in vivo without affecting azoxymethane-induced early colon cancer in mice. *Cell Commun. Signal* **2017**, *15*, 30. [CrossRef]
46. Liu, H.; Dilger, J.P.; Lin, J. Lidocaine Suppresses Viability and Migration of Human Breast Cancer Cells: TRPM7 as a Target for Some Breast Cancer Cell Lines. *Cancers* **2021**, *13*, 234. [CrossRef] [PubMed]
47. Liu, H.; Dilger, J.P.; Lin, J. The Role of Transient Receptor Potential Melastatin 7 (TRPM7) in Cell Viability: A Potential Target to Suppress Breast Cancer Cell Cycle. *Cancers* **2020**, *12*, 131. [CrossRef]

48. Middelbeek, J.; Kuipers, A.J.; Henneman, L.; Visser, D.; Eidhof, I.; van Horssen, R.; Wieringa, B.; Canisius, S.V.; Zwart, W.; Wessels, L.F.; et al. TRPM7 is required for breast tumor cell metastasis. *Cancer Res.* **2012**, *72*, 4250–4261. [CrossRef]
49. Guilbert, A.; Gautier, M.; Dhennin-Duthille, I.; Haren, N.; Sevestre, H.; Ouadid-Ahidouch, H. Evidence that TRPM7 is required for breast cancer cell proliferation. *Am. J. Physiol. Cell Physiol.* **2009**, *297*, C493–C502. [CrossRef]
50. Guilbert, A.; Gautier, M.; Dhennin-Duthille, I.; Rybarczyk, P.; Sahni, J.; Sevestre, H.; Scharenberg, A.M.; Ouadid-Ahidouch, H. Transient receptor potential melastatin 7 is involved in oestrogen receptor-negative metastatic breast cancer cells migration through its kinase domain. *Eur. J. Cancer* **2013**, *49*, 3694–3707. [CrossRef]
51. Meng, X.; Cai, C.; Wu, J.; Cai, S.; Ye, C.; Chen, H.; Yang, Z.; Zeng, H.; Shen, Q.; Zou, F. TRPM7 mediates breast cancer cell migration and invasion through the MAPK pathway. *Cancer Lett.* **2013**, *333*, 96–102. [CrossRef] [PubMed]
52. Liu, H.; Dilger, J.P.; Lin, J. A pan-cancer-bioinformatic-based literature review of TRPM7 in cancers. *Pharmacol. Ther.* **2022**, *240*, 108302. [CrossRef] [PubMed]
53. Gautier, M.; Perrière, M.; Monet, M.; Vanlaeys, A.; Korichneva, I.; Dhennin-Duthille, I.; Ouadid-Ahidouch, H. Recent Advances in Oncogenic Roles of theTRPM7 Chanzyme. *Curr. Med. Chem.* **2016**, *23*, 4092–4107. [CrossRef]
54. Dhennin-Duthille, I.; Gautier, M.; Korichneva, I.; Ouadid-Ahidouch, H. TRPM7 involvement in cancer: A potential prognostic factor. *Magnes. Res.* **2014**, *27*, 103–112. [CrossRef]
55. Köles, L.; Ribiczey, P.; Szebeni, A.; Kádár, K.; Zelles, T. The Role of TRPM7 in Oncogenesis. *Int. J. Mol. Sci.* **2024**, *25*, 719. [CrossRef]
56. Cordier, C.; Prevarskaya, N.; Lehen'kyi, V. TRPM7 Ion Channel: Oncogenic Roles and Therapeutic Potential in Breast Cancer. *Cancers* **2021**, *13*, 6322. [CrossRef] [PubMed]
57. Ji, D.; Fleig, A.; Horgen, F.D.; Feng, Z.-P.; Sun, H.-S. Modulators of TRPM7 and its potential as a drug target for brain tumours. *Cell Calcium* **2022**, *101*, 102521. [CrossRef]
58. Meng, S.; Alanazi, R.; Ji, D.; Bandura, J.; Luo, Z.-W.; Fleig, A.; Feng, Z.-P.; Sun, H.-S. Role of TRPM7 kinase in cancer. *Cell Calcium* **2021**, *96*, 102400. [CrossRef]
59. Schmidt, E.; Narangoda, C.; Nörenberg, W.; Egawa, M.; Rössig, A.; Leonhardt, M.; Schaefer, M.; Zierler, S.; Kurnikova, M.G.; Gudermann, T.; et al. Structural mechanism of TRPM7 channel regulation by intracellular magnesium. *Cell Mol. Life Sci.* **2022**, *79*, 225. [CrossRef] [PubMed]
60. Di Veroli, G.Y.; Fornari, C.; Wang, D.; Mollard, S.; Bramhall, J.L.; Richards, F.M.; Jodrell, D.I. Combenefit: An interactive platform for the analysis and visualization of drug combinations. *Bioinformatics* **2016**, *32*, 2866–2868. [CrossRef]
61. Loibl, S.; Gianni, L. HER2-positive breast cancer. *Lancet* **2017**, *389*, 2415–2429. [CrossRef]
62. Hoeger, B.; Nadolni, W.; Hampe, S.; Hoelting, K.; Fraticelli, M.; Zaborsky, N.; Madlmayr, A.; Sperrer, V.; Fraticelli, L.; Addington, L.; et al. Inactivation of TRPM7 Kinase Targets AKT Signaling and Cyclooxygenase-2 Expression in Human CML Cells. *Function* **2023**, *4*, zqad053. [CrossRef] [PubMed]
63. Essletzbichler, P.; Konopka, T.; Santoro, F.; Chen, D.; Gapp, B.V.; Kralovics, R.; Brummelkamp, T.R.; Nijman, S.M.; Bürckstümmer, T. Megabase-scale deletion using CRISPR/Cas9 to generate a fully haploid human cell line. *Genome Res.* **2014**, *24*, 2059–2065. [CrossRef] [PubMed]
64. Kollewe, A.; Chubanov, V.; Tseung, F.T.; Correia, L.; Schmidt, E.; Rössig, A.; Zierler, S.; Haupt, A.; Müller, C.S.; Bildl, W.; et al. The molecular appearance of native TRPM7 channel complexes identified by high-resolution proteomics. *eLife* **2021**, *10*, e68544. [CrossRef] [PubMed]
65. Scherer, W.F.; Syverton, J.T.; Gey, G.O. Studies on the propagation in vitro of poliomyelitis viruses. IV. Viral multiplication in a stable strain of human malignant epithelial cells (strain HeLa) derived from an epidermoid carcinoma of the cervix. *J. Exp. Med.* **1953**, *97*, 695–710. [CrossRef]
66. Jani, J.P.; Finn, R.S.; Campbell, M.; Coleman, K.G.; Connell, R.D.; Currier, N.; Emerson, E.O.; Floyd, E.; Harriman, S.; Kath, J.C.; et al. Discovery and pharmacologic characterization of CP-724,714, a selective ErbB2 tyrosine kinase inhibitor. *Cancer Res.* **2007**, *67*, 9887–9893. [CrossRef] [PubMed]
67. Greco, W.R.; Bravo, G.; Parsons, J.C. The search for synergy: A critical review from a response surface perspective. *Pharmacol. Rev.* **1995**, *47*, 331–385.
68. Blomen, V.A.; Májek, P.; Jae, L.T.; Bigenzahn, J.W.; Nieuwenhuis, J.; Staring, J.; Sacco, R.; van Diemen, F.R.; Olk, N.; Stukalov, A.; et al. Gene essentiality and synthetic lethality in haploid human cells. *Science* **2015**, *350*, 1092–1096. [CrossRef]
69. Wang, T.; Birsoy, K.; Hughes, N.W.; Krupczak, K.M.; Post, Y.; Wei, J.J.; Lander, E.S.; Sabatini, D.M. Identification and characterization of essential genes in the human genome. *Science* **2015**, *350*, 1096–1101. [CrossRef]
70. Findlay, G.M.; Daza, R.M.; Martin, B.; Zhang, M.D.; Leith, A.P.; Gasperini, M.; Janizek, J.D.; Huang, X.; Starita, L.M.; Shendure, J. Accurate classification of BRCA1 variants with saturation genome editing. *Nature* **2018**, *562*, 217–222. [CrossRef]
71. Robinson-Garcia, L.; da Silva, J.F.; Loizou, J.I. Synthetic Lethal Interactions for Kinase Deficiencies to DNA Damage Chemotherapeutics. *Cancer Res.* **2019**, *79*, 5693–5698. [CrossRef]
72. Mellott, A.; Rockwood, J.; Zhelay, T.; Luu, C.T.; Kaitsuka, T.; Kozak, J.A. TRPM7 channel activity in Jurkat T lymphocytes during magnesium depletion and loading: Implications for divalent metal entry and cytotoxicity. *Pflugers Arch.* **2020**, *472*, 1589–1606. [CrossRef] [PubMed]
73. Nahta, R. Pharmacological strategies to overcome HER2 cross-talk and Trastuzumab resistance. *Curr. Med. Chem.* **2012**, *19*, 1065–1075. [CrossRef] [PubMed]

74. Yang, L.; Bhattacharya, A.; Peterson, D.; Li, Y.; Liu, X.; Marangoni, E.; Robila, V.; Zhang, Y. Targeted dual degradation of HER2 and EGFR obliterates oncogenic signaling, overcomes therapy resistance, and inhibits metastatic lesions in HER2-positive breast cancer models. *Drug Resist. Updat.* **2024**, *74*, 101078. [CrossRef]
75. Levaot, N.; Hershfinkel, M. How cellular Zn2+ signaling drives physiological functions. *Cell Calcium* **2018**, *75*, 53–63. [CrossRef] [PubMed]
76. Chakraborty, M.; Hershfinkel, M. Zinc Signaling in the Mammary Gland: For. Better. and for Worse. *Biomedicines* **2021**, *9*, 1204. [CrossRef]
77. Rusch, P.; Hirner, A.V.; Schmitz, O.; Kimmig, R.; Hoffmann, O.; Diel, M. Zinc distribution within breast cancer tissue of different intrinsic subtypes. *Arch. Gynecol. Obstet.* **2021**, *303*, 195–205. [CrossRef]
78. Cui, Y.; Vogt, S.; Olson, N.; Glass, A.G.; Rohan, T.E. Levels of zinc, selenium, calcium, and iron in benign breast tissue and risk of subsequent breast cancer. *Cancer Epidemiol. Biomarkers Prev.* **2007**, *16*, 1682–1685. [CrossRef]
79. Wang, H.; Li, B.; Asha, K.; Pangilinan, R.L.; Thuraisamy, A.; Chopra, H.; Rokudai, S.; Yu, Y.; Prives, C.L.; Zhu, Y. The ion channel TRPM7 regulates zinc-depletion-induced MDMX degradation. *J. Biol. Chem.* **2021**, *297*, 101292. [CrossRef]
80. Strobaek, D.; Hougaard, C.; Johansen, T.H.; Sørensen, U.S.; Nielsen, E.Ø.; Nielsen, K.S.; Taylor, R.D.T.; Pedarzani, P.; Christophersen, P. Inhibitory gating modulation of small conductance Ca^{2+}-activated K+ channels by the synthetic compound (R)-N-(benzimidazol-2-yl)-1,2,3,4-tetrahydro-1-naphtylamine (NS8593) reduces afterhyperpolarizing current in hippocampal CA1 neurons. *Mol. Pharmacol.* **2006**, *70*, 1771–1782. [CrossRef]
81. Chubanov, V.; Schnitzler, M.M.Y.; Meißner, M.; Schäfer, S.; Abstiens, K.; Hofmann, T.; Gudermann, T. Natural and synthetic modulators of SK (K(ca)2) potassium channels inhibit magnesium-dependent activity of the kinase-coupled cation channel TRPM7. *Br. J Pharmacol* **2012**, *166*, 1357–1376. [CrossRef]

Supplementary information for publication I

I have included only the supplementary figures and screenshots from Suppl. Table S2. The corresponding Excel tables, which serve as the basis for the figures in my paper, can be accessed and downloaded via the following link if needed: https://www.mdpi.com/article/10.3390/cells13211801/s1.

Figure S1. Characterization of *TRPM7* KO-01 HAP1 cells.

(**A**) Sequence alignment of RT-PCR product obtained with primers flanking exon 4 of the human *TRPM7* gene. RT-PCR was performed using RNA extracted from *TRPM7* KO-01 HAP1 cells. Note that the aberrant transcript contains an intronic sequence (indicated by the red arrow), which was spliced between sequences encoded by exon 3 and the distal part of exon 4 of *TRPM7*. (**B**) Magnified sequence alignment of the intronic sequence found in the aberrant *TRPM7* transcript. (**C**) The sequence of RT-PCR product of the mutant *TRPM7* transcript containing the exon 3 (black sequence), intronic sequence (red sequence) and distal segment of exon 4 (blue sequence). In silico translation of the mutant transcript revealed that the mutation results in a frame-shift mutation.

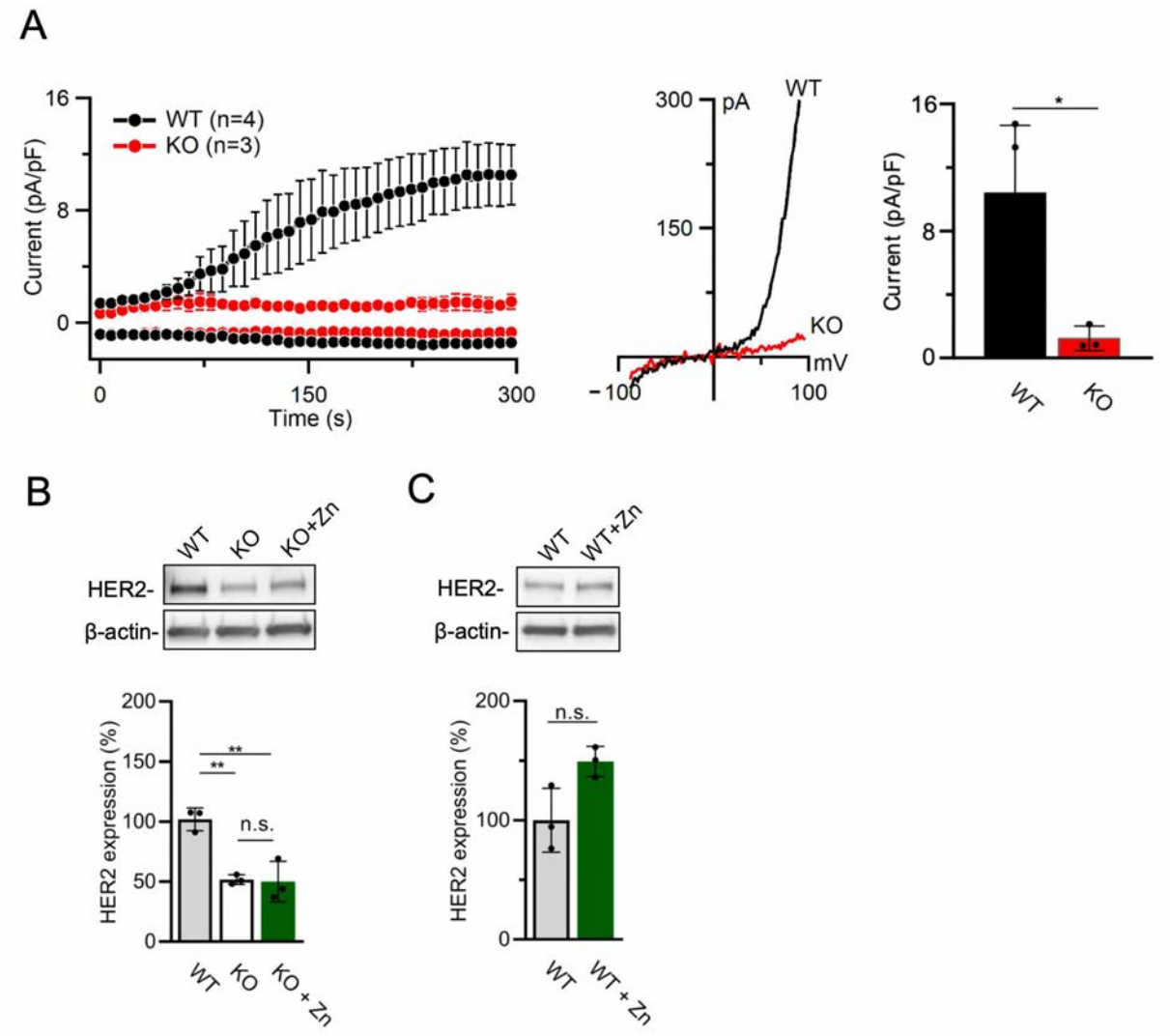

Figure S2. Assessment of human HeLa cells.

(**A**) Left panel: Whole-cell currents measured at −80 and +80 mV over time in wild-type (WT) and *TRPM7* KO (KO) HeLa cells. Middle panel: Representative current−voltage (I−V) relationships obtained at 300 s in measurements illustrated on the Left panel. Right panel: Bar graph of current amplitudes at +80 mV (300 s) illustrated on the Left panel. Data are mean ± SD; *n*, the number of cells examined. * $p \leq 0.05$; (one-way ANOVA). (**B**, **C**) Upper panels: Representative western blots obtained with WT (WT) and *TRPM7* KO (KO) HeLa cells maintained in the absence or presence of 10 μM $ZnCl_2$ (Zn). Equal volumes of cell lysates were assessed using anti-HER2 and anti-β-actin antibodies. Lower panels: Bar graphs showing normalized

HER2 expression levels in experiments from the Upper panels. The ratio of HER2 to anti-β-actin signals in WT cells (**B**) or untreated WT cells (**C**) was accounted as 100%. Data are mean ± SD of n = 3 independent experiments. ** $p \leq 0.01$; ns—not significantly different (one-way ANOVA).

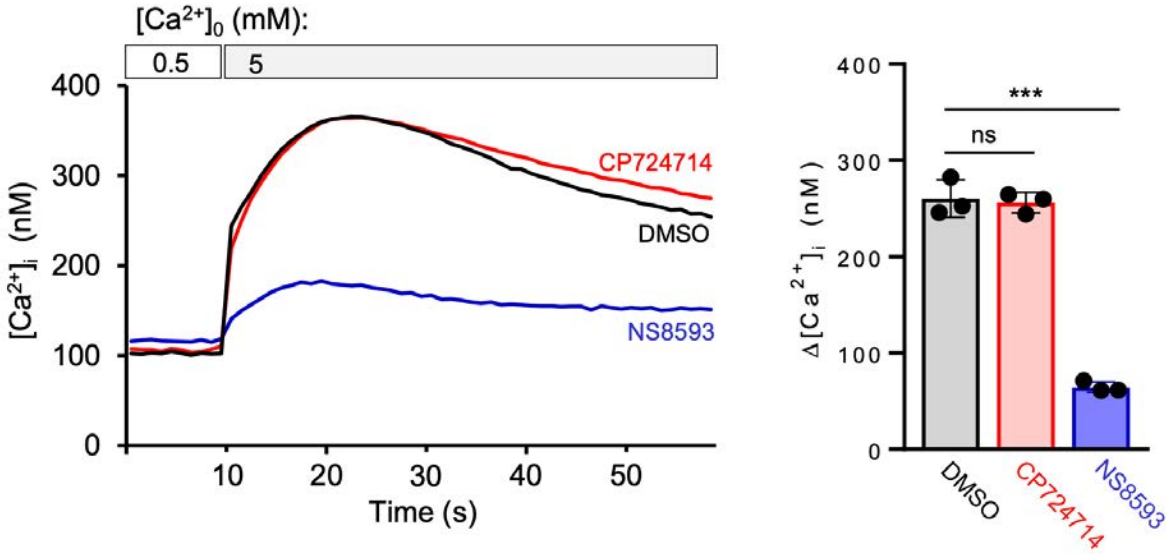

Figure S3. The effects of CP724714 and NS8593 on the TRPM7 channel.

Intracellular Ca^{2+} levels ($[24]_i$) were measured using a bioluminescence-based assay in WT HEK293 cells transfected with *Trpm7* plasmid DNA exposed to 10 μM CP724714, 10 μM NS8593 or equal DMSO volumes (DMSO). (**A**) $[Ca^{2+}]_i$ was measured in the presence of 0.5 or 10 mM external Ca^{2+} ($[Ca^{2+}]_o$) as indicated by the horizontal bars. Representative traces are shown from n = 3 independent experiments. (**B**) Ca^{2+} rises ($\Delta[Ca^{2+}]_i$, mean ± SD, n = 3) were calculated from measurements shown in **(A)** by subtraction of the resting $[Ca^{2+}]_i$ from the maximal $[Ca^{2+}]_i$ after application of 10 mM $[Ca^{2+}]_o$. *** $p \leq 0.001$; ns—not significantly different (one-way ANOVA).

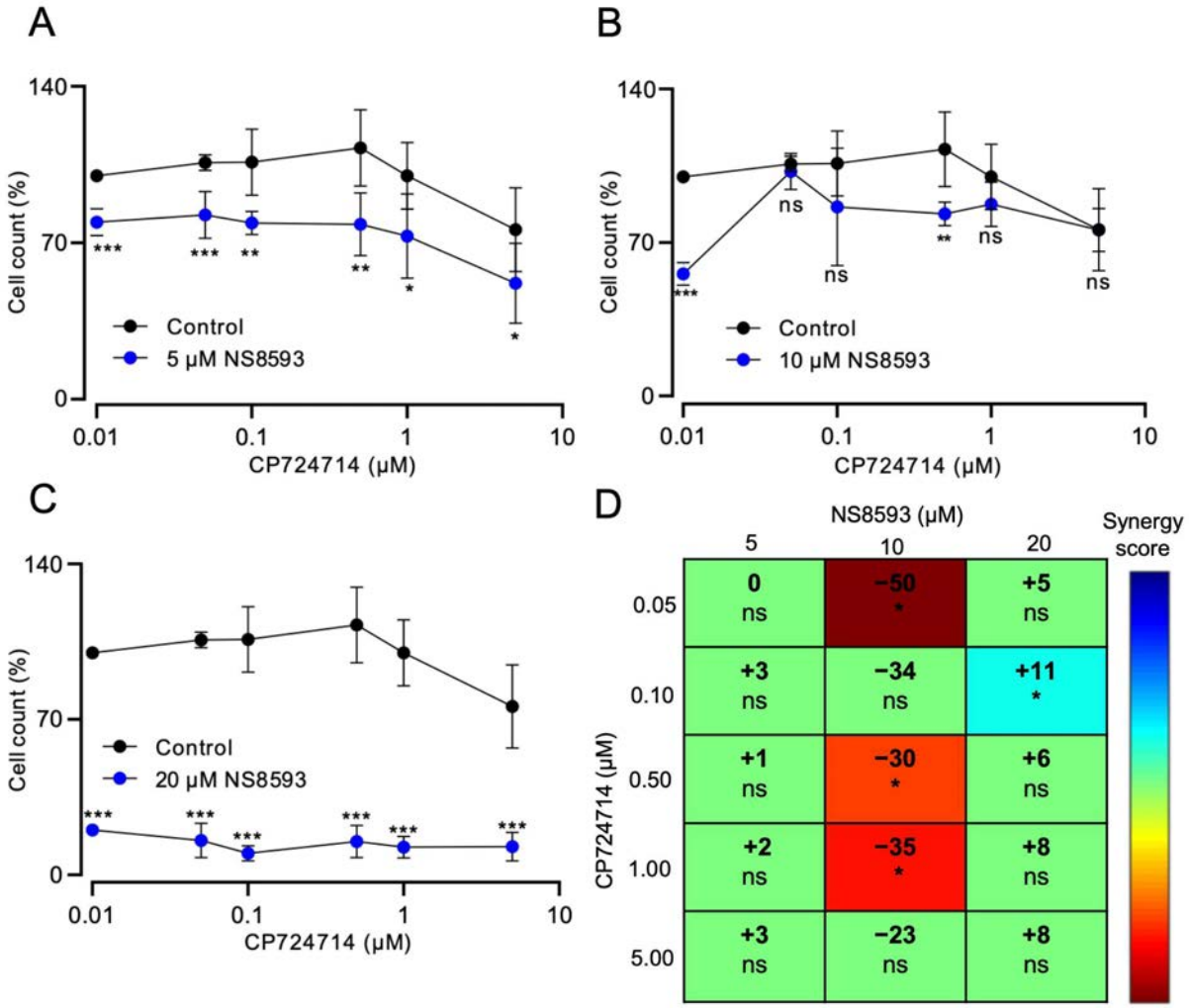

Figure S4. Combinatory treatment of MDA-MB-231 cells by NS8593 and CP724714. (**A–C**) Viability of MDA-MB-231 cells treated by different concentrations of CP724714 for 72 h in the absence (Control) and presence of 5 μM (**A**), 10 μM (**B**), or 20 μM (**C**) NS8593. Data are mean ± SD of n = 3 independent experiments. *** $p \leq 0.001$; ** $p \leq 0.01$; * $p \leq 0.05$; ns—not significantly different (one-way ANOVA). **D**, LOEWE synergy analysis of the cytotoxic effects elicited by NS8593 and CP724714 on MDA-MB-231 cells in (**A**–**C**). * $p \leq 0.05$; ns—not significantly different (one-way ANOVA).

Screenshot Worksheet 1 from Supplementary Excel Table S2:

			Linear expression level				Fold change from WT		
Affymetrix ID	Gene	Unigene	WT	KO-01	KO-04	WT+NS8593	KO-01	KO-04	WT+NS8593
8006906	ERBB2	Hs.446352	35,16	132,01	123,42	58,91	3,75	3,51	1,68
8044450	ZC3H6	Hs.190477	97,17	173,86	252,90	220,13	1,79	2,60	2,27
8102368	NEUROG2	Hs.744415	79,31	125,49	201,53	206,15	1,58	2,54	2,60
8135392	HBP1	Hs.162032	72,15	113,85	167,92	168,45	1,58	2,33	2,33
8113790	MARCH3	Hs.132441	226,41	389,20	516,74	451,85	1,72	2,28	2,00
8114326	FAM13B	Hs.567453	167,01	308,62	373,08	321,99	1,85	2,23	1,93
7973306	ABHD4	Hs.445665	147,34	233,99	308,91	289,17	1,59	2,10	1,96
7948332	LPXN	Hs.125474	33,43	50,36	68,07	62,34	1,51	2,04	1,87
7938329	SNORA23	Hs.689720	1018,12	1691,62	2070,50	1581,53	1,66	2,03	1,55
8133112	LOC84214	Hs.588334	35,87	64,66	71,40	63,35	1,80	1,99	1,77
8065242	LINC00652	Hs.584899	12,56	20,84	24,85	22,37	1,66	1,98	1,78
8133549	GTF2IRD2B	Hs.647039	45,84	69,11	89,33	82,80	1,51	1,95	1,81
8002897	TMEM231	Hs.156784	42,60	70,61	82,41	71,83	1,66	1,93	1,69
8140170	GTF2IRD2B	Hs.647039	45,60	70,34	87,77	83,08	1,54	1,92	1,82
8113059	MBLAC2	Hs.64004	107,77	171,94	200,29	171,21	1,60	1,86	1,59
8099506	TAPT1	Hs.479223	95,44	148,27	175,66	148,97	1,55	1,84	1,56
8084219	KLHL24	Hs.407709	81,51	125,54	145,17	204,79	1,54	1,78	2,51
8166184	CA5B	Hs.653287	428,17	648,28	754,16	750,43	1,51	1,76	1,75
8138602	DFNA5	Hs.520708	30,05	51,28	52,65	45,67	1,71	1,75	1,52
7941639	DPP3	Hs.502914	161,11	251,58	275,28	280,85	1,56	1,71	1,74
8174119	ZMAT1	Hs.496512	21,30	34,78	36,02	42,79	1,63	1,69	2,01
8076025	PLA2G6	Hs.170479	40,22	64,61	67,48	70,81	1,61	1,68	1,76
7900857	ST3GAL3	Hs.597915	67,98	115,34	112,15	107,83	1,70	1,65	1,59
8096919	ALPK1	Hs.652825	42,57	70,31	70,04	78,28	1,65	1,65	1,84
8003850	CYB5D2	Hs.513871	121,55	183,16	199,11	194,51	1,51	1,64	1,60
8058118	KCTD18	Hs.605775	82,48	126,25	131,28	125,39	1,53	1,59	1,52
8094476	TBC1D19	Hs.479403	84,04	129,48	132,77	146,44	1,54	1,58	1,74
7938925	NELL1	Hs.657172	55,22	95,84	86,74	87,12	1,74	1,57	1,58
8099721	SEL1L3	Hs.479384	151,55	361,97	237,27	249,94	2,39	1,57	1,65
8155192	GLIPR2	Hs.493819	135,10	204,47	205,68	208,84	1,51	1,52	1,55
7983828	TEX9	Hs.511476	66,41	103,82	100,60	99,49	1,56	1,51	1,50
8133770	CCDC146	Hs.113940	17,86	28,13	26,91	27,95	1,58	1,51	1,57

Screenshot Worksheet 2 from Supplementary Excel Table S2:

			Linear expression level				Fold change from WT		
Affymetrix ID	Gene	Unigene	WT	KO-01	KO-04	WT+NS8593	KO-01	KO-04	WT+NS8593
8170992	DKC1	Hs.4747	397,08	137,62	103,92	224,36	0,35	0,26	0,57
8164269	ENG	Hs.76753	90,27	40,23	46,91	58,01	0,45	0,52	0,64
8013987	RNY4P13	Hs.100379296	30,95	14,22	11,29	16,41	0,46	0,36	0,53
7952335	SNORD14E	Hs.85391	126,98	65,09	46,66	65,52	0,51	0,37	0,52
7952339	SNORD14C	Hs.180414	977,89	513,03	585,95	636,21	0,52	0,60	0,65
7904963	RNVU1-3	Hs.101954272	64,09	34,62	30,16	24,58	0,54	0,47	0,38
7915612	PTCH2	Hs.591497	58,95	32,36	32,58	24,97	0,55	0,55	0,42
7972826	LINC00346	Hs.245390	19,64	11,36	12,85	12,76	0,58	0,65	0,65
7983228	MAP1A	Hs.194301	173,88	105,54	93,99	99,43	0,61	0,54	0,57
7905329	MLLT11	Hs.75823	1278,12	815,90	730,06	627,20	0,64	0,57	0,49
7958019	DRAM1	Hs.525634	68,35	43,68	31,18	42,67	0,64	0,46	0,62
8177393	RBMY1B	Hs.725744	13,10	8,55	6,10	5,59	0,65	0,47	0,43

Table S2. Commonly up- and down-regulated transcripts after genetic and pharmacological inactivation of TRPM7 in HAP1 cells.

Excel file contains two worksheets: (**1**) Commonly ≥ 1.5-fold up-regulated Affymetrix probes in RNA extracted from *TRPM7* KO cells (clones KO-01 and KO-04) and parental wild-type (WT) cells treated with NS8593 (WT+NS8593) as compared to untreated parental WT cells; (**2**) Commonly ≥ 1.5-fold down-regulated Affymetrix probes in RNA extracted from *TRPM7* KO cells (clones KO-01 and KO-04) and parental WT cells treated with NS8593 (WT+NS8593) as compared to parental untreated WT cells.

6. Publication II

Title: Structural mechanism of TRPM7 channel regulation by intracellular magnesium

https://doi.org/10.1007/s00018-022-04192-7

Cellular and Molecular Life Sciences (2022) 79:225
https://doi.org/10.1007/s00018-022-04192-7

ORIGINAL ARTICLE

Structural mechanism of TRPM7 channel regulation by intracellular magnesium

Eva Schmidt[1] · Chamali Narangoda[2] · Wolfgang Nörenberg[3] · Miyuki Egawa[1] · Anna Rössig[1] · Marion Leonhardt[3] · Michael Schaefer[3] · Susanna Zierler[1,4] · Maria G. Kurnikova[2] · Thomas Gudermann[1,5] · Vladimir Chubanov[1]

Received: 22 October 2021 / Revised: 26 January 2022 / Accepted: 2 February 2022 / Published online: 7 April 2022

Abstract

Zn^{2+}, Mg^{2+} and Ca^{2+} are essential divalent cations implicated in many metabolic processes and signalling pathways. An emerging new paradigm is that the organismal balance of these cations predominantly depends on a common gatekeeper, the channel-kinase TRPM7. Despite extensive electrophysiological studies and recent cryo-EM analysis, an open question is how the channel activity of TRPM7 is activated. Here, we performed site-directed mutagenesis of mouse TRPM7 in conjunction with patch-clamp assessment of whole-cell and single-channel activity and molecular dynamics (MD) simulations to show that the side chains of conserved N1097 form an inter-subunit Mg^{2+} regulatory site located in the lower channel gate of TRPM7. Our results suggest that intracellular Mg^{2+} binds to this site and stabilizes the TRPM7 channel in the closed state, whereas the removal of Mg^{2+} favours the opening of TRPM7. Hence, our study identifies the structural underpinnings through which the TRPM7 channel is controlled by cytosolic Mg^{2+}, representing a new structure–function relationship not yet explored among TRPM channels.

Keywords TRPM7 · TRP channels · Magnesium · PIP_2 · ATP · Molecular dynamics simulations

Introduction

The transient receptor potential cation channel, subfamily M, member 7 (TRPM7) encodes a bi-functional protein comprising a transmembrane channel segment fused to a serine/threonine-protein kinase domain [1–3]. The TRPM7 channel is highly permeable to divalent cations, including Zn^{2+}, Ca^{2+}, and Mg^{2+}, and there is mounting evidence to suggest that the influx of all three cations underlies the indispensable physiological role of TRPM7 [4–8]. Thus, TRPM7 controls a wide range of biological processes such as organismal Zn^{2+}, Ca^{2+} and Mg^{2+} homeostasis, embryonic development, immune responses, cell motility, proliferation and differentiation [1–3].

TRPM7 currents were discovered in patch-clamp experiments with immune cells after removing Mg^{2+} from pipette solutions [9–11]. In contrast, the addition of free Mg^{2+} and Mg·ATP prevented the opening of the TRPM7 channel through different mechanisms [11–13]. Moreover, free Mg^{2+} and Mg·ATP inhibit TRPM7 synergistically, since elevation of free Mg^{2+} concentrations increases the potency of Mg·ATP [13]. TRPM7 currents were thus termed magnesium-nucleotide-regulated metal ion currents (MagNuM) and magnesium-inhibited cation currents (MIC) [11, 12]. In the past two decades, this experimental paradigm was commonly used to identify TRPM7 currents in a wide variety of primary isolated cells and stable cell lines [1–3]. The current consensus is that both Mg^{2+} and Mg·ATP act as negative

Maria G. Kurnikova: corresponding author for theoretical analysis.

✉ Thomas Gudermann
thomas.gudermann@lrz.uni-muenchen.de

✉ Vladimir Chubanov
vladimir.chubanov@lrz.uni-muenchen.de

1 Walther-Straub Institute of Pharmacology and Toxicology, LMU Munich, Munich, Germany

2 Chemistry Department, Carnegie Mellon University, Pittsburgh, PA, USA

3 Rudolf-Boehm Institute of Pharmacology and Toxicology, Leipzig University, Leipzig, Germany

4 Institute of Pharmacology, Johannes Kepler University Linz, Linz, Austria

5 Comprehensive Pneumology Center, a member of the German Center for Lung Research (DZL), Munich, Germany

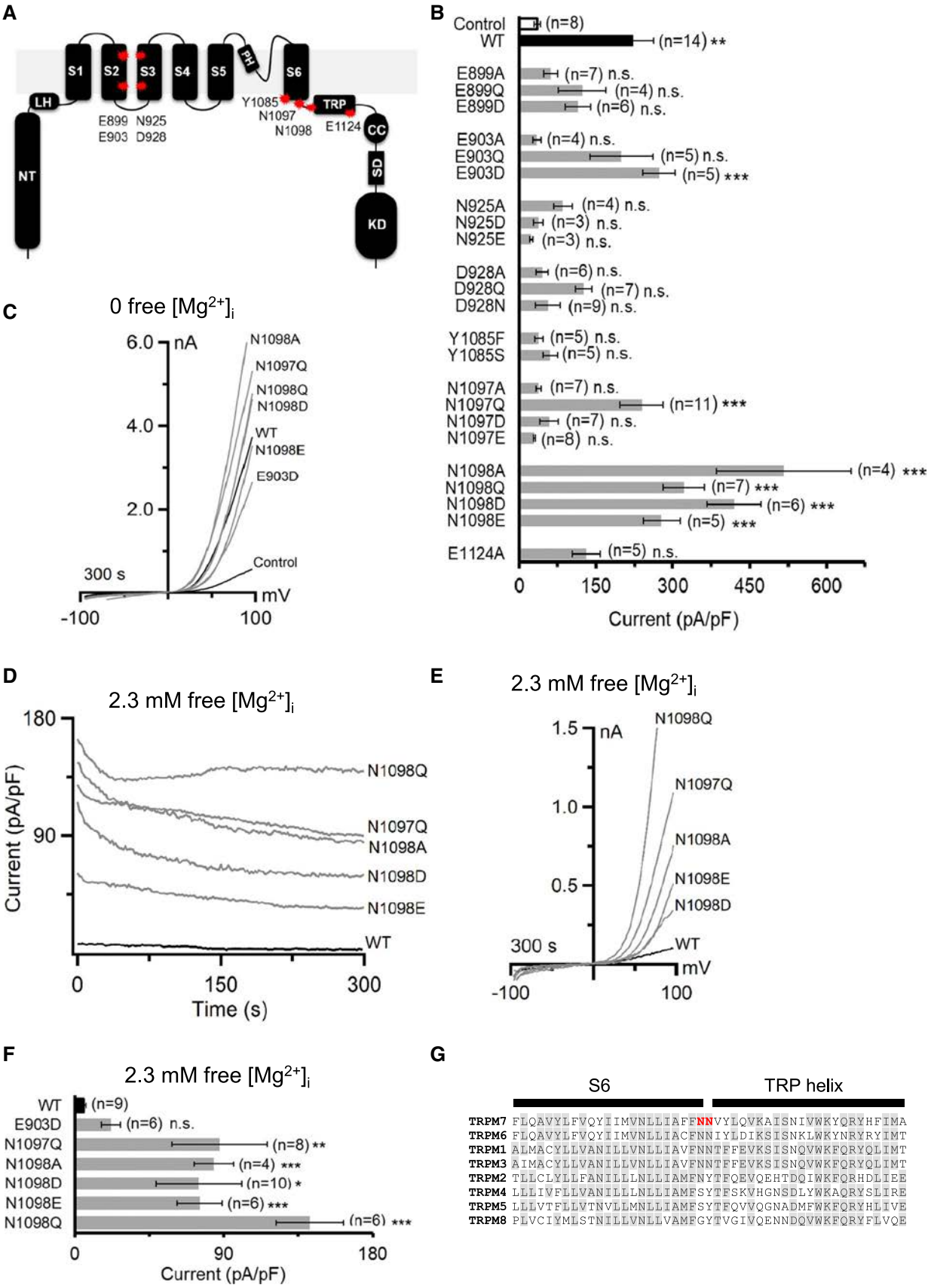
A
S1
S2
S3
S4
S5
PH
S6
LH
NT
E899 N925
E903 D928
Y1085
N1097
N1098
TRP
E1124
CC
SD
KD
B
Control
WT
(n=8)
(n=14) **
E899A
E899Q
E899D
(n=7) n.s.
(n=4) n.s.
(n=6) n.s.
E903A
E903Q
E903D
(n=4) n.s.
(n=5) n.s.
(n=5) ***
N925A
N925D
N925E
(n=4) n.s.
(n=3) n.s.
(n=3) n.s.
D928A
D928Q
D928N
(n=6) n.s.
(n=7) n.s.
(n=9) n.s.
Y1085F
Y1085S
(n=5) n.s.
(n=5) n.s.
N1097A
N1097Q
N1097D
N1097E
(n=7) n.s.
(n=11) ***
(n=7) n.s.
(n=8) n.s.
N1098A
N1098Q
N1098D
N1098E
(n=4) ***
(n=7) ***
(n=6) ***
(n=5) ***
E1124A
(n=5) n.s.
0
150
300
450
600
Current (pA/pF)
C
0 free [Mg2+]i
6.0 nA
4.0
2.0
N1098A
N1097Q
N1098Q
N1098D
WT
N1098E
E903D
Control
300 s
mV
-100
100
D
2.3 mM free [Mg2+]i
180
90
Current (pA/pF)
N1098Q
N1097Q
N1098A
N1098D
N1098E
WT
0
150
300
Time (s)
E
2.3 mM free [Mg2+]i
1.5 nA
1.0
0.5
N1098Q
N1097Q
N1098A
N1098E
N1098D
WT
300 s
mV
-100
100
F
2.3 mM free [Mg2+]i
WT
E903D
N1097Q
N1098A
N1098D
N1098E
N1098Q
(n=9)
(n=6) n.s.
(n=8) **
(n=4) ***
(n=10) *
(n=6) ***
(n=6) ***
0
90
180
Current (pA/pF)
G
S6
TRP helix
TRPM7 FLQAVYLFVQYIIMVNLLIAFFNNVYLQVKAISNIVWKYQRYHFIMA
TRPM6 FLQAVYLFVQYIIMVNLLIACFNNIYLDIKSISNKLWKYNRYRYIMT
TRPM1 ALMACYLLVANILLVNLLIAVFNNTFFEVKSISNQVWKFQRYQLIMT
TRPM3 AIMACYLLVANILLVNLLIAVFNNTFFEVKSISNQVWKFQRYQLIMT
TRPM2 TLLCLYLLFANILLLNLLIAMFNYTFQEVQEHTDQIWKFQRHDLIEE
TRPM4 LLLIVFLLVANILLLNLLIAMFSYTFSKVHGNSDLYWKAQRYSLIRE
TRPM5 LLLVTFLLVTNVLLMNLLIAMFSYTFQVVQGNADMFWKFQRYHLIVE
TRPM8 PLVCIYMLSTNILLVNLLVAMFGYTVGIVQENNDQVWKFQRYFLVQE

◂**Fig. 1** Assessment of the mouse TRPM7 variants expressed in HEK293T cells. **A** Domain topology of TRPM7. A large N-terminus (*NT*) of TRPM7 is linked to a pre-S1 helix also known as a linker-helical domain (*LH*) preceding a channel segment comprising six transmembrane helices (*S1–6*) with a short pore loop and a pore helix (*PH*) located between S5 and S6. The C-terminus of TRPM7 contains a receptor potential domain (*TRP*) followed by a coiled-coil (*CC*), kinase substrate (*SD*) and kinase (*KD*) domains. Red stars indicate the position of residues in the mouse TRPM7 protein subjected to site-directed mutagenesis in the present study. **B** Whole-cell currents measured in untransfected HEK293T cells (Control, white) and the cells transfected by wild type (WT, black) or indicated mutant variants (grey) of TRPM7-YFP cDNAs. Currents were induced using the standard $[Mg^{2+}]_i$-free intracellular solution and the standard external solution. Current amplitudes (mean ± SEM) were acquired at + 80 mV (at 300 s). *n*, number of cells measured; n.s., not significant; $*P<0.05$ $**P<0.01$; $***P<0.001$ (ANOVA, compared to Control). **C** Representative I–V relationships of currents shown in **B**. **D–F** A subset of TRPM7-YFP variants shown in **B** were examined using an intracellular solution containing 2.3 mM $[Mg^{2+}]_i$ (Suppl. Table S1). **D** Whole-cell currents measured in WT and indicated mutant variants of TRPM7-YFP. Current amplitudes (mean ± SEM) were acquired at − 80 and + 80 mV and plotted over time. **E** Representative I–V relationships of currents (at 300 s) illustrated in (**D**). **F** Bar graphs of outward currents (mean ± SEM; + 80 mV) shown in (D) at 300 s. *n*, number of cells measured; n.s., not significant; $*P<0.05$ $**P<0.01$; $***P<0.001$ (ANOVA, compared to WT). **G** Multiple sequence alignment (ClustalW) of amino acid sequences encoding the S6 and TRP segments in the mouse TRPM1 – 8 proteins. Grey background indicates the sequence consensus. N1097 and N1098 of TRPM7 are indicated in red

regulators of the ubiquitously expressed TRPM7 channel to correlate the uptake of essential metals with the metabolic state of the cell [1–3].

The molecular mechanism determining TRPM7 sensitivity to intracellular Mg^{2+} remains unclear. Previously, several research groups examined the role of the C-terminal kinase domain with regard to TRPM7 channel sensitivity to Mg^{2+} and obtained controversial results. Thus, deletion of the kinase domain resulted in either non-functional versions of the channel [14], channel variants with unchanged [15] or even increased sensitivity to free Mg^{2+} [5, 15, 16]. In other studies, the introduction of 'kinase-dead' point mutations (D1775A and K1648R) in the catalytic site of the kinase moiety or deletion of phosphorylation residues (S1511 and S1567) did not affect the responses of the channel to free Mg^{2+} [14, 17, 18]. However, other researchers observed that TRPM7 with 'kinase-dead' mutations (K1648R and G1799D) exhibited reduced responses to free Mg^{2+} [5, 13], whereas the T1482L mutation affecting a putative phosphorylation site in TRPM7 increased Mg^{2+} sensitivity of the channel [19]. While the reason for such inconsistencies remains unclear, the overall consensus is that functional TRPM7 channel variants with impaired kinase moiety retain the sensitivity to intracellular free Mg^{2+}, arguing that an additional Mg^{2+} regulatory domain must exist.

Other studies suggested that Mg^{2+} affects the TRPM7 channel indirectly, for instance, by interfering with the interaction of phosphatidylinositol 4,5-bisphosphate (PIP_2) and TRPM7, but the structural basis of such interference remains unknown [20–22]. More recently, high-resolution structures of a closed TRPM7 channel were resolved by cryo-electron microscopy (cryo-EM) [23]. However, structural rearrangements associated with the Mg^{2+}- and PIP_2-dependent opening of the TRPM7 channel were not identified in the structures available [23].

Here, we embark on extensive functional analysis, structural modelling and molecular dynamics simulations and propose that a pivotal Mg^{2+} regulatory site of TRPM7 is located within the lower channel gate. Our findings suggest that Mg^{2+} interacts directly with this protein segment and stabilizes TRPM7 in the closed state. In line with this model, we found that a point mutation introduced in the Mg^{2+} regulatory site abolishes the sensitivity of TRPM7 to physiological concentrations of intracellular Mg^{2+}.

Results

Search for amino acid residues involved in the Mg^{2+}-induced inhibition of TRPM7

Recently, several structures of TRPM channels were determined using cryo-EM [24–33]. The investigators noted that TRPM2, TRPM4, TRPM5 and TRPM8 harbour intra-subunit Ca^{2+}-binding sites formed by five negatively charged and polar residues in the S2 and S3 helices and the TRP segment (Suppl. Fig. S1) [24–33]. Interestingly, some of these residues are substituted in TRPM1, TRPM3, TRPM6 and TRPM7 (Suppl. Fig. S1), suggesting that the latter group of channels may contain a binding pocket for another ligand, for instance, Mg^{2+}. To test this hypothesis functionally, we exchanged E899, E903, N925, D928 and E1124 of TRPM7 to an uncharged alanine residue (A) or two structurally related acidic (D or E) and two polar residues (Q or N) (Fig. 1A).

In the pore domain formed by the S5 and S6 helices, the polar side chains of N1097 and N1098 appear to arrange the narrowest constriction in the lower gate of TRPM7 [23]. Since asparagine side chains frequently contribute to Mg^{2+}-binding sites in other channels [34, 35], we hypothesized that N1097 and N1098 could function as an Mg^{2+} recognition site in TRPM7. Accordingly, we produced versions of TRPM7 with modified amino acids at positions N1097 and N1098 (Fig. 1A). Finally, we introduced changes in Y1085 (Fig. 1A) since its side chain hydroxyl group is located in the upper channel gate and may potentially interact with Mg^{2+} [23]. Because of the exceptionally low efficiency of in vitro site-directed mutagenesis of untagged

mouse TRPM7 cDNA in the bicistronic pIRES2-EGFP vector, the functional impact of the introduced mutations was investigated using mouse TRPM7 with a C-terminal YFP tag in the pcDNA3.1 vector (see further details in "Materials and methods").

First, we studied whether the TRPM7 mutants can be activated in the absence of cytosolic Mg^{2+}, assuming that mutations with a specific impact on Mg^{2+}-dependent inhibition of the channel should not significantly affect current amplitudes and current–voltage (I–V) relationships of TRPM7 in such an experimental setting. To this end, we transiently transfected HEK293T cells with cDNAs encoding wild-type (WT) and mutant versions of TRPM7-YFP and conducted patch-clamp experiments with YFP-positive cells. Whole-cell currents were elicited by a voltage ramp protocol ranging from − 100 to + 100 mV and a standard Mg^{2+}-free internal solution (Fig. 1B, C). I–V relationships of WT currents exhibited characteristic features, such as tiny inward and large outward currents with a pronounced rectification and a reversal potential of about 0 mV (Fig. 1C). Accordingly, outward currents of TRPM7 variants were used to reliably quantify the effects of the mutations (Fig. 1B). Only six mutant variants (E903D, N1097Q, N1098A, N1098Q, N1098D and N1098E) displayed currents significantly different from endogenous currents in untransfected cells (Fig. 1B). In addition, I–V relationships of these mutant channels resembled those of WT currents (Fig. 1C). Consequently, only the latter six TRPM7 variants were selected for further analysis.

Next, we examined the channel activity of WT and mutant TRPM7 variants in the presence of relatively high levels of intracellular Mg^{2+}. As expected, the addition of free 2.3 mM $[Mg^{2+}]_i$ to the internal solution completely prevented the development of WT currents (Fig. 1D, F). Five channel variants (N1097Q, N1098A, N1098Q, N1098D and N1098E) displayed currents already after break-in, which were modestly reduced over time and exhibited typical I–V characteristics (Fig. 1F, D). In contrast, the E903D variant showed low activity under these experimental conditions (Fig. 1F). Hence, unlike other mutations, exchanges of asparagine residues located in the S6 segment and the TRP helix (Fig. 1G) resulted in active TRPM7 channels in the presence of $[Mg^{2+}]_i$. Consequently, we selected the N1097Q and N1098Q variants for a more detailed assessment.

Impact of N1097Q and N1098Q mutations on TRPM7 channel inhibition by $Mg^{2+}$and Ba^{2+}

To rule out a potential influence of the YFP tag on the functional analysis of TRPM7, we re-introduced the N1097Q and N1098Q amino acid exchanges into mouse TRPM7 cDNA inserted into the bicistronic pIRES2-EGFP vector [36, 37]. Immunofluorescent staining of HEK293T cells expressing WT and mutant versions of TRPM7 did not reveal differences in the subcellular distribution of the proteins (Suppl. Fig. S2).

Next, we performed patch-clamp experiments to examine the impact of N1097Q and N1098Q on the concentration-dependent suppression of the channel by free $[Mg^{2+}]_i$ (Fig. 2). The calculated IC_{50} value for WT currents was 0.47 mM (Fig. 2A, B). Currents in cells expressing TRPM7 carrying the N1097Q mutation were inhibited by $[Mg^{2+}]_i$ with an IC_{50} value of 3.74 mM (Fig. 2C, D). As $[Mg^{2+}]_i$ varies between 0.5 and 1.0 mM in most mammalian cells [41], these results suggest that, unlike the WT channel, the N1097Q variant remains active in the presence of physiological concentrations of Mg^{2+}. Remarkably, TRPM7 containing N1098Q was highly active after break-in and remained active over time in the presence of the whole range of $[Mg^{2+}]_i$ examined, thus precluding a reliable calculation of an IC_{50} value (Fig. 2E, F). These results indicate that the N1098Q mutation results in a constitutively active channel insensitive to physiological concentrations of intracellular Mg^{2+}.

Apart from Mg^{2+}, other divalent cations (Ba^{2+}, Ca^{2+} and Zn^{2+}) can suppress TRPM7 currents presumably through a common regulatory site [38]. Hence, we examined whether the N1097Q and N1098Q mutants interfered with the effects of free $[Ba^{2+}]_i$ (0.55 and 1 mM) on the TRPM7 channel variants (Figure S3). We observed that the WT TRPM7 channel was inactive in the presence of both concentrations of free $[Ba^{2+}]_i$ (Suppl. Fig. S3A). The N1097Q variant showed significantly reduced currents only after administration of 1 mM free $[Ba^{2+}]_i$ (Suppl. Fig. S3B), whereas the N1098Q channel remained unaffected under both experimental conditions (Suppl. Fig. S3C).

Effects of N1097Q and N1098Q mutations on TRPM7 channel suppression by Mg·ATP and Mg·GTP

Previously, extensive electrophysiological analyses revealed that free Mg^{2+} and Mg·ATP inhibit TRPM7, most likely through different ligand binding sites [12, 13]. Interestingly, the elevation of free Mg^{2+} levels increased the potency of Mg·ATP, suggesting that Mg^{2+} and Mg·ATP act synergistically on the TRPM7 channel [12, 13]. Therefore, to further verify the role of N1097Q and N1098Q, we compared the concentration-dependent inhibition of the TRPM7 channel variants by intracellular concentrations of Mg·ATP $[Mg{\cdot}ATP]_i$, in the presence of only 250 µM free $[Mg^{2+}]_i$. The physiological intracellular concentrations of ATP vary between 2 and 9 mM in most mammalian cells [39]. In a physiological saline solution, the apparent K_d of Mg·ATP

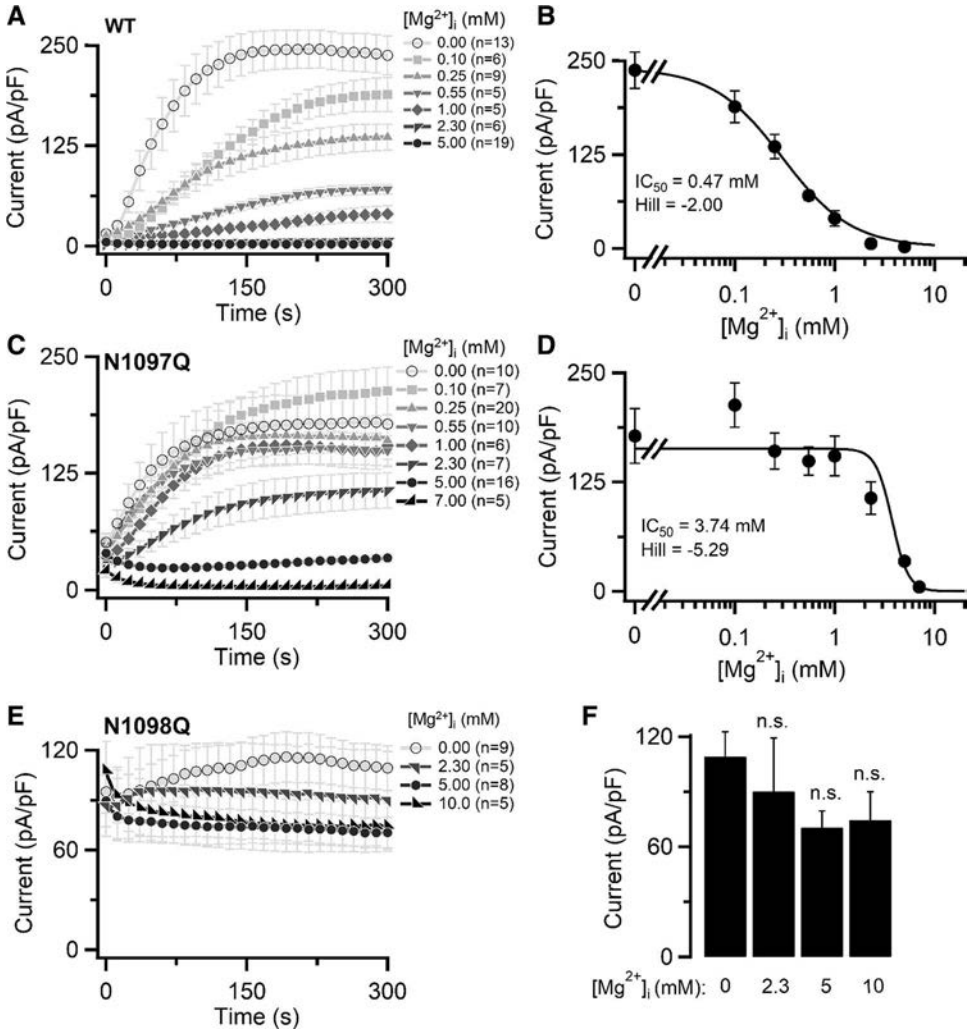

Fig. 2 Inhibition of TRPM7 currents by cytosolic Mg^{2+}. Whole-cell currents measured in HEK293T cells transfected by WT (**A, B**), N1097Q (**C, D**) and N1098Q (**E, F**) variants of TRPM7 cDNAs in pIRES2-EGFP expression vectors. **A**, **C**, **E** Current amplitudes (mean ± SEM) were measured at + 80 mV using internal solutions containing the indicated free $[Mg^{2+}]_i$ (Suppl. Table S1) and plotted over time. **B**, **D** Concentration-dependent suppression of currents (+ 80 mV, 300 s) shown in (**A**, **B**). The Hill equation was fitted to determine IC_{50} and the Hill factor. **F** Bar graphs of outward currents (mean ± SEM; + 80 mV) shown in (**E**) at 300 s. *n*, number of cells measured

is ~50 µM [40] and it was estimated that >90% of cytosolic ATP is present as Mg·ATP [41]. Using internal solutions covering this range of $[Mg{\cdot}ATP]_i$, we found that WT currents were suppressed with an IC_{50} value of 2.07 mM (Fig. 3A, B). By contrast, TRPM7 mutants N1097Q and N1098Q were characterized by a remarkably low sensitivity to $[Mg{\cdot}ATP]_i$ at all concentrations examined (Fig. 3C–F). Due to experimental limitations, $[Mg{\cdot}ATP]_i$ above 10 mM could not be reliably examined. Since other Mg·nucleotides (like Mg·GTP) were also capable of suppressing the TRPM7 channel, presumably through a mechanism shared with Mg·ATP [12, 13], we asked whether co-administration of 6 mM $[Mg{\cdot}GTP]_i$ and 250 µM free $[Mg^{2+}]_i$ will recapitulate the effects of 6 mM $[Mg{\cdot}ATP]_i$ co-applied with 250 µM free $[Mg^{2+}]_i$ (Suppl. Fig. S4). We observed that the impact of the N1097Q and N1098Q mutations on the channel's response to both Mg·nucletides were not different in such experimental settings (Suppl. Fig. S4).

Next, we examined the effects of 9 mM $[Mg{\cdot}ATP]_i$ in the presence of the physiological range of $[Mg^{2+}]_i$ concentrations using an internal solution containing 550 µM and 1 mM free $[Mg^{2+}]_i$. We found that WT currents were entirely suppressed under these conditions (Fig. 3G, Suppl. Fig. S5). In contrast, N1097Q mutant TRPM7 channel currents developed in the presence of 550 µM free $[Mg^{2+}]_i$ (Fig. 3G), but were undetectable after application of 1 mM free $[Mg^{2+}]_i$ (Suppl. Fig. S5). These results suggest that the N1097Q channel variant remained sensitive to Mg·ATP, but only in the presence of high concentrations of free Mg^{2+}, in accord with the idea that Mg^{2+} and Mg·ATP independently interact with different TRPM7 channel sites [12, 13], and that the N1097Q mutation primarily affected the Mg^{2+} regulatory mechanism. The N1098Q variant was not suppressed in all experimental settings (Fig. 3E, Suppl. Fig. S5), indicating that the N1098Q mutation engendered a constitutively active channel variant.

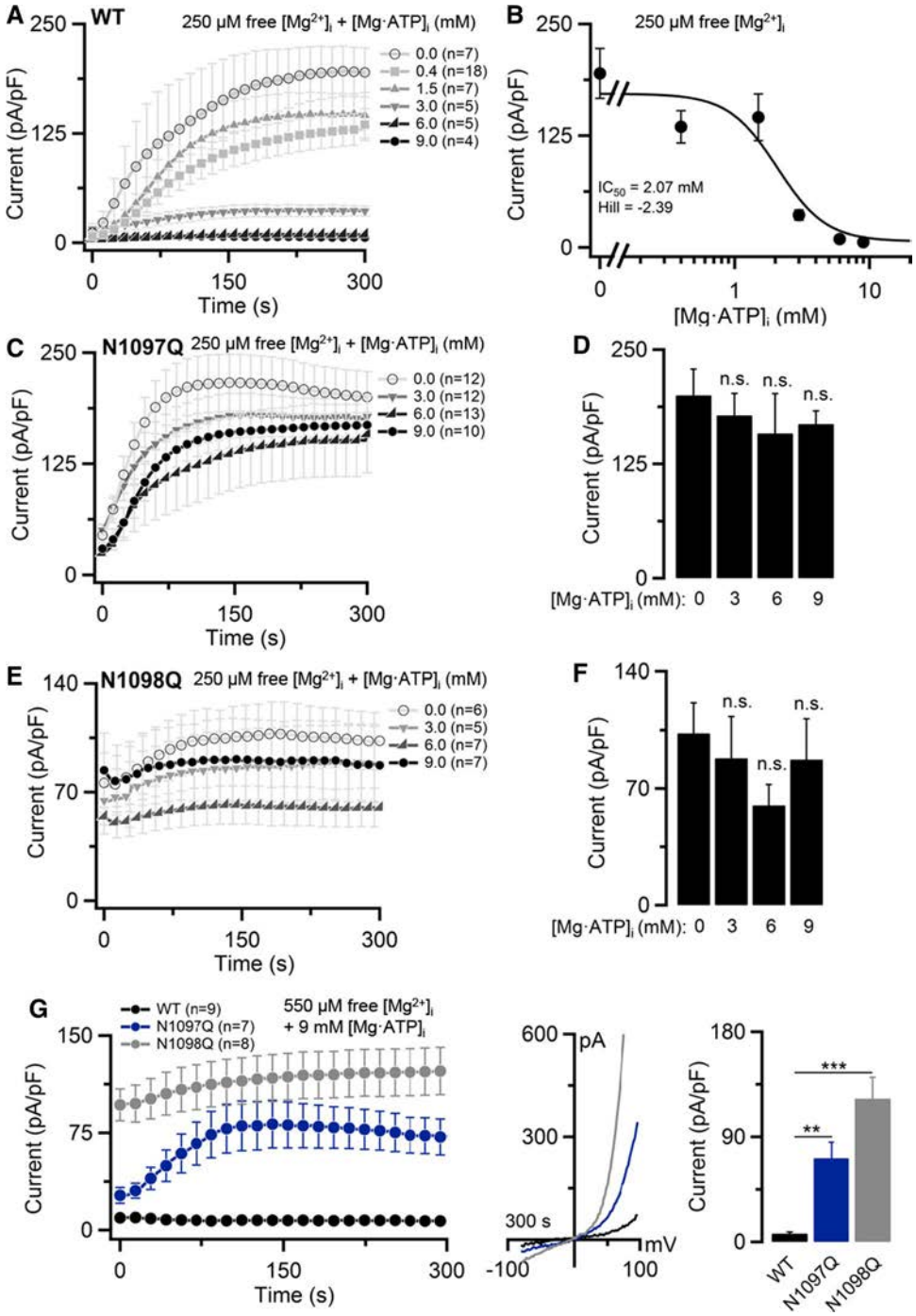

Fig. 3 Inhibition of TRPM7 currents by cytosolic Mg·ATP. Whole-cell currents measured in HEK293T cells transfected by WT, N1097Q and N1098Q variants of TRPM7 cDNAs (in pIRES2-EGFP). **A, B** Concentration-dependent suppression of WT TRPM7 by $[Mg{\cdot}ATP]_i$ in the presence of 250 µM free $[Mg^{2+}]_i$ (Suppl. Table S3). **A** Current amplitudes of the WT channel (mean ± SEM) measured at + 80mV were plotted over time. **B** Concentration–response curve for currents shown in **A** (+ 80 mV, 300 s). The Hill equation was used to determine IC_{50} and the Hill factor. **C–F** Effects of $[Mg{\cdot}ATP]_i$ on the N1097Q (**C**, **D**) and N1098Q (**E**, **F**) variants of TRPM7. Measurements were performed as in **A**. However, bar graphs of outward currents (mean ± SEM; + 80 mV) at 300 s were used to analyse the effects of $[Mg{\cdot}ATP]_i$. **G** Whole-cell currents were measured in the presence of 9 mM $[Mg{\cdot}ATP]_i$ and 550 µM free $[Mg^{2+}]_i$ (Suppl. Table S4). *Left panel* current amplitudes (mean ± SEM) acquired at + 80 mV were plotted over time. *Middle panel* representative current–voltage (I–V) relationships of currents (at 300 s) illustrated in the *left panel*. *Right panel* bar graphs of outward currents (mean ± SEM; + 80 mV) shown in the *left panel* at 300 s. *n*, number of cells measured; ns, not significant; $^{**}P < 0.01$, $^{***}P < 0.001$ (ANOVA)

Finally, we aimed to assess the activity of TRPM7 variants without manipulations of the cytosolic contents of Mg^{2+} and Mg·ATP using perforated patch recordings (Suppl. Fig. S6). Consistent with earlier studies [21], WT currents did not develop in this experimental setting, presumably because resting concentrations of Mg^{2+} and Mg·ATP are sufficient to inhibit TRPM7. On the contrary, channel activity of the N1097Q or N1098Q variants was well detectable (Suppl. Fig. S6), supporting the notion that the N1097Q or N1098Q mutations diminish the inhibitory

effects of both Mg^{2+} and Mg·ATP in resting HEK293T cells.

Effects of N1097Q and N1098Q on the sensitivity of TRPM7 to pharmacological agents and PIP_2 depletion

To determine whether the N1097Q or N1098Q amino acid exchanges altered the sensitivity of TRPM7 exclusively to $[Mg^{2+}]_i$ and $[Mg{\cdot}ATP]_i$ or caused more general changes of regulatory characteristics of the channel, we studied the effects of small synthetic molecules acting as activators or inhibitors of the TRPM7 channel. First, we assessed the action of naltriben, a potent agonist of the TRPM7 channel [42]. In these experiments, we used intracellular solutions containing 9 mM $[Mg{\cdot}ATP]_i$ and 550 µM free $[Mg^{2+}]_i$. The external application of naltriben led to a fast stimulation of WT and N1097Q currents (Fig. 4A, B). The N1098Q variant did not respond to naltriben (Fig. 4C).

Next, we examined the effect of NS8593, a potent TRPM7 inhibitor [43]. In these experiments, we induced currents using the standard $[Mg^{2+}]_i$-free intracellular pipette solution and externally applied NS8593 when currents were fully developed (Fig. 5). We noted that NS8593 caused a rapid inhibition of WT and N1097Q currents (Fig. 5A, B). In analogy to the effects of naltriben (Fig. 4A), the N1098Q mutation abolished the channel's sensitivity to NS8593 (Fig. 5C), indicating that the N1098Q mutant is functionally different from the N1097Q variant with regard to its sensitivity to natural or synthetic ligands.

It is well documented that depletion of plasma membrane PIP_2 results in the inactivation of the TRPM7 channel [20–22]. Therefore, we investigated the response of the TRPM7 variants to such a treatment using a voltage-sensitive phosphatase from *Ciona intestinalis* (Ci-VSP) [44]. Ci-VSP reduces PIP_2 levels in the plasma membranes at positive membrane potentials (Fig. 6A). A catalytically silent mutant of Ci-VSP (Ci-VSP-C363S) cannot hydrolyse PIP_2 and was used as a control (Fig. 6A). Cells co-expressing Ci-VSP or Ci-VSP-C363S together with TRPM7 variants were held at − 60 mV to allow induction of TRPM7 currents without activation of Ci-VSP. Then the regular voltage ramp ranging

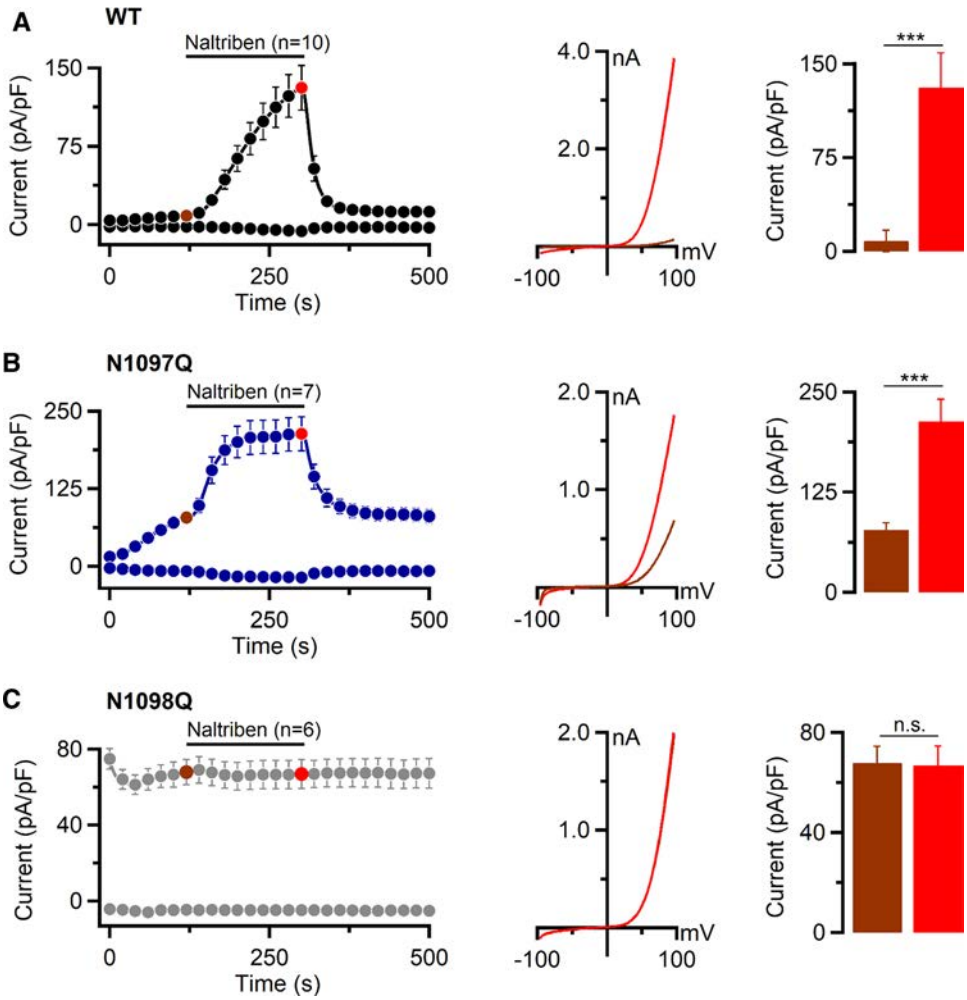

Fig. 4 Activation of TRPM7 currents by naltriben. Whole-cell currents were measured in HEK293T cells transfected by WT (**A**), N1097Q (**B**) and N1098Q (**C**) variants of TRPM7 cDNAs (in pIRES2-EGFP). *Left panels* current amplitudes (mean ± SEM) were measured at − 80 and + 80 mV and plotted over time. Currents were measured using an intracellular solution containing 9 mM $[Mg{\cdot}ATP]_i$ and 550 µM $[Mg^{2+}]_i$ and the standard external solution with or without 100 µM naltriben as indicated by the black bars. *Middle panels* representative I–V relationships obtained from individual ramps before (brown) and after (red) naltriben application as indicated in the *left panels* by coloured data points. *Right panels* bar graphs of outward currents (+ 80 mV, mean ± SEM) obtained before (brown) and after (red) naltriben application as indicated in the *left panels* by coloured data points. *n*, number of cells measured; ns, not significant; ***$P<0.001$ (two-tailed *t* test)

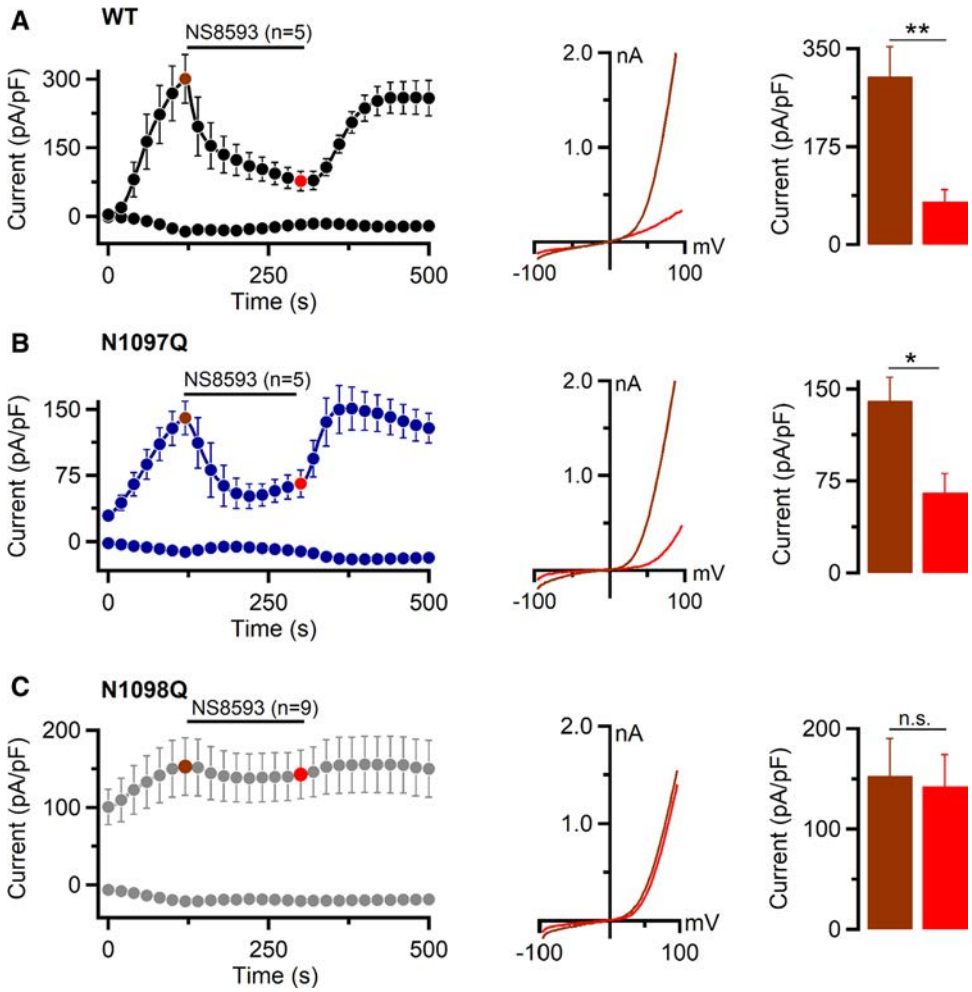

Fig. 5 Effects of NS8593 on TRPM7 currents. Whole-cell currents were measured in HEK293T cells transfected by WT (**A**), N1097Q (**B**), and N1098Q (**C**) variants of TRPM7 cDNAs (in pIRES2-EGFP) expressed in HEK293T cells. *Left panels* current amplitudes (mean ± SEM) were acquired at − 80 and + 80 mV and plotted over time. Currents were induced using the standard $[Mg^{2+}]_i$-free intracellular solution and the standard external solution. When currents were activated, the cells were exposed to the standard external solution with 10 µM NS8593 as indicated by the black bars. *Middle panels* representative I–V relationships obtained from individual ramps before (brown) and after (red) NS8593 application as indicated in the *left panels* by coloured data points. *Right panels* bar graphs of outward currents (+ 80 mV, mean ± SEM) obtained before (brown) and after (red) NS8593 application as indicated in the *left panels* by coloured data points. *n*, number of cells measured; ns, not significant; $*P<0.05$; $**P<0.01$ (two-tailed *t* test)

from − 100 to + 100 mV was applied to activate Ci-VSP and record TRPM7 currents (Fig. 6B). We found that Ci-VSP, but not Ci-VSP-C363S, suppressed WT and N1097Q currents similarly (Fig. 6C, D). In contrast, N1098Q currents were not affected by Ci-VSP and Ci-VSP-C363S (Fig. 6E). Hence, the N1097Q channel resembles the WT channel in the sensitivity to naltriben, NS8593 and PIP_2 depletion by Ci-VSP, whereas the N1098Q variant represents a constitutively active channel insensitive to these agents.

Assessment of TRPM7 channel variants in a divalent cation-free (DVF) extracellular solution

A well-known characteristic feature of TRPM7 is the permeation block of the channel pore by extracellular divalent cations [12], causing the characteristic shape of the I–V relationship of TRPM7 currents in the presence of divalent cations in external solutions (Fig. 1C). However, exposure of TRPM7-expressing cells to a DVF solution abolish such a permeation block and entails large monovalent cation currents with a distinguishing semi-linearized I–V relationship [12]. We examined whether N1097Q or N1098Q would affect this channel feature. As illustrated in Suppl. Fig. S7, application of DVF solution to the WT channel caused rapid increases of outward and inward currents accompanied with expected alterations in the I–V relationships. After the removal of the DVF solution, this characteristic I–V relationship of TRPM7 was reversed. We also noted that the N1097Q or N1098Q variants recapitulated the response of WT TRPM7 (Suppl. Fig. S7), indicating that N1097Q or N1098Q did not impinge on the function of the ion selectivity filter of TRPM7.

Impact of N1097Q on TRPM7 characteristics in excised outside-out patches

For a more thorough examination of the hypothesis that the N1097Q mutation affected the sensitivity of TRPM7 to intracellular Mg^{2+}, we thought to analyse TRPM7 on the single-channel level. However, our extensive attempts to measure TRPM7 currents in inside-out patches were unsuccessful. Therefore, we used previously established experimental

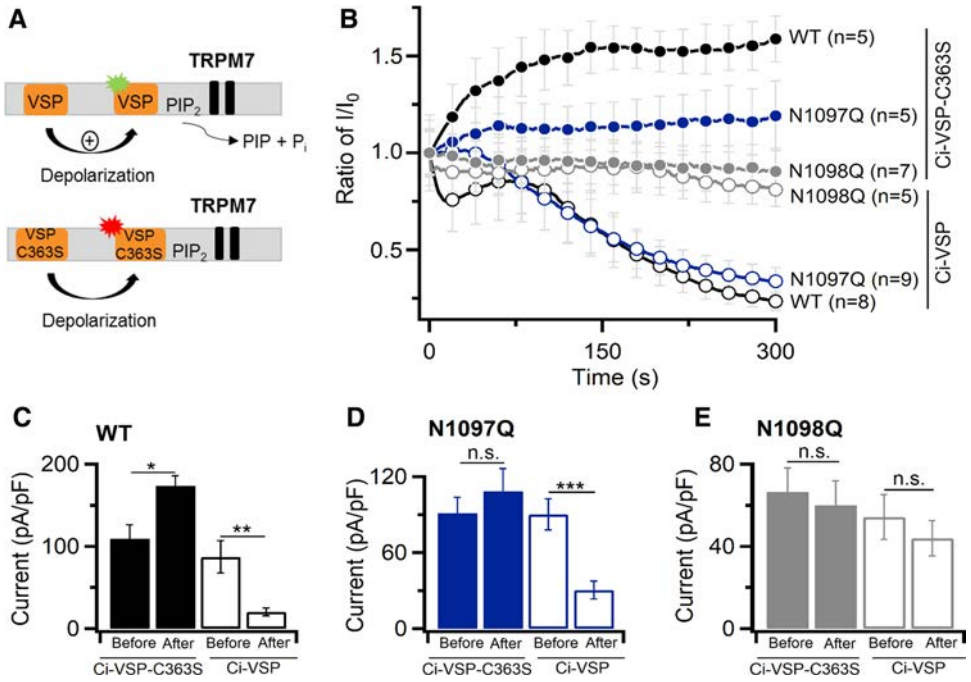

Fig. 6 Assessment of TRPM7 currents after PIP_2 depletion. **A** A diagram showing how wild-type voltage-sensitive phosphatase from *Ciona intestinalis* (Ci-VSP) reduces PIP_2 levels in the plasma membranes. A catalytically silent mutant of Ci-VSP (Ci-VSP-C363S) is unable to affect PIP_2 contents. **B** Time-dependent changes of normalized whole-cell outward currents in HEK293T cells transfected with WT, N1097Q and N1098Q variants of TRPM7 cDNA and Ci-VSP or Ci-VSP-C363S. Cells were held at − 60 mV for 2 min to allow induction of TRPM7 without activation of Ci-VSP. Then the voltage ramp ranging from − 100 to + 100 mV was applied to activate Ci-VSP and record TRPM7 currents. Current amplitudes (+ 80 mV) were normalized to the initial currents (mean ± SEM) and plotted over time. Data points are shown for every 10's ramp. *n*, number of cells measured. **C**–**E** Bar graphs of outward currents (+ 80 mV, mean ± SEM) shown in **B** immediately and after 300 s of application of voltage ramps from − 100 to + 100 mV. ns, not significant; $*P<0.05$; $**P<0.01$; $***P<0.001$ (two-tailed *t* test)

settings to analyse TRPM7 activity in excised outside-out patches [45]. To this end, outside-out patches were excised from transfected HEK293 cells and voltage clamped to − 60 mV. TRPM7 activity was evoked by exchanging the standard bath solution with a divalent cations-free (no-DIV) solution. This manoeuvre elicited only multichannel responses, irrespective of whether patches were from WT- or N1097Q-expressing cells, precluding an analysis of single-channel kinetics in these experimental settings (Suppl. Figure 8A, B). Nevertheless, differences between the WT and N1097Q channels were well evident. Single-channel amplitudes and the sojourns in the open state were about twice as large in the WT channels (Suppl. Fig. S8A, B). Estimated form a subset of experiments in which current–voltage relationships could be obtained, the calculated single-channel slope conductances (γ_s) were 41.4 ± 2.5 pS and 23.8 ± 2.4 pS for the WT and N1097Q, respectively [$n = 7$; see Suppl. Fig. S8C for examples; Suppl. Table S5 provides auxiliary chord conductance values (γ_c) from a larger sample]. The corresponding surrogate mean open times (T_{OS}), an admittedly rough estimate for the duration of the open state, were 4.7 ± 0.6 ms and 1.5 ± 0.3 ms for the WT and N1097Q channel variants, respectively. Despite shortening of T_{OS}, N1097Q did not affect the open probability (NP_O) (Suppl. Fig. S8C and Table S5), suggesting that the N1097Q mutation facilitated gating motions in the TRPM7 protein. Interestingly, besides a 40 pS main level, at least one additional subconductance state for TRPM7 has been described [46]. However, the all-points histograms derived from our data (Fig. 5A, C) showed evenly spaced peaks and lack of overt humps and, therefore, do not point to a significant contribution of such a subconductance state to the overall conductance under our experimental conditions.

To assess the effects of intracellular Mg^{2+} on channel characteristics, we used a pipette solution containing 1 mM free Mg^{2+}. All outside-out patches from cells overexpressing the WT channel exposed to no-DIV solution showed only an initial burst of channel openings followed by lasting quiescence (Fig. 7A, B). Single-channel current amplitudes assessed during the initial outbreaks of activity (− 2.3 ± 0.18 pA, Fig. 7A) were similar to those obtained in the absence of intracellular Mg^{2+} (− 2.2 ± 0.21 pA; Suppl. Fig. S8, Table S5). N1097Q behaved differently from the WT channel. Exposure to no-DIV solution induced sustained channel

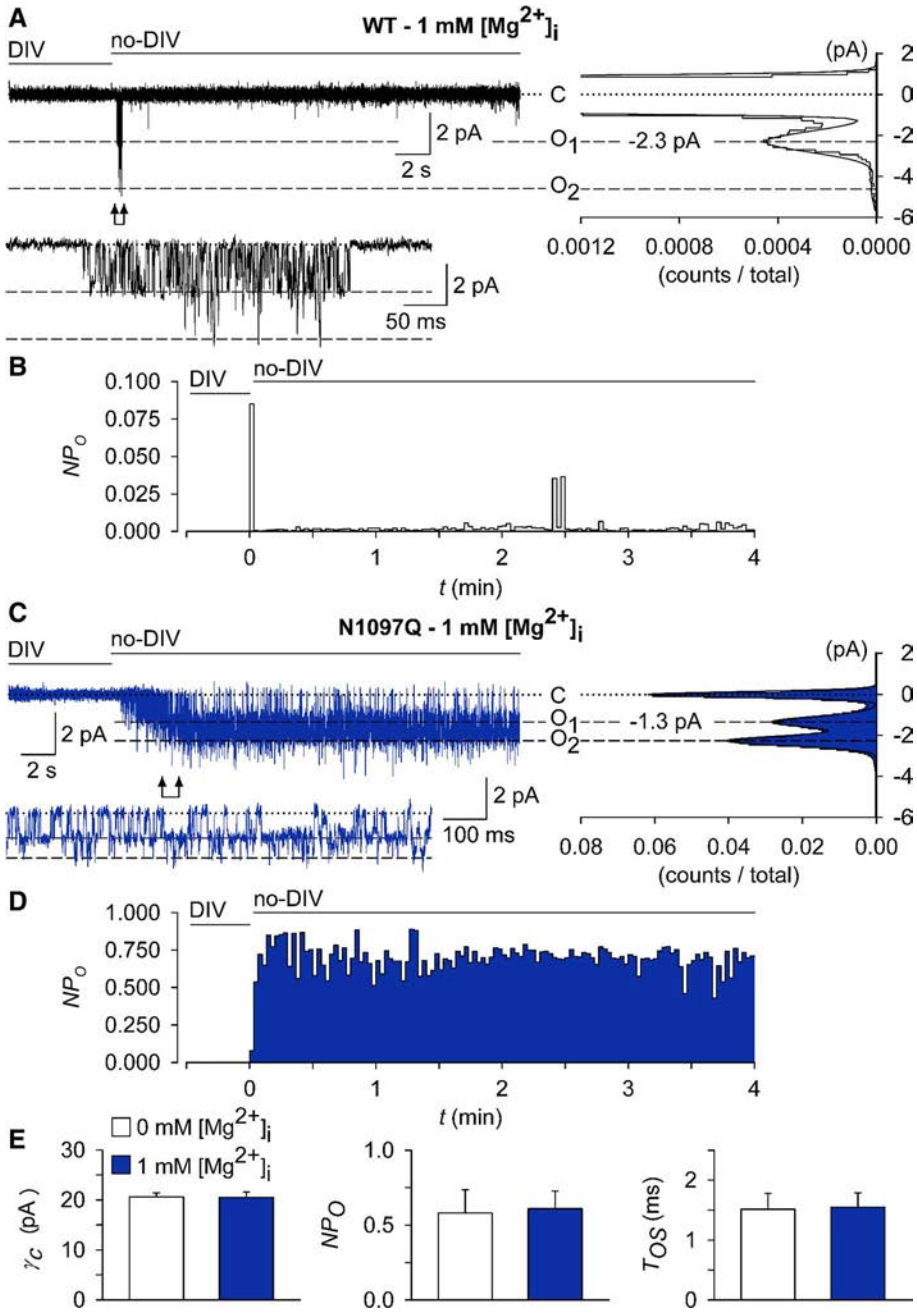

Fig. 7 Impact of intracellular Mg^{2+} on single-channel currents from TRPM7 variants. Currents were recorded at a holding potential of − 60 mV in outside-out membrane patches excised from HEK293 cells expressing WT (**A**, **B**) and N1097Q (**C**–**E**) variants of TRPM7. The WT (**A**) or N1097Q (**C**) channels were unblocked by removing the extracellular divalent cations (DIV bath) using a no-DIV solution, as indicated above the current traces. The intracellular solution was no-DIV augmented by 1 mM Mg^{2+}. Insets: currents on an expanded time scale from the segments indicated by arrows. The graphs on the right show all-point histograms from the two 30 s current traces. The dotted line indicates the closed level (**C**). The broken lines indicate the current level for one channel (*O1*) or two channels (*O2*) being open. Single-channel amplitudes (i) taken from O1 were − 2.3 pA and − 1.3 pA for WT channels (**A**) and N1097Q (**C**), respectively. **B**, **D** The open probabilities (NP_O) assessed for bins of 2 s over the whole 4.5 min duration of the experiments shown in (**A**, **C**). Note the different ordinate scaling in **B** and **D**. **E** Statistical evaluation of outside-out recordings with the N1097Q channel. Note that intracellular Mg^{2+} did not affect single-channel chord conductance (γ_c), NP_O and open time (T_{OS}; $n = 7$ each)

activity of the N1097Q variant, with the NP_O being stable over the whole time of current recordings (Fig. 7C, D). All measured channel characteristics, including chord conductance, NP_O, and T_{OS} were not affected by adding 1 mM intracellular Mg^{2+} (Fig. 7E, Table S5). Finally, using the same experimental settings, we analysed the effects of 2.9 mM $[Mg{\cdot}ATP]_i$ and 250 µM free $[Mg^{2+}]_i$ and observed that the WT channel exhibited only an initial burst of channel openings, whereas the N1097Q variant was active and displayed functional characteristics similar to those obtained in the presence of 1 mM free Mg^{2+} (Suppl. Fig. S9). These results corroborate with our analysis of whole-cell currents reinforcing the idea that the N1097Q substitution abrogated the inhibition of the TRPM7 channel by physiological intracellular Mg^{2+} concentrations.

Modelling and molecular dynamics (MD) simulations of the wild-type and mutant variants of the TRPM7 channel in closed and open conformations

To elucidate a mechanism by which N1097 and N1098 contribute to TRPM7 channel regulation, we opted for protein modelling and MD simulations of the TRPM7 ion

channel domain. The TRPM7 structure in Mg^{2+}-free conditions (PDB 5ZX5) showed the highest resolution of the S5–S6 segment in TRPM7, and, therefore, it was selected for analysis. To perform MD simulations, we constructed a 3D model of the closed channel pore-forming segment of TRPM7 (S4–S5 linker, S5–S6 helices and TRP domain) embedded in a lipid membrane and surrounded by water and ions (Fig. 8A). To develop a TRPM7 open channel structure, we used the homology modelling method. Initially, we attempted to use the open structure of the zebrafish TRPM2 channel as a template [32]. However, the open TRPM2 channel displayed significant conformational changes in the S5 helix driven by the interaction of charged residues in the S4–S5 linker and the TRP box, which are not conserved in TRPM7. Therefore, our analysis relied on the open structure of the human TRPV6 channel (PDB: 6BO8 [47]) (Suppl. Fig. S10).

The homology-modelled open channel structure then was used in targeted MD simulations to open the channel in lipid and water (Fig. 8). We observed that in the

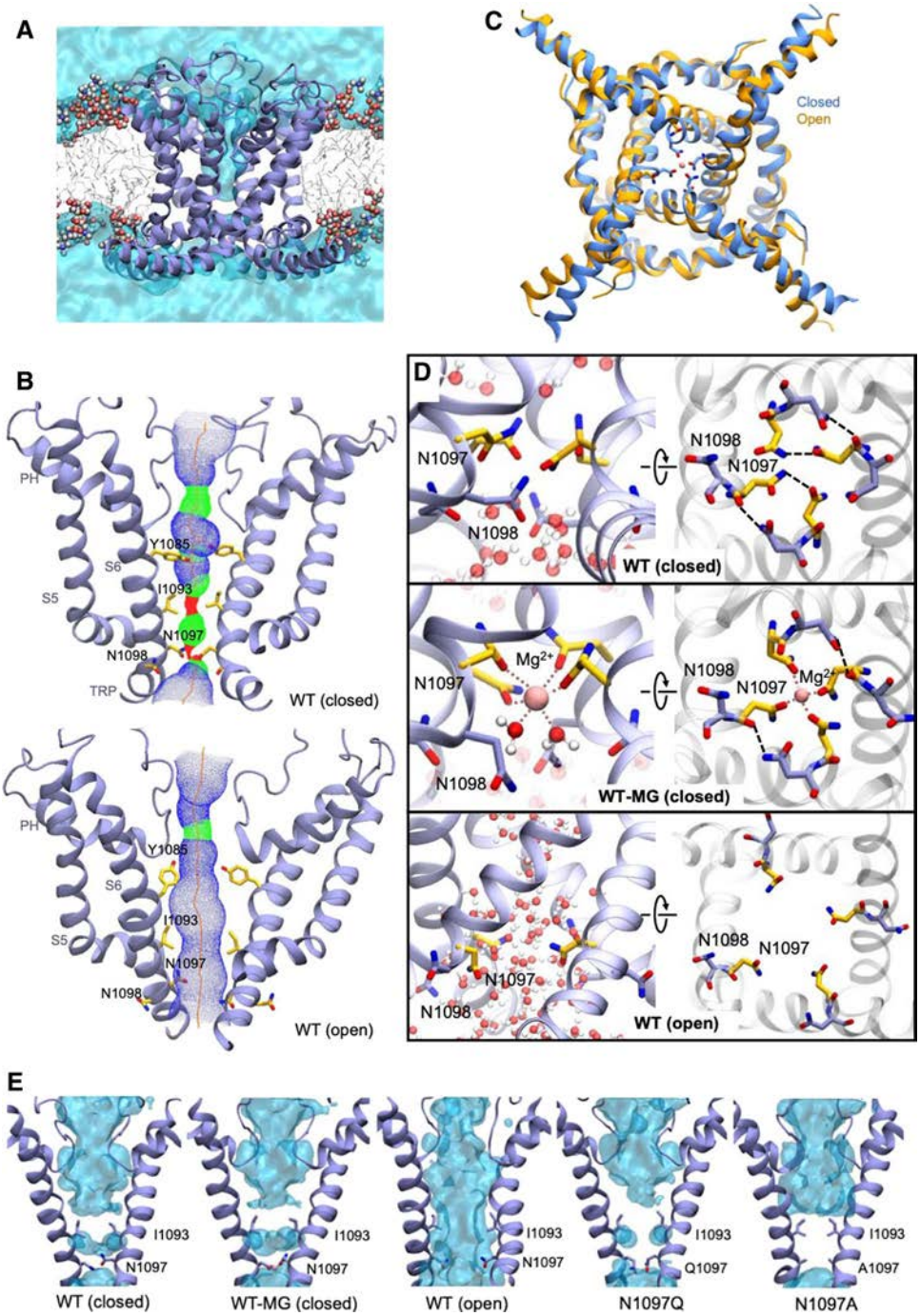

Fig. 8 Models of the channel pore-forming segment of mouse TRPM7 in lipid and water environments in closed and open conformations. **A** A representative structure of the mouse WT TRPM7 simulated channel unit (residues 982 to 1123) in the lipid bilayer and water. **B** A side view of a channel structure in the closed (top panel) and open (bottom panel) conformations. The channel pore-lining residues are shown. **C** Overlap of the closed structure an open structure shown (bottom view). **D** Structure of the channel gate in the closed channel with or without Mg^{2+} and open channel. Persistent water molecules are shown in red. Dashed lines indicate hydrogen bonds formed between N1097 and N1098 residues and Mg^{2+}. Note that the hydrogen bonds are transient, and the specific interactions shown are not present in all frames of the trajectory. **E** Channel's hydration in the simulations is shown for the WT, N1097A and N1097Q variants. Water is shown as a semi-transparent light blue continuum

closed state of the channel, the side chains of I1093 formed a hydrophobic seal excluding water from the channel (Fig. 8E), whereas polar side chains of N1097 build the narrowest segment of the cation permeation path in the pore (Fig. 8B). We found that transient inter-subunit hydrogen bonds were formed between N1097 residues of different subunits and between N1097 and N1098 residues. The most prominent hydrogen bonds were formed between the side chain amino and carbonyl groups of N1097 residues of adjacent subunits and between the side chain amino group of N1098 and the backbone carbonyl group of N1097 of adjacent subunits (Fig. 8D). On average, 3.6 inter-subunit hydrogen bonds involving N1097 and N1098 were present in the tetramer during the simulation (Suppl. Table S6). Our analysis suggests that these hydrogen bonds serve to stabilize the closed state of the channel gate (Fig. 8B, D).

MD simulation of TRPM7 in the open channel state revealed several remarkable structural rearrangements compared to the closed pore state (Fig. 8B, D). Specifically, we observed a loss of the hydrophobic seal formed by I1093 and significantly increased distance between the side chains of N1097. Inter-subunit hydrogen bonds formed by N1097 and N1098 were nearly absent with an average of 0.36 (Suppl. Table S6). Next, we performed MD simulations with Mg^{2+} placed in the pocket formed by the four N1097 in the closed channel (Fig. 8D). We found that Mg^{2+} steadily interacted with the side chain carbonyl groups of N1097 and two water molecules (Fig. 8C, D), stabilizing the closed state of TRPM7.

Finally, we performed MD simulations of the N1097A, N1097Q, N1098Q mutants. The N1097A channel formed a tightly closed gate due to the hydrophobicity of A1097 downstream to the hydrophobic seal formed by I1093 (Fig. 8E), thus explaining the silencing of the channel variant in patch-clamp experiments (Fig. 1). In the absence of Mg^{2+}, the N1097Q variant behaved similarly to the WT channel (Fig. 8E). However, MD simulations in the presence of Mg^{2+} revealed that Mg^{2+} lost coordination with three out of the four side chains of Q1097 (Suppl. Figure 11A), thus explaining the shift in concentration–response Mg^{2+} inhibition of the N1097Q channel (Fig. 2). The N1098Q presented a more complicated picture. In the absence of Mg^{2+}, the N1098Q mutation reduced the average number of inter-subunit hydrogen bonds formed by N1097 and Q1098 to only 0.6 as opposed to 3.6 in the WT structure (Suppl. Table S6, Suppl. Figure 11B). These results suggest that the closed state of the N1098Q channel is significantly less stable than the WT channel. In the presence of Mg^{2+}, the N1098Q channel retained coordination with Mg^{2+}, but the glutamine residue at position 1098 interacted weaker with N1097 than the WT channel (Suppl. Table S6). Hence, consistent with electrophysiological data, N1097 and N1098 have distinct structural roles in the lower channel gate of TRPM7.

Discussion

There is growing evidence to show that TRPM7 is a central gatekeeper of the cellular uptake of essential divalent cations and that cytosolic Mg^{2+} acts as the principal regulator of this fundamental process. In the present paper, we used a combination of site-directed mutagenesis, electrophysiological techniques and MD simulations to show that side chains of N1097 in mouse TRPM7 form an inter-subunit Mg^{2+}-regulatory site, determining the responses of the channel to changes of cytosolic Mg^{2+} levels. Hence, our study offers a molecular explanation of the key regulatory characteristic of the TRPM7 channel. The primary role of the lower channel gate in sensing the intracellular milieu has not been described yet in TRPM channels. Whether such a mechanism epitomizes a general principle among other TRP channels remains to be answered in the future.

The current view is that intracellular Mg^{2+} and Mg·ATP represent physiologically relevant negative regulators of the channel. Because TRPM7 contains a kinase unit, initial studies attempted to address the regulatory role of this domain [13–15, 21]. However, a kinase-dead point mutation (K1646R in mouse TRPM7) or channel variants lacking the C-terminal segments of the channel, including the kinase moiety, resulted in channels with only modestly changed sensitivity to Mg^{2+} [13–15, 21]. In contrast, the effects of Mg·ATP were dependent on the kinase moiety and upstream coiled-coil segments of TRPM7 in a species-specific fashion [13–15, 21]. These findings can be interpreted to mean that Mg^{2+} and Mg·ATP operate through different regulatory sites in TRPM7 and that Mg^{2+} blocks TRPM7 independently from the kinase domain.

In the present study, we uncovered the structural basis of the inhibitory action of free Mg^{2+} on the TRPM7 channel. Our hypothesis-driven assessment of TRPM7 variants with point mutations spanning different segments of TRPM7 suggests that the lower channel gate determines the Mg^{2+} sensitivity of TRPM7. Thus, a slight modification of the side chain of N1097 (N1097Q mutation) was sufficient to shift the IC_{50} value beyond physiological levels of free Mg^{2+}. Consequently, the N1097Q mutant was active in perforated patch-clamp recordings when the patch pipette solutions did not manipulate the intracellular Mg^{2+} levels. Interestingly, the N1097Q channel showed reduced sensitivity to free Ba^{2+}, implying that other divalent cations can potentially occupy the proposed Mg^{2+} binding site, thus, providing a mechanistic explanation for the inhibition of TRPM7 currents by Ba^{2+}, Ca^{2+} and Zn^{2+}

when applied in the mM range [38]. Significantly, N1097Q did not affect the current amplitudes of the channel in the absence of intracellular or extracellular Mg^{2+} and displayed unchanged I–V characteristics in all experimental settings used. The N1097Q mutant retained the sensitivity to pharmacological agents acting as negative and positive gating modulators of TRPM7, such as NS8593 and naltriben. Moreover, assessing the biophysical properties of the N1097Q mutant on the single-channel level corroborated our conclusion derived from whole-cell data, in that the mutant channel remains active in the presence of physiological concentrations of internal Mg^{2+}. Collectively, these results indicate that the N1097Q mutation selectively affects the inhibitory action of intracellular Mg^{2+} rather than perturbing TRPM7 function unspecifically.

Although the present study primarily aimed to reveal regulatory mechanisms of Mg^{2+}, our experiments also provide new insight into the action of PIP_2 and Mg·ATP on TRPM7. Thus, the N1097Q variant responded to PIP_2 depletion similarly to the WT channel. The latter finding is not surprising because the side chain of N1097 is exposed to the channel pore lumen and, consequently, incapable of interacting directly with membrane PIP_2. However, we observed that the N1097Q channel was sensitive to unphysiologically high Mg^{2+} concentrations suggesting that an additional action of Mg^{2+} was retained, for instance, the predicted electrostatic Mg^{2+} shielding of negatively charged PIP_2 [20–22]. Also, we observed that in the presence of relatively low Mg^{2+} levels (250 and 550 µM), the N1097Q variant exhibited a significantly reduced sensitivity to Mg·ATP (and Mg·GTP). However, the inhibitory effect of Mg·ATP on N1097Q currents was retained in the presence of 1 mM free Mg^{2+}. These results are consistent with a previous study [13], demonstrating that free Mg^{2+} and Mg·ATP can interact with TRPM7 causing the synergistic inhibition of TRPM7 currents. Accordingly, we suggest that the N1097Q mutation primarily affects the channel's response to free Mg^{2+}, while its sensitivity to Mg·ATP is still preserved.

MD simulations allowed us to interrogate the structural role of N1097 in opening of the TRPM7 channel. Our data suggest that the four side chains of N1097 in a TRPM7 tetramer form an inter-subunit cation-binding site and that the presence of Mg^{2+} in this pocket stabilizes the closed channel state. Accordingly, the lack of Mg^{2+} facilitates channel opening. In line with electrophysiological experiments, the N1097Q variant eradicates the coordination of Mg^{2+} in the lower channel gate due to the difference of one methylene group in the length of side chains of asparagine and glutamine, thus destabilizing the closed channel state in the presence of Mg^{2+}. Unlike N1097Q, a similar modification of an adjacent asparagine, N1098Q, resulted in a gain-of-function mutation completely offsetting the effects of Mg^{2+}, Ba^{2+}, Mg·ATP, Mg·GTP, PIP_2 and pharmacological agents. Such constitutive activity of the N1098Q channel resembles a previously isolated TRPM7 variant containing the point mutation S1107E in the TRP domain [42]. The S1107E channel was insensitive to physiological levels of free Mg^{2+}, PIP_2 and naltriben [42].

The structural role of N1098 is distinguishable from that of N1097. MD simulations suggest that N1098 forms inter-subunit hydrogen bonds stabilizing the closed state of the WT channel. Consequently, the N1098Q mutation most likely destabilizes such hydrogen bonds resulting in a constitutively active channel variant. The striking functional impact of N1098Q and the closely located S1107E further reinforce the notion that this segment of TRPM7 plays a crucial role in opening of the channel.

Previously, our structure–functional analysis of mouse TRPM7 identified the crucial role of E1047 in the cation selectivity filter of the channel [48]. Together with other researchers [23, 48, 49], we showed that the E1047Q variant of TRPM7 was essentially impermeable to divalent cations, supporting the idea that the side chain of E1047 forms an inter-subunit site that directly interacts with divalent cations entering the channel pore. To this end, the structural impact of E1047 in the cation selectivity filter resembles the role of N1097 in the lower channel gate of TRPM7, implying the channel function of TRPM7 primarily operates using two inter-subunit cation-binding sites interacting with extracellular and cytosolic divalent cations. Since N1097 and N1098 of mouse TRPM7 are conserved within the TRPM1/3/6/7 group of mammalian proteins (Fig. 1G), such a structure–function paradigm may be relevant for this subgroup of TRPM channels as a general principle.

Material and methods

Molecular biology and cell culture

Mouse TRPM7 (in pIRES2-EGFP vector) and TRPM7-YFP (in pcDNA3.1/V5-His TA-TOPO vector) were reported previously [36, 37]. Ci-VSP or Ci-VSP-C363S cDNAs (in pIRES2-EGFP) were provided by Joris Vriens, KU Leuven [50].

Point mutations in TRPM7 were introduced using the QuikChange system (Thermo Fisher Scientific) according to the manufacturer's protocol and verified by sequencing (Eurofins, Germany). Initially, we attempted to introduce the mutations outlined in Fig. 1A in the mouse TRPM7 cDNA in the bicistronic pIRES2-EGFP vector [36, 37]. However, we found that side-directed mutagenesis of this expression construct is highly inefficient and prone to errors likely due to cis-acting IRES sequence. Nevertheless, we could successfully conduct mutagenesis using the mouse TRPM7

with C-terminal YFP tag in pcDNA3.1 vector [36, 37] and, consequently, the primary functional assessment of TRPM7 variants (Fig. 1) was performed using the latter expression construct.

HEK293T cells were grown at 37 °C and 5% CO_2 in Dulbecco's modified Eagle's medium (DMEM, Sigma-Aldrich) supplemented with 10% foetal bovine serum (FBS, Thermo Fisher Scientific), 100 U/ml penicillin and 100 µg/ml streptomycin (P/S, Sigma-Aldrich). Cells ~60% confluence, 3 cm dish) were transiently transfected by 2 µg TRPM7 cDNAs using Lipofectamine 2000 reagent (Thermo Fisher Scientific). In some experiments, 2 µg TRPM7 cDNAs (pIRES2-EGFP) were co-transfected with 1 µg Ci-VSP WT or Ci-VSP-C363S cDNAs (pIRES2-EGFP) as indicated in the corresponding figure legend.

Immunofluorescent staining

HEK293T cells cultured on glass-bottom cell culture dishes (World Precision Instruments) were transiently transfected by 2 µg/dish WT or mutant variants of TRPM7 cDNA (in pIRES2-EGFP) and examined 18–24 h after transfection. Cells were washed twice with PBS, fixed with ice-cold methanol for 20 min at − 20 °C, and blocked for 1 h with 5% (v/v) BSA in PBS at room temperature. The mouse monoclonal anti-TRPM7 antibody (clone 2C7; 0.84 µg/ml; [51]) was applied. The secondary antibody (0.5 µg/ml) was goat anti-mouse IgG conjugated to Alexa Fluor 488 (Molecular Probes). Each incubation was performed in PBS containing 5% (v/v) normal goat serum for 1 h at room temperature, followed by triple washing with PBS. After the final washing, glass coverslips were placed on glass-bottom cell culture dishes using a mounting medium (DakoCytomation). Differential interference contrast (DIC) and Airyscan images of Alexa Fluor 488 were obtained with the confocal laser-scanning microscope LSM 880 AxioObserver (Carl Zeiss). We used a C-Apochromat 63x/1.2 W objective, 488 nm excitation wavelength and 493–630 nm filters, multi-line argon laser 458/488/514 nm and an Airyscan detector. The acquired images were analysed using the ZEN 3.0 SR software (Carl Zeiss).

Electrophysiological techniques

Patch-clamp experiments with HEK293T cells were performed 18–22 h after transfection as reported previously [37, 52] with a few modifications. Whole-cell currents were measured using an EPC10 patch-clamp amplifier and PatchMaster software (Harvard Bioscience). Voltages were corrected for a liquid junction potential of 10 mV. Currents were elicited by a ramp protocol from − 100 mV to + 100 mV over 50 ms acquired at 0.5 Hz and a holding potential of 0 mV. Inward and outward current amplitudes were extracted at − 80 mV and + 80 mV and were normalized to cell size as pA/pF. Capacitance was measured using the automated capacitance cancellation function of EPC10. Patch pipettes were made of borosilicate glass (Science Products) and had resistance 2–3.5 MΩ.

Unless stated otherwise, a standard extracellular solution contained (in mM): 140 NaCl, 2.8 KCl, 1 $CaCl_2$, 2 $MgCl_2$, 10 HEPES–NaOH and 11 glucose (all from Roth Industries), pH 7.2. Effects of NS8593 (Tocris) and naltriben (Tocris) were examined by adding the compounds to the standard extracellular solution. A divalent cation-free (DVF) extracellular solution contained (in mM) 140 NaCl, 2.8 KCl, 11 glucose, 10 Na-EDTA and 10 HEPES–NaOH, pH 7.2. For the experiment with TRPM7-YFP (Fig. 1), we used an extracellular solution contained (in mM): 140 NaCl, 2.8 KCl, 1 $CaCl_2$, 10 HEPES–NaOH, and 11 glucose (all from Roth Industries), pH 7.2. The standard Mg^{2+}-free intracellular ($[Mg^{2+}]_i$) pipette solution containing (in mM): 120 Cs·glutamate, 8 NaCl, 10 Cs-EGTA, 5 Cs-EDTA, 10 HEPES–CsOH, pH 7.2.

To obtain $[Mg^{2+}]_i$ and $[Mg{\cdot}ATP]_i$ concentration–response data, the intracellular pipette solutions were prepared as outlined in Suppl. Tables S1–S4. Concentrations of $[Mg{\cdot}ATP]_i$ and free $[Mg^{2+}]_i$ were calculated using the Maxchelator software (maxchelator.stanford.edu).

The concentration–response data were fitted (Prism 8.4.0) with the following equation:

$$E(c) = E_{\min} + (E_{\max} - E_{\min}) \times (1/(1 + (IC_{50}/c)^h)),$$

with E being the effect/current at a given concentration c of inhibitor; $E_{\min}$, the minimal effect/current; E_{max}, the maximal effect; IC_{50}, the half-maximal concentration; h, the Hill factor.

For perforated patch recordings, 320 µM amphotericin B (Sigma-Aldrich) was added to the internal solution containing (in mM): 120 monopotassium glutamate (Sigma-Aldrich), 8 NaCl, 1 $MgCl_2$, 10 HEPES–KOH, pH 7.2. Cells were held at − 60 mV for 2 min to ensure activation of TRPM7 currents, followed by the standard voltage ramp protocol.

Outside-out patch-clamp recordings with EGFP-positive HEK293 cells were performed the day after transfection with either the WT or the N1097Q mutant of TRPM7, using procedures described previously [45]. The standard extracellular solution contained in these experiments (in mM): 147 NaCl, 2 KCl, 1 $MgCl_2$, 2 $CaCl_2$, 13 D-glucose and 10 HEPES (~305 mOsm/l; pH 7.3 with NaOH). A divalent cation-free (no-DIV) solution was produced by omitting Ca^{2+} and Mg^{2+} and supplementing EGTA and EDTA (1 mM each). Patch pipettes had a resistance of 15–20 MΩ when filled with intracellular solutions. These were either identical with the

no-DIV saline or based on it but containing about 1 mM of free Mg^{2+} in addition (2.07 mM added $MgCl_2$). Baselines in the current traces were corrected and raw single-channel data was evaluated with the QuB program. The mean amplitudes (i) of TRPM7 single-channel currents (digitized at 20 kHz and filtered at 2 kHz) were thereby from all-points amplitude histograms fitted to a sum of multiple Gaussian distributions, with the number of components depending on the apparent number of active channels (N) in a given patch. The probability for N channels being open (NP_O) was, in turn, defined as the ratio of the area occupied by all the peaks for open channels to the total amplitude histogram (summation of the open and closed peaks). The unitary conductance (γ) of WT or mutant TRPM7 channels was either calculated from i as chord conductance (γ_c), assuming a reversal potential of zero mV or, for comparison, in some experiments also derived from the slope of respective current–voltage relationships (γ_s, slope conductance). In multichannel patches, like those usually obtained during this study, uncertainties concerning the "true" value of N, as well as the overlap of channel openings, precludes a detailed dwell time analysis.

To still allow for comparisons, such as between WT and N1097Q channels, the relation [53]:

$$T_{os} = \left(\sum_i L_i \, t_i \right) / \, \#O,$$

where t_i is the total time the outside-out currents dwelt on level L_i during the recording and $\#O$ is the total of the number of opening events, was used to estimate a surrogate mean open time (T_{OS}). To this end, channel openings were counted over a prolonged time (4 min) in the outside-out current recordings, using the 50% amplitude threshold criterion implemented in QuB. The dead time imposed was 200 µs (~1.2-fold of the filter rise time), thus excluding shorter events than this from the analysis.

Data are presented as means ± standard error of the mean (means ± SEM). Statistical comparisons (Prism 8.4.0 or SigmaPlot 14.0) were made using analysis of variance (ordinary one-way ANOVA) or two-tailed t test, as indicated in the figure legends. Significance was accepted at $P \leq 0.05$.

MD simulations

All MD simulations were carried out using the pmemd.cuda program of AMBER16 molecular dynamics package [54]. The Amber FF99SB–ILDN force field [55] for proteins was used for all simulations combined with Lipid14 model [56] for lipids and TIP3P model for water. All covalent bonds involving hydrogen atoms were constrained using SHAKE [57] to allow an integration time step of 2 fs. Langevin thermostat and Berendsen barostat were used to control temperature and pressure, respectively. All NPT simulations were carried out using anisotropic pressure scaling. Electrostatic interactions were calculated using particle mesh ewald (PME) method [58] as implemented in Amber, with a non-bonded cutoff distance of 8 Å. Periodic boundary conditions were applied in all directions. In order to maintain the integrity of the pore loop of the protein, backbone hydrogen bond distances in the pore helix (residues 1031–1043) were restrained between 2.6 Å and the initial value during all simulations. Post-processing of trajectories was carried out using CPPTRAJ [59] and VMD [60].

MD simulation setup

Residues 982–1123 (S4-S5 linker, S5 helix, pore loop, S6 helix, and TRP helix) of the cryo-EM structure of the closed TRPM7 channel (PDB: 5ZX5) was used as the starting structure for all simulations. The protein was embedded in a POPC lipid membrane and solvated in water using the CHARMM-GUI Membrane Builder [61]. Additional water molecules were added manually to solvate the ion channel pore. The system was prepared for simulations using the charmmlipid2amber.py script and the tleap program in AmberTools16 (www.ambermd.org). The protein N and C termini were capped with the neutral acetyl and amide groups, and the conserved disulfide bond between residues C1056 and C1066 was introduced. The system was neutralized with Na^+ and Cl^- ions. The final system contained 568 protein residues, 159 lipid molecules, 13,585 water molecules and neutralizing ions.

MD simulations of the closed TRPM7 channel

The prepared TRPM7 closed channel system was equilibrated as follows. First, a short minimization (6000 steps) was performed to remove clashes in the system. The system was then heated from 0.1 to 100 K in NVT ensemble and 100 K to 300 K in NPT ensemble, over 250 ps. The protein heavy atoms were restrained at their initial positions with a harmonic force constant (k) of 10 kcal mol^{-1} $Å^{-2}$ during the heating steps (residues 1050–1070 in the pore loop were not restrained in order to enforce the disulphide bond between C1056 and C1066). The system was equilibrated at 300 K in NPT ensemble for 35 ns while gradually decreasing restraints on the protein until only the C_α atoms were restrained with $k = 0.5$ kcal mol^{-1} $Å^{-2}$. The resulting system was used as the starting structure for the simulations with Mg^{2+} and N1097 mutant simulations (described in the following sections). All restraints on protein C_α atoms were removed except those on residues 1116–1123 of the TRP helix, and the closed channel was equilibrated in NPT ensemble for further 100 ns.

TRPM7 open channel conformation model

The S5, S6, and TRP helices and the S4–S5 linker (residues 982–1022 and 1071–1123) of the TRPM7 open channel were modelled in SWISS-MODEL [62] using the open channel structure of human TRPV6 channel (PDB ID: 6BO8) as a template. The target–template alignment for homology modelling was extracted from a multiple sequence alignment of the transmembrane and TRP regions of known TRPM and TRPV structures (TRPM7, TRPM4, TRPM2, TRPV1, TRPV3, TRPV6) performed using Clustal Omega at EMBL-EBI [63]. Residues 471–513 and 553–605 of PDB: 6BO8 was used to model the open structure of TRPM7.

MD simulations of the open channel

The homology model of the open TRPM7 channel was used to open the equilibrated closed channel by targeted MD simulations with simulated annealing. To open the channel, the C_α atoms of residues 982–1022 and 1071–1123 (S4–S5 and S5 helix, S6 and TRP helices) in the closed channel were harmonically restrained to the corresponding coordinates of the open homology model. Simulated annealing was performed in six steps as follows. In each step, (a) the system was equilibrated for 5 ns at 300 K, (b) heated to 350 K over 500 ps, (c) equilibrated at 350 K for 5 ns (or until RMSD of the targeted C_α atoms with respect to the reference structure was stable), and (d) cooled back to 300 K over 500 ps. Harmonic restraints were maintained throughout the process, increasing the force constant at the end of each step from 0.05, 0.1, 0.2, 1.0, 2.0 to 2.5 kcal mol^{-1} Å^{-2}. The restraints were then released gradually over a period of 25 ns and, finally, unrestrained simulations of the open model were carried out for over 200 ns.

MD simulations of the mutant TRPM7 variants

The partially equilibrated closed TRPM7 channel (see "MD simulations of the closed TRPM7 channel" section) was used to construct the mutants N1097Q, N1097A and N1098Q. Additionally, Mg^{2+} was placed between the residues at the 1097 position to obtain complexes of the wild type (WT-MG), and the N1097Q (N1097Q-MG) and N1098Q (N1098Q-MG) mutants with Mg^{2+}. The charge on Mg^{2+} was set to + 1.65. Each system was equilibrated using a protocol similar to that described in the previous section (MD simulations of the closed TRPM7 channel), except restraints on the protein C_α atoms were changed from $k = 10$ to 0.5 kcal mol^{-1} Å^{-2} in 20 ns. In WT-MG, N1097Q-MG and N1098Q-MG systems, the magnesium ion was restrained with the same force constant used to restrain the protein, and an additional equilibration step of 100 ns was carried out without restraints on the magnesium ion while maintaining restraints on the protein C_α atoms at $k = 0.5$ kcal mol^{-1} Å^{-2}. All systems were simulated for 100 ns with all restraints removed except the restraints on C_α atoms of residues 1116–1123.

Supplementary Information The online version contains supplementary material available at https://doi.org/10.1007/s00018-022-04192-7.

Acknowledgements We thank the Extreme Science and Engineering Discovery Environment (XSEDE) at the Pittsburgh Supercomputing Center for technical support (allocation TG-MCB180173). We thank Joanna Zaisserer, Lisa Pleninger and Anna Erbacher for their technical assistance.

Authors' contributions All authors read and approved the final manuscript. All authors contributed to the study conception and design as follows: conceptualization: VC, TG, MGK; funding acquisition, VC, TG, MGK, MS; experimental investigation, ES, CN, WN, ME, AR, ML; theoretical investigation, CN, MGK; formal analysis, SZ, MS, CN, MGK; writing—original draft preparation VC, TG, MGK; writing—review and editing, MS, SZ, WN, VC, TG.

Funding Open Access funding enabled and organized by Projekt DEAL. VC, MS, SZ and TG were supported by the Deutsche Forschungsgemeinschaft, TRR 152. TG was supported by Research Training Group 2338 (DFG). CN and MK were supported by grants from NSF 1818213, NSF 1563291, and NIH RO1NS083660.

Availability of data and materials All reagents and data generated or analysed during this study and its supplementary information files are available from the corresponding authors on request.

Declarations

Conflict of interests The authors declare that they have no conflict of interests.

Consent for publication Not applicable.

Ethics approval and consent to participate Not applicable.

References

1. Chubanov V, Mittermeier L, Gudermann T (2018) Role of kinase-coupled TRP channels in mineral homeostasis. Pharmacol Ther 184:159–176

2. Fleig A, Chubanov V (2014) Trpm7. Handb Exp Pharmacol 222:521–546
3. Bates-Withers C, Sah R, Clapham DE (2011) TRPM7, the Mg(2+) inhibited channel and kinase. Adv Exp Med Biol 704:173–183
4. Mittermeier L et al (2019) TRPM7 is the central gatekeeper of intestinal mineral absorption essential for postnatal survival. Proc Natl Acad Sci U S A 116(10):4706–4715
5. Schmitz C et al (2003) Regulation of vertebrate cellular Mg^{2+} homeostasis by TRPM7. Cell 114(2):191–200
6. Abiria SA et al (2017) TRPM7 senses oxidative stress to release Zn(2+) from unique intracellular vesicles. Proc Natl Acad Sci USA 114(30):E6079–E6088
7. Monteilh-Zoller MK et al (2003) TRPM7 provides an ion channel mechanism for cellular entry of trace metal ions. J Gen Physiol 121(1):49–60
8. Faouzi M et al (2017) The TRPM7 channel kinase regulates store-operated calcium entry. J Physiol 595(10):3165–3180
9. Kerschbaum HH, Cahalan MD (1999) Single-channel recording of a store-operated Ca^{2+} channel in Jurkat T lymphocytes. Science 283(5403):836–839
10. Prakriya M, Lewis RS (2002) Separation and characterization of currents through store-operated CRAC channels and Mg^{2+}-inhibited cation (MIC) channels. J Gen Physiol 119(5):487–507
11. Kozak JA, Kerschbaum HH, Cahalan MD (2002) Distinct properties of CRAC and MIC channels in RBL cells. J Gen Physiol 120(2):221–235
12. Nadler MJ et al (2001) LTRPC7 is a Mg·ATP-regulated divalent cation channel required for cell viability. Nature 411(6837):590–595
13. Demeuse P, Penner R, Fleig A (2006) TRPM7 channel is regulated by magnesium nucleotides via its kinase domain. J Gen Physiol 127(4):421–434
14. Matsushita M et al (2005) Channel function is dissociated from the intrinsic kinase activity and autophosphorylation of TRPM7/ChaK1. J Biol Chem 280(21):20793–20803
15. Jansen C et al (2016) The coiled-coil domain of zebrafish TRPM7 regulates Mg. nucleotide sensitivity. Sci Rep 6:33459
16. Ryazanova LV et al (2010) TRPM7 is essential for Mg(2+) homeostasis in mammals. Nat Commun 1:109
17. Ryazanova LV et al (2014) Elucidating the role of the TRPM7 alpha-kinase: TRPM7 kinase inactivation leads to magnesium deprivation resistance phenotype in mice. Sci Rep 4:7599
18. Kaitsuka T et al (2014) Inactivation of TRPM7 kinase activity does not impair its channel function in mice. Sci Rep 4:5718
19. Hermosura MC et al (2005) A TRPM7 variant shows altered sensitivity to magnesium that may contribute to the pathogenesis of two Guamanian neurodegenerative disorders. Proc Natl Acad Sci U S A 102(32):11510–11515
20. Runnels LW, Yue L, Clapham DE (2002) The TRPM7 channel is inactivated by PIP(2) hydrolysis. Nat Cell Biol 4(5):329–336
21. Kozak JA et al (2005) Charge screening by internal pH and polyvalent cations as a mechanism for activation, inhibition, and rundown of TRPM7/MIC channels. J Gen Physiol 126(5):499–514
22. Xie J et al (2011) Phosphatidylinositol 4,5-bisphosphate (PIP(2)) controls magnesium gatekeeper TRPM6 activity. Sci Rep 1:146
23. Duan J et al (2018) Structure of the mammalian TRPM7, a magnesium channel required during embryonic development. Proc Natl Acad Sci U S A 115(35):E8201–E8210
24. Ruan Z et al (2021) Structures of the TRPM5 channel elucidate mechanisms of activation and inhibition. Nat Struct Mol Biol 28(7):604–613
25. Duan J et al (2018) Structure of full-length human TRPM4. Proc Natl Acad Sci U S A 115(10):2377–2382
26. Autzen HE et al (2018) Structure of the human TRPM4 ion channel in a lipid nanodisc. Science 359(6372):228–232
27. Winkler PA et al (2017) Electron cryo-microscopy structure of a human TRPM4 channel. Nature 552(7684):200–204
28. Guo J et al (2017) Structures of the calcium-activated, non-selective cation channel TRPM4. Nature 552(7684):205–209
29. Yin Y et al (2019) Structural basis of cooling agent and lipid sensing by the cold-activated TRPM8 channel. Science 363(6430):9334
30. Diver MM, Cheng Y, Julius D (2019) Structural insights into TRPM8 inhibition and desensitization. Science 365(6460):1434–1440
31. Huang Y et al (2019) Ligand recognition and gating mechanism through three ligand-binding sites of human TRPM2 channel. Elife 8:e50175
32. Huang Y et al (2018) Architecture of the TRPM2 channel and its activation mechanism by ADP-ribose and calcium. Nature 562(7725):145–149
33. Zhang Z et al (2018) Structure of a TRPM2 channel in complex with Ca(2+) explains unique gating regulation. Elife 7:e36409
34. Mesbahi-Vasey S et al (2017) All atom NMDA receptor transmembrane domain model development and simulations in lipid bilayers and water. PLoS ONE 12(6):e0177686
35. Payandeh J, Pfoh R, Pai EF (2013) The structure and regulation of magnesium selective ion channels. Biochim Biophys Acta 1828(11):2778–2792
36. Chubanov V et al (2004) Disruption of TRPM6/TRPM7 complex formation by a mutation in the TRPM6 gene causes hypomagnesemia with secondary hypocalcemia. Proc Natl Acad Sci U S A 101(9):2894–2899
37. Ferioli S et al (2017) TRPM6 and TRPM7 differentially contribute to the relief of heteromeric TRPM6/7 channels from inhibition by cytosolic Mg(2+) and Mg. ATP. Sci Rep 7(1):8806
38. Kozak JA, Cahalan MD (2003) MIC channels are inhibited by internal divalent cations but not ATP. Biophys J 84(2 Pt 1):922–927
39. Traut TW (1994) Physiological concentrations of purines and pyrimidines. Mol Cell Biochem 140(1):1–22
40. Gupta RK et al (1983) Measurement of the dissociation constant of MgATP at physiological nucleotide levels by a combination of 31P NMR and optical absorbance spectroscopy. Biochem Biophys Res Commun 117(1):210–216
41. Romani AM (2011) Cellular magnesium homeostasis. Arch Biochem Biophys 512(1):1–23
42. Hofmann T et al (2014) Activation of TRPM7 channels by small molecules under physiological conditions. Pflugers Arch 466(12):2177–2189
43. Chubanov V et al (2012) Natural and synthetic modulators of SK (K (ca)2) potassium channels inhibit magnesium-dependent activity of the kinase-coupled cation channel TRPM7. Br J Pharmacol 166(4):1357–1376
44. Murata Y et al (2005) Phosphoinositide phosphatase activity coupled to an intrinsic voltage sensor. Nature 435(7046):1239–1243
45. Norenberg W et al (2016) TRPM7 is a molecular substrate of ATP-evoked P2X7-like currents in tumor cells. J Gen Physiol 147(6):467–483
46. Chokshi R, Matsushita M, Kozak JA (2012) Sensitivity of TRPM7 channels to Mg^{2+} characterized in cell-free patches of Jurkat T lymphocytes. Am J Physiol Cell Physiol 302(11):C1642–C1651
47. McGoldrick LL et al (2018) Opening of the human epithelial calcium channel TRPV6. Nature 553(7687):233–237
48. Mederos y Schnitzler M et al (2008) Evolutionary determinants of divergent calcium selectivity of TRPM channels. FASEB J 22(5):1540–1551

49. Li M et al (2007) Molecular determinants of Mg^{2+} and Ca^{2+} permeability and pH sensitivity in TRPM6 and TRPM7. J Biol Chem 282(35):25817–25830
50. Toth BI et al (2015) Regulation of the transient receptor potential channel TRPM3 by phosphoinositides. J Gen Physiol 146(1):51–63
51. Kollewe A et al (2021) The molecular appearance of native TRPM7 channel complexes identified by high-resolution proteomics. Elife 10:e68544
52. Chubanov V et al (2016) Epithelial magnesium transport by TRPM6 is essential for prenatal development and adult survival. Elife 5:e20914
53. Nemec J, Wickman K, Clapham DE (1999) Gbetagamma binding increases the open time of IKACh: kinetic evidence for multiple Gbetagamma binding sites. Biophys J 76(1 Pt 1):246–252
54. Case DA et al (2005) The Amber biomolecular simulation programs. J Comput Chem 26(16):1668–1688
55. Lindorff-Larsen K et al (2010) Improved side-chain torsion potentials for the Amber ff99SB protein force field. Proteins 78(8):1950–1958
56. Dickson CJ et al (2014) Lipid14: the amber lipid force field. J Chem Theory Comput 10(2):865–879
57. Hauptman HA (1997) Shake-and-bake: an algorithm for automatic solution ab initio of crystal structures. Methods Enzymol 277:3–13
58. Darden T et al (1999) New tricks for modelers from the crystallography toolkit: the particle mesh Ewald algorithm and its use in nucleic acid simulations. Structure 7(3):R55-60
59. Roe DR, Cheatham TE 3rd (2013) PTRAJ and CPPTRAJ: software for processing and analysis of molecular dynamics trajectory data. J Chem Theory Comput 9(7):3084–3095
60. Humphrey W, Dalke A, Schulten K (1996) VMD: visual molecular dynamics. J Mol Graph 14(1):33–38
61. Jo S, Kim T, Im W (2007) Automated builder and database of protein/membrane complexes for molecular dynamics simulations. PLoS ONE 2(9):e880
62. Waterhouse A et al (2018) SWISS-MODEL: homology modelling of protein structures and complexes. Nucleic Acids Res 46(W1):W296–W303
63. Madeira F et al (2019) The EMBL-EBI search and sequence analysis tools APIs in 2019. Nucleic Acids Res 47(W1):W636–W641

Supplementary information for publication II

Here I only included supplementary figures which were produced by me.

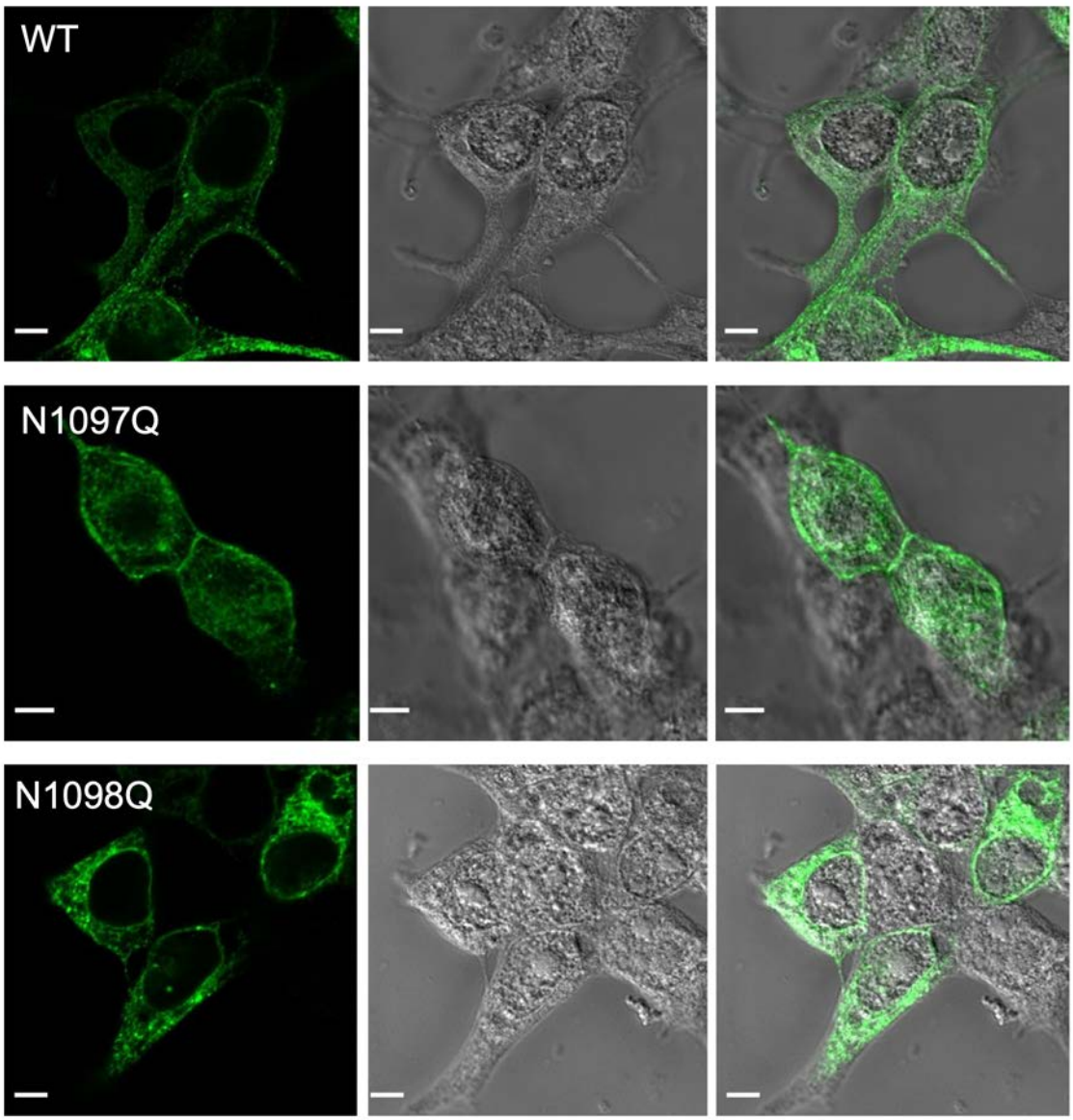

Suppl. Figure S2. Subcellular localization of TRPM7 in HEK293T cells.

Mouse TRPM7 variants were transiently expressed in the indicated TRPM7 cDNA plasmid variants in HEK293T cells and immunolocalized using anti-TRPM7 and anti-mouse IgG-Alexa Fluor 488 antibodies. Representative confocal images of Alexa Fluor 488 fluorescence (Left panels) and their overlay with corresponding DIC images (Middle and Right panels) are shown. Scale bars are 5 μm.

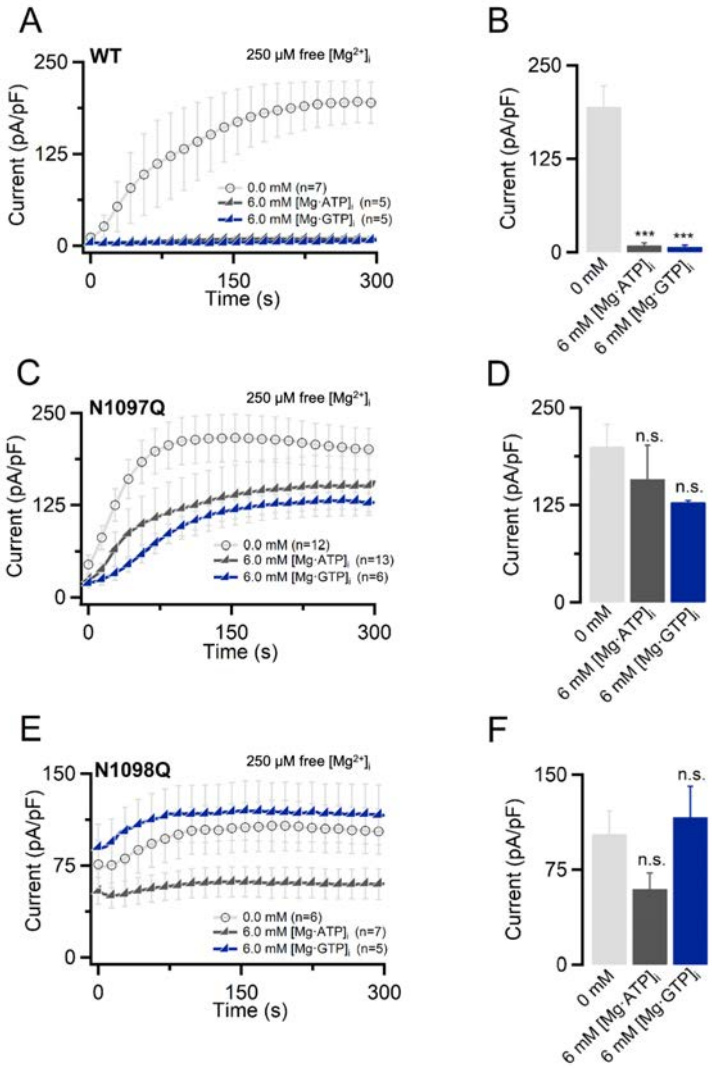

Suppl. Figure S4. Inhibition of TRPM7 currents by cytosolic Mg·ATP and Mg·GTP. Whole-cell currents were measured in HEK293T cells transfected by WT (**A**, **B**), N1097Q (**C**, **D**) and N1098Q (**E**, **F**) variants of TRPM7 cDNAs (in pIRES2-EGFP). A, C, D Current amplitudes (mean ± SEM) were measured at +80 mV and plotted over time. Currents were measured using an intracellular solution containing 250 µM free $[Mg^{2+}]_I$ without Mg·nucleotides, 250 µM free $[Mg^{2+}]_i$ with 6 mM $[Mg{\cdot}ATP]_i$, and 250 µM free $[Mg^{2+}]_i$ with 6 mM $[Mg{\cdot}GTP]_i$ (Suppl. Table S3). B, D, F Bar graphs of outward currents (+80 mV, mean ± SEM) obtained at 300 s as indicated in (A, B, C). Note: The results obtained with 250 µM free $[Mg^{2+}]_i$ without Mg·nucleotides and with 6 mM $[Mg{\cdot}ATP]_i$ were taken from Fig. 3. n, number of cells measured; n.s., not significant; ****P*< 0.001 (ANOVA)

7. References

[1] M. Egawa, E. Schmücker, C. Grimm, T. Gudermann, and V. Chubanov, "Expression Profiling Identified TRPM7 and HER2 as Potential Targets for the Combined Treatment of Cancer Cells," *Cells,* vol. 13, no. 21, p. 1801, 2024.

[2] E. Schmidt *et al.*, "Structural mechanism of TRPM7 channel regulation by intracellular magnesium," (in eng), *Cell Mol Life Sci,* vol. 79, no. 5, p. 225, Apr 7 2022, doi: 10.1007/s00018-022-04192-7.

[3] S. A. Abiria *et al.*, "TRPM7 senses oxidative stress to release Zn^{2+} from unique intracellular vesicles," *Proceedings of the National Academy of Sciences,* vol. 114, no. 30, pp. E6079-E6088, 2017.

[4] M. Faouzi, T. Kilch, F. D. Horgen, A. Fleig, and R. Penner, "The TRPM7 channel kinase regulates store-operated calcium entry," *The Journal of physiology,* vol. 595, no. 10, pp. 3165-3180, 2017.

[5] L. Mittermeier *et al.*, "TRPM7 is the central gatekeeper of intestinal mineral absorption essential for postnatal survival," *Proceedings of the National Academy of Sciences,* vol. 116, no. 10, pp. 4706-4715, 2019.

[6] M. K. Monteilh-Zoller, M. C. Hermosura, M. J. Nadler, A. M. Scharenberg, R. Penner, and A. Fleig, "TRPM7 provides an ion channel mechanism for cellular entry of trace metal ions," *The Journal of general physiology,* vol. 121, no. 1, pp. 49-60, 2003.

[7] C. Schmitz *et al.*, "Regulation of vertebrate cellular Mg^{2+} homeostasis by TRPM7," *Cell,* vol. 114, no. 2, pp. 191-200, 2003.

[8] V. Chubanov, L. Mittermeier, and T. Gudermann, "Role of kinase-coupled TRP channels in mineral homeostasis," *Pharmacology & Therapeutics,* vol. 184, pp. 159-176, 2018.

[9] A. Fleig and V. Chubanov, "Trpm7," *Mammalian transient receptor potential (TRP) cation channels,* pp. 521-546, 2014.

[10] C. Bates-Withers, R. Sah, and D. E. Clapham, "TRPM7, the Mg^{2+} inhibited channel and kinase," *Transient Receptor Potential Channels,* pp. 173-183, 2011.

[11] P. Demeuse, R. Penner, and A. Fleig, "TRPM7 channel is regulated by magnesium nucleotides via its kinase domain," *The Journal of general physiology,* vol. 127, no. 4, pp. 421-434, 2006.

[12] M. J. Nadler *et al.*, "LTRPC7 is a Mg·ATP-regulated divalent cation channel required for cell viability," *Nature,* vol. 411, no. 6837, pp. 590-595, 2001.

[13] J. Duan *et al.*, "Structure of the mammalian TRPM7, a magnesium channel required during embryonic development," *Proceedings of the National Academy of Sciences,* vol. 115, no. 35, pp. E8201-E8210, 2018.

[14] L.-J. Wu, T.-B. Sweet, and D. E. Clapham, "International Union of Basic and Clinical Pharmacology. LXXVI. Current progress in the mammalian TRP ion channel family," *Pharmacological reviews,* vol. 62, no. 3, pp. 381-404, 2010.

[15] J. Middelbeek, K. Clark, H. Venselaar, M. A. Huynen, and F. N. Van Leeuwen, "The alpha-kinase family: an exceptional branch on the protein kinase tree," *Cellular and molecular life sciences,* vol. 67, no. 6, pp. 875-890, 2010.

[16] L. W. Runnels, L. Yue, and D. E. Clapham, "TRP-PLIK, a bifunctional protein with kinase and ion channel activities," *Science,* vol. 291, no. 5506, pp. 1043-1047, 2001.

[17] T. Voets *et al.*, "TRPM6 forms the Mg^{2+} influx channel involved in intestinal and renal Mg^{2+} absorption," *Journal of Biological Chemistry,* vol. 279, no. 1, pp. 19-25, 2004.

[18] R. Y. Walder *et al.*, "Mutation of TRPM6 causes familial hypomagnesemia with secondary hypocalcemia," *Nature genetics,* vol. 31, no. 2, pp. 171-174, 2002.

[19] E. Fonfria, P. R. Murdock, F. S. Cusdin, C. D. Benham, R. E. Kelsell, and S. McNulty, "Tissue distribution profiles of the human TRPM cation channel family," *Journal of Receptors and Signal Transduction,* vol. 26, no. 3, pp. 159-178, 2006.

[20] C. Kunert-Keil, F. Bisping, J. Krüger, and H. Brinkmeier, "Tissue-specific expression of TRP channel genes in the mouse and its variation in three different mouse strains," *BMC genomics,* vol. 7, no. 1, pp. 1-14, 2006.

[21] L. W Runnels, "TRPM6 and TRPM7: A Mul-TRP-PLIK-cation of channel functions," *Current pharmaceutical biotechnology,* vol. 12, no. 1, pp. 42-53, 2011.

[22] R. Penner and A. Fleig, "The Mg^{2+} and Mg^{2+}-nucleotide-regulated channel-kinase TRPM7," *Transient Receptor Potential (TRP) Channels,* pp. 313-328, 2007.

[23] S. Brauchi, G. Krapivinsky, L. Krapivinsky, and D. E. Clapham, "TRPM7 facilitates cholinergic vesicle fusion with the plasma membrane," *Proceedings of the National Academy of Sciences,* vol. 105, no. 24, pp. 8304-8308, 2008.

[24] M. L. Bernhardt, E. Padilla-Banks, P. Stein, Y. Zhang, and C. J. Williams, "Store-operated Ca^{2+} entry is not required for fertilization-induced Ca^{2+} signaling in mouse eggs," *Cell Calcium,* vol. 65, pp. 63-72, 2017.

[25] I. Carvacho, G. Ardestani, H. C. Lee, K. McGarvey, R. A. Fissore, and K. Lykke-Hartmann, "TRPM7-like channels are functionally expressed in oocytes and modulate post-fertilization embryo development in mouse," *Scientific reports,* vol. 6, no. 1, pp. 1-12, 2016.

[26] C. Schmitz, F. Deason, and A.-L. Perraud, "Molecular components of vertebrate Mg^{2+}-homeostasis regulation," *Magnesium research,* vol. 20, no. 1, pp. 6-18, 2007.

[27] L. W. Runnels, L. Yue, and D. E. Clapham, "The TRPM7 channel is inactivated by PIP_2 hydrolysis," *Nature cell biology,* vol. 4, no. 5, pp. 329-336, 2002.

[28] J. Jiang, M. Li, and L. Yue, "Potentiation of TRPM7 inward currents by protons," *The Journal of general physiology,* vol. 126, no. 2, pp. 137-150, 2005.

[29] T.-J. Kim *et al.*, "Distinct mechanisms regulating mechanical force-induced Ca^{2+} signals at the plasma membrane and the ER in human MSCs," *Elife,* vol. 4, p. e04876, 2015.

[30] Y.-S. Liu *et al.*, "Mechanosensitive TRPM7 mediates shear stress and modulates osteogenic differentiation of mesenchymal stromal cells through Osterix pathway," *Scientific reports,* vol. 5, no. 1, pp. 1-13, 2015.

[31] T. Numata, T. Shimizu, and Y. Okada, "Direct mechano-stress sensitivity of TRPM7 channel," *Cellular Physiology and Biochemistry,* vol. 19, no. 1-4, pp. 1-8, 2007.

[32] E. Oancea, J. T. Wolfe, and D. E. Clapham, "Functional TRPM7 channels accumulate at the plasma membrane in response to fluid flow," *Circulation research,* vol. 98, no. 2, pp. 245-253, 2006.

[33] E. Xiao *et al.*, "TRPM7 senses mechanical stimulation inducing osteogenesis in human bone marrow mesenchymal stem cells," *Stem cells,* vol. 33, no. 2, pp. 615-621, 2015.

[34] H. Yu, Z. Zhang, A. Lis, R. Penner, and A. Fleig, "TRPM7 is regulated by halides through its kinase domain," *Cellular and molecular life sciences,* vol. 70, no. 15, pp. 2757-2771, 2013.

[35] B. F. Bessac and A. Fleig, "TRPM7 channel is sensitive to osmotic gradients in human kidney cells," *The Journal of physiology,* vol. 582, no. 3, pp. 1073-1086, 2007.

[36] V. Chubanov *et al.*, "Natural and synthetic modulators of SK (Kca2) potassium channels inhibit magnesium-dependent activity of the kinase-coupled cation channel TRPM7," *British journal of pharmacology,* vol. 166, no. 4, pp. 1357-1376, 2012.

[37] T. Hofmann, S. Schäfer, M. Linseisen, L. Sytik, T. Gudermann, and V. Chubanov, "Activation of TRPM7 channels by small molecules under physiological conditions," *Pflügers Archiv-European Journal of Physiology,* vol. 466, no. 12, pp. 2177-2189, 2014.

[38] S. Zierler *et al.*, "Waixenicin A inhibits cell proliferation through magnesium-dependent block of transient receptor potential melastatin 7 (TRPM7) channels," *Journal of Biological Chemistry,* vol. 286, no. 45, pp. 39328-39335, 2011.

[39] X. Qin *et al.*, "Sphingosine and FTY720 are potent inhibitors of the transient receptor potential melastatin 7 (TRPM7) channels," *British journal of pharmacology,* vol. 168, no. 6, pp. 1294-1312, 2013.

[40] L. V. Ryazanova, M. V. Dorovkov, A. Ansari, and A. G. Ryazanov, "Characterization of the protein kinase activity of TRPM7/ChaK1, a protein kinase fused to the transient receptor potential ion channel," *Journal of Biological Chemistry,* vol. 279, no. 5, pp. 3708-3716, 2004.

[41] K. Brandao, F. Deason-Towne, X. Zhao, A.-L. Perraud, and C. Schmitz, "TRPM6 kinase activity regulates TRPM7 trafficking and inhibits cellular growth under hypomagnesic conditions," *Cellular and molecular life sciences,* vol. 71, no. 24, pp. 4853-4867, 2014.

[42] M. V. Dorovkov and A. G. Ryazanov, "Phosphorylation of annexin I by TRPM7 channel-kinase," *Journal of Biological Chemistry,* vol. 279, no. 49, pp. 50643-50646, 2004.

[43] K. Clark *et al.*, "TRPM7, a novel regulator of actomyosin contractility and cell adhesion," *The EMBO journal,* vol. 25, no. 2, pp. 290-301, 2006.

[44] A.-L. Perraud, X. Zhao, A. G. Ryazanov, and C. Schmitz, "The channel-kinase TRPM7 regulates phosphorylation of the translational factor eEF2 via eEF2-k," *Cellular signalling,* vol. 23, no. 3, pp. 586-593, 2011.

[45] F. Deason-Towne, A.-L. Perraud, and C. Schmitz, "Identification of Ser/Thr phosphorylation sites in the C2-domain of phospholipase C γ2 ($PLC_{\gamma}2$) using TRPM7-kinase," *Cellular signalling,* vol. 24, no. 11, pp. 2070-2075, 2012.

[46] M. Dorovkov, S. Beznosov, S. Shah, L. Kotlyanskaya, and A. Kostyukova, "Effect of mutations imitating the phosphorylation by TRPM7 kinase on the function of the N-terminal domain of tropomodulin," *Biophysics,* vol. 53, no. 6, pp. 500-504, 2008.

[47] A. Romagnani *et al.*, "TRPM7 kinase activity is essential for T cell colonization and alloreactivity in the gut," *Nature communications,* vol. 8, no. 1, pp. 1-14, 2017.

[48] S. Voringer *et al.*, "Inhibition of TRPM7 blocks MRTF/SRF-dependent transcriptional and tumorigenic activity," *Oncogene,* vol. 39, no. 11, pp. 2328-2344, 2020.

[49] M. Matsushita *et al.*, "Channel function is dissociated from the intrinsic kinase activity and autophosphorylation of TRPM7/ChaK1," *Journal of Biological Chemistry,* vol. 280, no. 21, pp. 20793-20803, 2005.

[50] K. Clark, J. Middelbeek, N. A. Morrice, C. G. Figdor, E. Lasonder, and F. N. van Leeuwen, "Massive autophosphorylation of the Ser/Thr-rich domain controls protein kinase activity of TRPM6 and TRPM7," *PloS one,* vol. 3, no. 3, p. e1876, 2008.

[51] M. V. Dorovkov, A. S. Kostyukova, and A. G. Ryazanov, "Phosphorylation of annexin A1 by TRPM7 kinase: a switch regulating the induction of an α-helix," *Biochemistry,* vol. 50, no. 12, pp. 2187-2193, 2011.

[52] K. Clark *et al.*, "The α-kinases TRPM6 and TRPM7, but not eEF-2 kinase, phosphorylate the assembly domain of myosin IIA, IIB and IIC," *FEBS letters,* vol. 582, no. 20, pp. 2993-2997, 2008.

[53] K. Clark *et al.*, "TRPM7 regulates myosin IIA filament stability and protein localization by heavy chain phosphorylation," *Journal of molecular biology,* vol. 378, no. 4, pp. 790-803, 2008.

[54] C. Song *et al.*, "Identification of TG100-115 as a new and potent TRPM7 kinase inhibitor, which suppresses breast cancer cell migration and invasion," *Biochimica et Biophysica Acta (BBA)-General Subjects,* vol. 1861, no. 4, pp. 947-957, 2017.

[55] M. I. Davis *et al.*, "Comprehensive analysis of kinase inhibitor selectivity," *Nature biotechnology,* vol. 29, no. 11, pp. 1046-1051, 2011.

[56] V. Chubanov *et al.*, "Epithelial magnesium transport by TRPM6 is essential for prenatal development and adult survival," *Elife,* vol. 5, p. e20914, 2016.

[57] L. V. Ryazanova *et al.*, "TRPM7 is essential for Mg^{2+} homeostasis in mammals," *Nature communications,* vol. 1, no. 1, pp. 1-9, 2010.

[58] C. Wei, X. Wang, M. Chen, K. Ouyang, L.-S. Song, and H. Cheng, "Calcium flickers steer cell migration," *Nature,* vol. 457, no. 7231, pp. 901-905, 2009.

[59] G. Krapivinsky, L. Krapivinsky, Y. Manasian, and D. E. Clapham, "The TRPM7 chanzyme is cleaved to release a chromatin-modifying kinase," *Cell,* vol. 157, no. 5, pp. 1061-1072, 2014.

[60] Y. Kim, H. G. Oh, Y. Y. Cho, O.-H. Kwon, M. K. Park, and S. Chung, "Stress hormone potentiates Zn^{2+}-induced neurotoxicity via TRPM7 channel in dopaminergic neuron," *Biochemical and biophysical research communications,* vol. 470, no. 2, pp. 362-367, 2016.

[61] L.-T. Su *et al.*, "TRPM7 regulates cell adhesion by controlling the calcium-dependent protease calpain," *Journal of Biological Chemistry,* vol. 281, no. 16, pp. 11260-11270, 2006.

[62] J. Sahni and A. M. Scharenberg, "TRPM7 ion channels are required for sustained phosphoinositide 3-kinase signaling in lymphocytes," *Cell metabolism,* vol. 8, no. 1, pp. 84-93, 2008.

[63] R. M. Touyz, "Transient receptor potential melastatin 6 and 7 channels, magnesium transport, and vascular biology: implications in hypertension," *American Journal of Physiology-Heart and Circulatory Physiology,* vol. 294, no. 3, pp. H1103-H1118, 2008.

[64] M. Aarts *et al.*, "A key role for TRPM7 channels in anoxic neuronal death," *Cell,* vol. 115, no. 7, pp. 863-877, 2003.

[65] M. C. Hermosura *et al.*, "A TRPM7 variant shows altered sensitivity to magnesium that may contribute to the pathogenesis of two Guamanian neurodegenerative disorders," *Proceedings of the National Academy of Sciences,* vol. 102, no. 32, pp. 11510-11515, 2005.

[66] V. Tseveleki *et al.*, "Comparative gene expression analysis in mouse models for multiple sclerosis, Alzheimer's disease and stroke for identifying commonly regulated and disease-specific gene changes," *Genomics,* vol. 96, no. 2, pp. 82-91, 2010.

[67] J. Du *et al.*, "TRPM7-mediated Ca^{2+} signals confer fibrogenesis in human atrial fibrillation," *Circulation research,* vol. 106, no. 5, pp. 992-1003, 2010.

[68] T. Hanano *et al.*, "Involvement of TRPM7 in cell growth as a spontaneously activated Ca^{2+} entry pathway in human retinoblastoma cells," *Journal of pharmacological sciences,* vol. 95, no. 4, pp. 403-419, 2004.

[69] J. Jiang, M.-H. Li, K. Inoue, X.-P. Chu, J. Seeds, and Z.-G. Xiong, "Transient Receptor Potential Melastatin 7–like Current in Human Head and Neck Carcinoma Cells: Role in Cell Proliferation," *Cancer Research,* vol. 67, no. 22, pp. 10929-10938, 2007.

[70] B. J. Kim, E. J. Park, J. H. Lee, J. H. Jeon, S. J. Kim, and I. So, "Suppression of transient receptor potential melastatin 7 channel induces cell death in gastric cancer," *Cancer science,* vol. 99, no. 12, pp. 2502-2509, 2008.

[71] A. Guilbert, M. Gautier, I. Dhennin-Duthille, N. Haren, H. Sevestre, and H. Ouadid-Ahidouch, "Evidence that TRPM7 is required for breast cancer cell proliferation," *American Journal of Physiology-Cell Physiology,* vol. 297, no. 3, pp. C493-C502, 2009.

[72] J. Jin, B. N. Desai, B. Navarro, A. Donovan, N. C. Andrews, and D. E. Clapham, "Deletion of Trpm7 disrupts embryonic development and thymopoiesis without altering Mg^{2+} homeostasis," *Science,* vol. 322, no. 5902, pp. 756-760, 2008.

[73] R. Sah *et al.*, "Timing of myocardial trpm7 deletion during cardiogenesis variably disrupts adult ventricular function, conduction, and repolarization," *Circulation,* vol. 128, no. 2, pp. 101-114, 2013.

[74] R. Sah *et al.*, "Ion channel-kinase TRPM7 is required for maintaining cardiac automaticity," *Proceedings of the National Academy of Sciences,* vol. 110, no. 32, pp. E3037-E3046, 2013.

[75] J. Jin *et al.*, "The channel kinase, TRPM7, is required for early embryonic development," *Proceedings of the National Academy of Sciences,* vol. 109, no. 5, pp. E225-E233, 2012.

[76] S. Stritt *et al.*, "Defects in TRPM7 channel function deregulate thrombopoiesis through altered cellular Mg^{2+} homeostasis and cytoskeletal architecture," *Nature communications,* vol. 7, no. 1, pp. 1-13, 2016.

[77] T. Kaitsuka *et al.*, "Inactivation of TRPM7 kinase activity does not impair its channel function in mice," *Scientific reports,* vol. 4, no. 1, pp. 1-7, 2014.

[78] L. V. Ryazanova, Z. Hu, S. Suzuki, V. Chubanov, A. Fleig, and A. G. Ryazanov, "Elucidating the role of the TRPM7 alpha-kinase: TRPM7 kinase inactivation leads to magnesium deprivation resistance phenotype in mice," *Scientific reports,* vol. 4, no. 1, pp. 1-11, 2014.

Acknowledgments

First, I would like to express my deep gratitude to **Prof. Dr. Thomas Gudermann**, who gave me the opportunity to complete my doctoral thesis at Walther-Straub-Institute.

Furthermore, I sincerely thank **Prof. Dr. Dr. Christian Grimm** for supervising this dissertation, his invaluable technical advice and his support in the experiments with breast cancer cells.

I am most grateful to **Dr. Vladimir Chubanov**, who made it possible for me to carry out my doctoral thesis in his laboratory. Your enthusiasm and enriching discussions have made me a better scientist. Thank you very much for that!

A special thanks goes to **Prof. Dr. Susanna Zierler**, who gave me a comprehensive introduction to electrophysiological techniques.

In addition, I would like to thank all my current and former colleagues: **Dr. Eva Schmücker, Joanna Zaißerer, Anna Rössig, Anna Erbacher, Dr. Banu Akdogan, Lisa Pleninger, Leonor Correia, Angel Tseung, Sebastian Weidenbach, Dr. Silvia Ferioli** and **Dr. Lorenz Mittermeier** - for the friendly atmosphere in the lab and your support.

I am deeply grateful to **Joanna Zaisserer** and **Anna Erbacher** for their technical help, experimental support and for keeping the lab running smoothly.

A special thanks to **Dr. Eva Schmücker, Anna Rössig, Dr. Jasmin Becker, Dr. Aaron Treder, and Christian Hermann** who always had a sympathetic ear and helpful advice for me. I am grateful to have you as friends!

A big thank you to everyone who critically proofread my thesis, especially **Dr. Timothy Ramnarine** and **Leeanne Mundle**.

Finally, my heartfelt thanks go to my parents **Irina Egawa** and **Dr. Masashi Egawa**, my siblings **Mayumi Egawa** and **Masamitsu Egawa**, my husband **Marcel Udina** and

my dogs **Filou, Monty** and **Finn** - for their love, their unwavering support and their encouragement in all situations. Thank you for always being there for me! I am eternally grateful for your love, your boundless support and for having you in my life.